Title
LOCAL SURFACE STRUCTURES OF c(2x2) S/Ni(011) AND (2x2) S/Ge(lll) DETERMINED USING ARPEFS

Author
Robey, S.W.

Publication Date
1986-04-01

LBL-21468 c.2

Lawrence Berkeley Laboratory
UNIVERSITY OF CALIFORNIA

Materials & Molecular Research Division

LOCAL SURFACE STRUCTURES OF c(2x2) S/Ni(011) AND (2x2) S/Ge(111) DETERMINED USING ARPEFS

S.W. Robey
(Ph.D. Thesis)

April 1986

Prepared for the U.S. Department of Energy under Contract DE-AC03-76SF00098

DISCLAIMER

LBL-21468

Local Surface Structures of c(2x2) S/Ni(011) and (2x2) S/Ge(111) Determined Using ARPEFS

Steven Wayne Robey

Ph.D. Thesis

Materials and Molecular Research Division
Lawrence Berkeley Laboratory
and
Department of Physics
University of California
Berkeley, California 94720

Local Surface Structures of c(2x2) S/Ni(011) and (2X2) S/Ge(111) Determined Using ARPEFS

Steven Wayne Robey

ABSTRACT

Angle-resolved photoemission extended fine structure (ARPEFS) measurements were performed on the c(2x2) S/Ni(011) and (2x2) S/Ge(111) systems. The S/Ni(011) system was studied to assess the extent to which surface structural information can be obtained from ARPEFS and to provide a large data set for comparison to recently developed multiple-scattering calculations. The results of that study indicate that ARPEFS is not only capable of producing reliable information concerning the major features of the adsorption site-- sulfur adsorbs in a rectangular hollow site 2.20 Å above a second layer Ni atom-- but can also detect relaxations induced by chemisorption. Thus, an expansion of the first Ni interplanar separation (11%) previously indicated by ion scattering experiments was confirmed, and a further reconstruction consisting of a buckled second Ni layer was suggested.

The S/Ge(111) study extended the ARPEFS investigations to a previously unstudied system and also provides the first application of ARPEFS to a semiconductor substrate. The choice of (2x2) S/Ge(111) was partially motivated by the results of a SEXFAS measurement performed on the similar (2x2) Te/Ge(111) system. That study indicated that Te adsorbs on Ge(111) in a 3-fold surface site directly above a second layer Ge atom. The results of the ARPEFS investigation indicate that sulfur adsorbs on Ge(111) in a 2-fold bridge site, 1.03 ±0.05 Å above

the first Ge layer. This is different from the site determined for Te/Ge(111), but agrees with the adsorption sites proposed for Te/Si(111) and Se/Si(111). The data also indicate a contraction (9%) in the first interplanar separation (the separation of the two components of the first bilayer), and an expansion of 7 ±3 % in the bond lengths between the Ge bilayers (2.60-2.65 A versus a bulk value of 2.45 A). This last result applies to the bonds which are most nearly below the 2-fold adsorption site.

David A Shirley

Local Surface Structures of c(2x2) S/Ni(011) and (2x2) S/Ge(111) Determined Using ARPEFS

Contents

CHAPTER 1

General Introduction

Angle-resolved photoemission (ARP) is well known as a probe surface electronic structure. An increasing number of studies have also used this technique to deduce surface atomic structure.[1-4] Surface structural information is contained in ARP due to final state interference caused by scattering of the photoelectron from neighboring atoms.

Two experimental variants have been employed to measure these interference effects. Azimuthal photoelectron diffraction[2] is based on measuring the oscillatory structure in the photocurrent as the electron emission angle is scanned, while keeping the photon energy constant. An alternate method, used in this work, is variable-energy photoelectron diffraction. This technique consists of performing a constant initial-state scan for a core level, with the electron emission direction held fixed. Originally this method was called normal photoelectron diffraction.[3,4] More recently, the name angle-resolved photoemission extended fine structure (ARPEFS)[1] has been employed to better acknowledge the analogy to EXAFS and the advantages of non-normal emission directions.

Early studies of variable energy photoelectron diffraction were successful in determining a number of surface structures.[3] Extraction of structural information in these studies was implicit, in being based on comparisons of the data to LEED-like multiple scattering calculations.[5] The attractiveness of ARPEFS was recently enhanced by a study which indicated that Fourier transforms could be employed to facilitate explicit data analysis, yielding more direct access to structural information.[1] That study, along with the presentation of a theoretical model based on a more EXAFS-like cluster approach[6] to describe the scattering, led to the name ARPEFS.

The work described in this thesis was designed to further evaluate the application of the ARPEFS technique for obtaining surface structural information, while at the same time performing these studies on systems which would in themselves provide interesting results.

In Chapter 4, we report ARPEFS experiments performed for photoemission from the S(1s) level in the system c(2x2) S/Ni(011). This research was motivated by several goals. First, the c(2x2) S/Ni(011) was chosen in part because it has been well studied in previous LEED[7,8]and ion-scattering[9] experiments. This system therefore provides a stringent test for ARPEFS to generate a unique, accurate, and correct surface structure. In this context, for example, the ion-scattering analysis indicated an expansion of the first Ni interplanar separation by 6%. Thus the ability of ARPEFS to confirm this result would provide strong support for the capacity of this technique toprovide reliable surface structures.

Second, the analysis of the ARPEFS $\chi(k)$ curve (defined below) can be performed at three levels of increasing sophistication. Two of these are analogous to standard EXAFS analyses. The first is based simply on Fourier transforming $\chi(k)$ to form a spectrum, F(r), with intensities at various "path length differences". These distances can then be compared with expectations based on trial geometries. The second, more quantitative, level consists of selecting a peak in F(r) that arises mostly from one path length difference, if one is available, and back-transforming to derive the value for that distance. At the third level, the ARPEFS curve is fitted with a theoretical curve for which structural parameters are thereby optimized. Our goal in analyzing the c(2x2) S/Ni(011) data is to ascertain the extent and validity with which structural information can be obtained from each level of analysis. Until now this question has been uncertain and even controversial, for lack of adequate data.

Finally, previous ARPEFS studies[1,10] have concentrated on data taken for high symmetry crystallographic directions. However, there is no reason to expect that the adsorption site will maintain the bulk symmetries, especially when considering more complicated systems. This study has attempted to select experimental geometries which help elucidate the surface structure. In this work, experimental geometries were chosen to test proposed structures by collecting ARPEFS data for angles which have increased sensitivity to selected atoms.[11] This study is the first investigation to be performed employing experimental geometries based on the local structure of the adsorption site rather than the crystallographic symmetries of the bulk substrate.

The second study, (2x2) S/Ge(111), applies the technique to a system for which no previous structural information exists. This system was chosen for a number of reasons. The directional bonding in covalent semiconductors, leading to the concept of "dangling bonds" at the surface, presents more interesting possibilities for investigations of chemisorption on these surfaces than is typically found for metallic substrates. Second, while the S/Ge(111) system has not been studied, similar systems have been investigated. Previous experiments employing surface-extended x-ray absorption fine structure measurements were performed for Te/Ge(111) and Te/Si(111).[12] The results of these investigations indicated an interesting deviation from the expected adsorption behavior-- based on a very simple model-- for the Te/Ge(111) case. Since the ARPEFS technique is best used in a mode in which possible surface structures are tested, this previous information allowed for the design of an experiment which could at the very least answer the question of whether or not sulfur adsorbs in the same site as that proposed for Te on this surface.

Another attractive feature of the S/Ge system is the absence of numerous strong Auger peaks in the energy range of importance in the measurement of ARPEFS (~ 50-400 eV)-- this makes the data reduction much less painful. Also, the region of photon energy necessary for studying photoemission from the S(1s) core level is relatively free of edge structure and "crystal glitches" on the double-crystal monochromator[13] employed in these experiments. Finally, Ge has a backscattering amplitude which is similar to that found for Cu or Ni, so that the results of previous ARPEFS experiments gave hope for reasonably large ARPEFS oscillations if backscattering geometries were used.

The remainder of this thesis is organized as follows. Chapter 2 provides a descriptive overview of the fundamental ideas necessary for understanding the origin of ARPEFS and the extraction of structural information from measurements of the fine structure. Chapter 3 provides an explanation of the experimental set-up and methods of data collection and reduction. The measurement and analysis of ARPEFS for the system c(2x2) S/Ni(011) is described in Chapter 4, while Chapter 5 describes similar measurements performed for the (2x2) S/Ge(111) system. Chapter 6 provides conclusions which can be drawn from these experiments.

REFERENCES

1. J.J. Barton, C.C. Bahr, Z. Hussain, S.W. Robey, J.G. Tobin, L.E. Klebanoff, and D.A. Shirley, Phys. Rev. Lett. 51, 272 (1983).
2. a) S. Kono, C.S. Fadley, N.F.T. Hall, and Z. Hussain, Phys. Rev. Lett. 41, 117 (1978); b) S. Kono, S.M. Goldberg, N.F.T. Hall, and C.S. Fadley, Phys. Rev. Lett. 41, 1831 (1978); c) P.J. Orders, R.E. Connelly, N.F.T.Hall, and C.S. Fadley, Phys. Rev. B 24, 6163 (1981).
3. a) S.D. Kevan, D.H. Rosenblatt, D.R. Denley, B.-C. Lu, and D.A. Shirley, Phys. Rev. B 20, 4133 (1979); b) S.D. Kevan, J.G. Tobin, D.H. Rosenblatt, R.F. Davis, and D.A. Shirley, Phys. Rev. B 23, 493 (1981); c) S.D. Kevan, R.F. Davis, D.H. Rosenblatt, J.G. Tobin, M.G. Mason, D.A. Shirley, C.H. Li, and S.Y. Tong, Phys. Rev. Lett. 46, 1629 (1981); d) D.H. Rosenblatt, S.D. Kevan, J.G. Tobin, R.F. Davis, M.G. Mason, D.R. Denley, D.A. Shirley, Y. Huang, and S.Y. Tong, Phys. Rev. B 26, 1812 (1982).
4. D.H. Rosenblatt, J.G. Tobin, M.G. Mason, R.F. Davis, S.D. Kevan, D.A. Shirley, C.H. Li, and S.Y. Tong, Phys. Rev. B 23, 3828, (1981).
5. S.Y. Tong, and C.H. Li, in Chemistry and Physics of Solid Surfaces, vol. III, ed. R. Vanselow and W. England, CRC Press, (1982), p.287; C.H. Tong and S.Y. Tong, Phys. Rev. Lett. 43, 526, (1979).

6. P.J. Orders and C.S. Fadley, Phys. Rev. B 27, 781 (1983); E.L. Bullock, C.S. Fadley, and P.J. Orders, Phys. Rev. B 28, 4867 (1983); M. Sagurton, E.L. Bullock, and C.S. Fadley, Phys. Rev. B 30, 7332 (1984).

7. J.E. Demuth, D.W. Jepsen, and P.M. Marcus, Phys. Rev. Lett. 32, 1182 (1974).

8. P.M. Marcus, J.E. Demuth, and D.W. Jepsen, Surf. Sci. 53, 501 (1973).

9. J.F. van der Veen, R.M. Tromp, R.G. Smeek, and F.W. Saris, Surf. Sci. 82, 468 (1979).

10. C.C. Bahr, J.J. Barton, Z. Hussain, S.W. Robey, J.G. Tobin, and D.A. Shirley, (to be published).

11. J.J. Barton, S.W. Robey, C.C. Bahr, and D.A. Shirley, 1st Intl. Conf. on the Structure of Surfaces, Berkeley, CA., Springer Series in Surface Sciences 2, ed. M.A. Van Hove and S.Y. Tong, (1985)

12. P.H. Citrin, P. Eisenberger, and J.E. Rowe, Phys. Rev. Lett. 48, 802 (1981).

13. Z. Hussain, E. Umbach, D.A. Shirley, and J. Feldhaus, Nucl. Instrum. Methods 195, 115 (1982).

CHAPTER 2

Theory

2.1 Introduction

Surface structural information is contained in angle-resolved photoemission measurements due to final state interference effects caused by scattering of the photoelectron from neighboring atoms. This information can be extracted by performing an ARPEFS (Angle-Resolved Photoemission Extended Fine Structure) measurement. This experiment consists of measuring the angle-resolved photoemission intensity from a core level of the adsorbed atom or molecule as a function of the photoelectron kinetic energy. The measured photoelectron current oscillates as the photoelectron kinetic energy is varied. This is caused by interference between that part of the emitted photoelectron wave which travels directly to the detector and that part which propagates first to a neighboring atom, where it is elastically scattered toward the detector. The path length difference for these two propagation paths leads to a phase difference between the two components at the detector. As the photoelectron kinetic energy is increased, this phase difference increases, resulting in a series of maxima and minima in the photoemission intensity.

Theoretical treatments of ARPEFS, or photoelectron diffraction, have been presented by several groups.[1-5] The degree of sophistication has varied from simple single scattering cluster models to fully dynamical treatments derived from LEED theory. Work by Barton et al.[5,6] provided approximations which allow one to include important multiple-scattering and spherical wave effects while retaining the physical insight offered by a cluster approach, thus providing a bridge between the two extremes. For completeness, this chapter will provide an overview of the important physics behind ARPEFS. More detailed and rigorous accounts can be found in the previously cited references. Section 2.2 will provide a qualitative discussion of ARPEFS starting with a simple model and present the major conclusions that have been derived from previous studies. Section 2.3 will then provide an explanation of the approximations considered in Refs. (6) and (7), and which were used to include spherical wave effects in calculating ARPEFS presented in later chapters.

2.2 ARPEFS theory

Because we are concerned primarily with presenting the major qualitative ideas that can be extracted from detailed theories of ARPEFS, we will begin by presenting an expression for $\chi(k)$ which is derived with some simplfying assumptions. These involve representing the photoelectron wave at the scattering center using the plane wave approximation[8] and including only single scattering. The derivation provided is more schematic than rigorous. After considering the implications of this simple model, we will discuss the modifications that must be considered when the dominant effects of multiple scattering are included.

2.2.1 Single scattering

We begin by considering the simple system illustrated in Fig. 1. A soft x-ray photon is incident on an adsorbed S atom, leading to the excitation of a photoelectron from an inner core level. The wave function for this outgoing photoexcited electron at position $\vec{r}$ is given by

$$\psi(\vec{r}) = A_{10}(k)\ Y^{*}_{10}(\hat{r}) h_1(kr) \tag{1}$$

with the assumption of photoexcitation from an s initial state. The photoexcitation (dipole) matrix element, $A_{10}(k)$, is assumed to be slowly varying as a function of the photoelectron kinetic energy (or wave number, k) for this initial state. The function $h_1(kr_2)$ is a spherical Hankel function of the first kind for $l = 1$, and $Y^*_{10}(\hat{r})$ is a spherical harmonic for $l,m = 1,0$.

The photoelectron wave incident on the Ni scattering atom at $\vec{R}_j$ is given by

$$\psi(\vec{R}_j) = A_{10}(k)\ Y^*_{10}(\hat{R}_j)e^{ikR_j}/kR_j, \tag{2}$$

where it is assumed that $kR_j >> 1$. The scattered wave at point $\vec{R}$ emanating from this point is then given by

$$\begin{aligned}\psi(\vec{R}) &= A_{10}(k)\ Y^*_{10}(\hat{R}_j)e^{ikR_j}/kR_j(k\ f(\theta_j))\ e^{ik\rho}/k\rho, \\ &= A_{10}(k)\ Y^*_{10}(\hat{R}_j)e^{ikR_j}/R_j(f(\theta_j))\ e^{ik|\vec{R}-\vec{R}_j|}/k|\vec{R}-\vec{R}_j|,\end{aligned} \tag{3}$$

where $\vec{R} = \vec{R}_j + \vec{\rho}$. The scattering of the photoelectron from the atom at R_j is represented by the complex scattering amplitude, $f(\theta_j)$, for scattering through an angle θ_j. This scattering amplitude is a function of the phase shifts for the particular potential at $\vec{R}_j$. For example, in the plane-wave approximation, for which the curvature of the incident photoelectron wave across the scattering potential is neglected, the scattering amplitude assumes the familiar form

$$f(\theta_j) = \sum_l (1/2ik)(e^{2i\delta_l} - 1)(2l+1)P_l(\cos\theta_j). \tag{4}$$

At the position, $\vec{R}$, of the detector the total wave function can be written

$$\psi(\vec{R}) = \psi_o(\vec{R}) + \psi_s(\vec{R}), \tag{5}$$

with $\psi_o(\vec{R})$ representing that part of the photoelectron wave which propagates directly to the detector, and $\psi_s(\vec{R})$ giving the scattered contribution. The photocurrent measured by the detector is given by

$$\begin{aligned} I &= \psi^*(\vec{R})\psi(\vec{R}) \\ &= \psi_o^*(\vec{R})\psi_o(\vec{R}) + \psi_o^*(\vec{R})\psi_s(\vec{R}) + \psi_s^*(\vec{R})\psi_o(\vec{R}) + \psi_s^*(\vec{R})\psi_s(\vec{R}) \end{aligned} \tag{6}$$

Neglecting the scattered-scattered components and forming

$$\chi = \psi^*\psi \;/\psi_o^*\psi_o \; - 1 \tag{7}$$

gives

$$\begin{aligned} \chi(k) &= 2 \operatorname{Re} (\psi_o^*\psi_s) \;/\psi_o^*\psi_o \\ &= \frac{\cos\beta_j}{\cos\gamma} \; \frac{|f(\Theta_j)|}{R_j} \; \cos(k(R_j - R_j\cos\Theta_j) + \phi_j) \end{aligned} \tag{8}$$

Summing over scattering from atoms which are near the adsorbed atom and including terms to account for inelastic losses leads to

$$\chi(k)=2\ \Sigma_j \frac{\cos\beta_j}{\cos\Upsilon}\ \frac{|f(\Theta_j)|}{R_j}\ \cos(k(R_j-R_j\cos\Theta_j)+\phi_j) \qquad (9)$$
$$\times\ e^{-\Delta R_j/\lambda}\ e^{-\sigma_j{}^2(1-\cos\Theta_j)k^2}.$$

As indicated, the summation is over all atoms near the adsorbed "source" atom from which the core level photoemission is being measured. The angle β_j is measured between the photon polarization vector and the vector connecting the emitting and scattering atoms, R_j is the bond length between the emitting and j-th scattering atoms, and Υ is the angle between the polarization and the electron emission direction. The j-th scattering atom is characterized by a complex scattering amplitude, $f(\Theta_j) = |f(\Theta_j)|\ e^{i\phi_j}$. Both the magnitude of $f(\Theta_j)$ and the phase, ϕ_j, depend on the scattering angle, Θ_j, and the photoelectron wave number, k. The emission angle dependent path length difference is given by $\Delta R_j=R_j-R_j\cos\Theta_j$. Inelastic damping due to thermal vibrations is included using a Debye-Waller term, where σ_j^2 is the mean-square relative displacement between the emitting and scattering atoms, projected on the photoelectron momentum change direction. Inelastic losses due to excitation of plasmons and electron-hole pairs by the energetic photoelectron are incorporated in an electron mean-free path, λ.

Each term in the summation represents the ARPEFS due to interference between the direct wave and the wave scattered from a neighboring ion core potential, as described previously. The cosinusoidal factor has a frequency given by the path length difference for that scattering event, with an additional small contribution to the phase from the complex scattering amplitude. These oscillatory functions are multiplied by angle and energy (or wave number) dependent amplitudes. The amplitudes for given scattering atoms are determined by a number of factors:[2,5]

(1) The finite electron mean free path, the lower correlation of thermal vibration at larger distance, and the $1/r_j$ dependence of the oscillation amplitude all act to limit strongly the number of atoms which contribute significantly to the ARPEFS. Thus the ARPEFS is dominated by the local atomic structure.

(2) The scattering amplitude $|f(\theta_j)|$ is peaked in the forward and backscattering directions, with only weak scattering for angles in between. Thus, atoms which provide near backscattering will usually produce large intensity modulations in $\chi(k)$. Structure at low ΔR_j values due to near-forward scattering will become important for near-grazing emission or for sub-surface adsorption.

(3) The factor $\cos \beta_j$ arises from the orientation of the photon polarization with respect to the vector from the emitting atom to the scattering atom. This factor determines the amplitude of the photoelectron p-wave that

> is incident on the scattering center. Orientation of the polarization such that the bond vector for a particular scattering atom lies in the nodal plane of the p-wave final state will lead to negligible intensity for that scattering path length.

Two major conclusions can be drawn from this discussion. First, scattering involving near-neighbors and near-backscattering will produce strong ARPEFS modulations. Secondly, specific atoms can be enhanced relative to others by proper choice of the photon polarization direction.

As indicated earlier, however, these conclusions were derived based on a model which incorporated some simplifying assumptions. Comparisons by Tong et al.[1] of fully dynamical calculations to kinematic theory indicated that the simple single scattering model used to derive these conclusions is inadequate for a quantitative description of ARPEFS. The recent studies of Barton et al.[5,7] also indicate that multiple scattering is important in many cases. We will now discuss what modifications are needed when multiple scattering is considered.

2.2.2 Multiple scattering

Because of the strong peaking of the scattering amplitude in the forward direction, the dominant multiple-scattering events will be those which include forward scattering. The quasidynamical theory[10] of Tong et al., which included all single scattering events and all orders of forward multiple scattering, gave curves essentially identical to those produced with their fully dynamical theory for photoelectron energies above 100 eV.[1] Since additional near-forward scattering events will introduce practically no extra path length difference, the inclusion of multiple scattering will serve primarily to enhance the amplitude of a single scattering event when that event is proceeded or followed by forward scattering. The additional forward scattering events act to focus the electron amplitude along the forward direction. Since backscattering will always be followed by a subsequent forward scattering through the emitting atom, we can see that multiple scattering will serve to enhance backscattering events even more strongly than is predicted for a single scattering theory.

In addition to this modification of the single scattering amplitude, there will also be additional contributions to the scattering phase shift for each additional forward scattering event. A correct determination of the amplitude enhancement and forward scattering phase shift requires the consideration of another of the approximations described above. The study by Barton et al.[6] of the effects of including the curvature of the photoelectron wavefront across the scattering potential versus treatment by the plane wave approximation indicated that correct treatment of spherical wave effects is necessary for near-forward scattering. Thus, considering the above discussion, the correct inclusion of the dominant multiple scattering effects requires a treatment which goes beyond the plane wave approximation. Attempts to treat multiple scattering within the plane wave approximation give results which are nearly as inaccurate as those introduced by completely neglecting the multiple scattering. Again, this is because the dominant multiple scattering effects involve forward scattering, and it is these events which are most poorly described by an approximation based on neglecting the wavefront curvature.

An exact treatment of spherical wave effects with multiple scattering rapidly becomes computationally unreasonable for higher kinetic energies. Barton et al.[6] have developed formulas for calculating spherical wave effects with successively higher levels of approximation. This allows the inclusion of a correct treatment of multiple scattering while maintaining the physical insights afforded by a cluster approach to the scattering. The next section will provide a brief discussion of the form of these approximations and the motivation behind them. Other investigations of spherical wave effects and approximations to include these effects can also be found in the literature.[11-13]

2.3 Spherical wave approximations

This section will provide a brief explanation of the approximations employed in calculating theoretical ARPEFS curves for comparison to data in this thesis. This discussion is based on the conclusions indicated by the detailed account which can be found in Ref. (7).

Starting with the Lippman-Schwinger equation for scattering from the crystal potential, and with the crystal assumed to consist of non-overlapping muffin-tins at $\vec{R}_j$ represented by individual scattering t-matrices, t_j, the required wave function at position $\vec{R}$ is given by

$$\psi(\vec{R}) = G_0\Phi_I + \sum_j G_0 t_j G_0 \Phi_I + \ldots \qquad (10)$$

Here Φ_I is the wavefunction for the excited photoelectron for the case of no scattering and G_0 is the free-electron propagator. Additional terms would include higher order scattering. Since the approximations that we will be discussing concern the form of the scattering amplitude, $f(\theta_j)$, we can concentrate this discussion on the second, single-scattering term in Eq. 10. Furthermore, we will concentrate primarily on the functional form of this term for various approximations.

With the coordinates as defined in Fig. 2, the single scattering term becomes

$$G_0 t_j G_0 \Phi_I \propto \int d\vec{r}_1^3 d\vec{r}_2^3 \; G_0(\vec{R}-\vec{r}_1) t_j(\vec{r}_1-\vec{R}_j;\vec{r}_2-\vec{R}_j) k h_1(kr_2) Y_{10}^*(\hat{r}_2) A_{10}(k) \tag{11}$$

where

$$G_0 \Phi_I = k h_1(kr_2) Y_{10}^*(\hat{r}_2) A_{10}(k) \tag{12}$$

with the assumption of an s initial state and $A_{10}(k)$ as defined in Section 2.2. The integrations over $\vec{r}_1$ and $\vec{r}_2$ are restricted to the muffin-tin of the scattering atom.

To proceed from this point, several aproximations can be employed. The plane-wave approximation,[8] which has proved useful for descriptions of EXAFS, consists of assuming

$$\begin{aligned} h_1(kr_2) Y_{10}^*(\hat{r}_2) &\approx h_1(kR_j) Y_{10}^*(\hat{R}_j)\; e^{i\vec{k}\cdot(\vec{r}_2-\vec{R}_j)} \\ &\approx h_1(kR_j) Y_{10}^*(\hat{R}_j)\; e^{i\vec{k}\cdot\vec{\rho}_2} \end{aligned} \tag{13}$$

The outgoing spherical wave is represented as a plane wave with the amplitude and phase of the spherical wave at $\vec{R}_j$.

If we employ the expansion

$$e^{i\vec{k}\cdot\vec{\rho}} = \sum_L 4\pi i^l \; j_l(k\rho_2) Y_L^*(\hat{\rho}_2) Y_L(\hat{k}), \tag{14}$$

where $L = (l,m)$ and also use

$$G_0(\vec{R}-\vec{R}_j-\vec{\rho}_1) = \tag{15}$$
$$-2ik \sum_{L_1} j_{l_1}(k\rho_1) Y_{L_1}^{*}(\hat{\rho}_1) h_{l_1}(k|\vec{R}-\vec{R}_j|) Y_{L_1}(\vec{R}-\vec{R}_j/|\vec{R}-\vec{R}_j|)$$

and define[14]

$$t_j(\vec{\rho}_1,\vec{\rho}_2) \equiv \sum_{L_2} t_{jl_2}(\rho_1,\rho_2) Y_{L_2}(\hat{\rho}_1) Y_{L_2}(\hat{\rho}_2) \tag{16}$$

then following, for instance, the treatment of Ref. (15) leads to

$$G_0 t_j G_0 \Phi_I \propto \tag{17}$$
$$\sum_L h_l(k|\vec{R}-\vec{R}_j|) Y_L(\vec{R}-\vec{R}_j/|\vec{R}-\vec{R}_j|) Y_L(\hat{R}_j)\; k^2(1/2ik)(e^{2i\delta_l} - 1)$$
$$\times\; h_1(kR_j) Y_{10}(\hat{R}_j) A_{10}(k).$$

Now, using the fact that $k|\vec{R}-\vec{R}_j| >> 1$ and the addition theorem for spherical harmonics, gives

$$G_0 t_j G_0 \Phi_I \propto \tag{18}$$
$$(e^{ik|\vec{R}-\vec{R}_j|}/k|\vec{R}-\vec{R}_j|)\; \{\sum_l k^2(1/2ik)(e^{2i\delta_l} - 1)(2l+1)P_l(\cos\theta_j)\}$$
$$\times\; h_1(kR_j) Y_{10}(\hat{R}_j) A_{10}(k).$$

If we let $h_1(kR_j) \approx e^{ikR_j}/kR_j$, then this is exactly Eq. 3 of Section 2.2 with

$$f(\theta_j) = \sum_l (1/2ik)(e^{2i\delta_l} - 1)(2l+1)P_l(\cos\theta_j), \tag{19}$$

the scattering amplitude for an incident plane wave.

A different approximation which more accurately accounts for spherical wave effects was used in Auger angular dependence studies by McDonnel et al.[16] and also studied for ARPEFS by Barton.[7] It consists of making the substitution

$$h_1(kr_2)Y^*_{10}(\hat{r}_2) \approx e^{ikr_2}/kr_2 \; Y^*_{10}(\hat{R}_j) \tag{20}$$

instead of the plane wave approximation of Eq. 13. Then using

$$e^{ikr_2}/kr_2 = \sum_L 4\Pi ik \; j_l(k\rho_2)h_l(kR_j)Y^*_L(\hat{\rho}_2)Y_L(\hat{R}_j), \tag{21}$$

where as before $\vec{r}_2 = \vec{R}_j + \vec{\rho}_2$, we obtain

$$G_0 t_j G_0 \Phi_I \propto \tag{22}$$
$$\left(e^{ik|\vec{R}-\vec{R}_j|}/k|\vec{R}-\vec{R}_j|\right) \left\{\sum_l k^2(1/2ik)(e^{2i\delta_l} - 1)(2l+1)P_l(\cos\theta_j)h_l(kR_j)\right\}$$
$$\times \; Y_{10}(\hat{R}_j)A_{10}(k).$$

With $h_l(kR_j) = e^{ikR_j}/kR_j \; (d_l(kR_j))$, this gives again the form of Eq. 3, but with a different scattering amplitude[7]

$$f(\theta_j) = \sum_l (1/2ik)(e^{2i\delta_l} - 1)(2l+1)P_l(\cos\theta_j)(d_l(kR_j)). \tag{23}$$

The reason for considering these approximations in the first place can be seen by examining the expression that results from an treatment employing the exact expansion for the outgoing spherical wave

$$\begin{aligned} & h_1(kr_2)Y^*_{10}(\hat{r}_2) = \\ & 4\pi \sum_{L,L_1} i^l\, c(L,L_1;1,0)\, h_{l_1}(kR_j)Y_{L_1}(\hat{R}_j)j_l(k\rho_2)Y^*_L(\hat{\rho}_2) \end{aligned} \tag{24}$$

where

$$c(L,L_1;1,0) = \int Y^*_L(\hat{k})Y_{L_1}(\hat{k})Y^*_{10}(\hat{k})\, d\Omega_k. \tag{25}$$

This leads to an expression for the scattered wave given by

$$\begin{aligned} & G_0 t_j G_0 \Phi_I \propto \\ & \left(e^{ik|\vec{R}-\vec{R}_j|}/k|\vec{R}-\vec{R}_j|\right) \Big\{ \sum_{L_1} Y_{L_1}(\vec{R}-\vec{R}_j/|\vec{R}-\vec{R}_j|) \sum_{L} c(L,L_1;1,0) \\ & x\; k^2(1/2ik)(e^{2i\delta_l} - 1)h_l(kR_j)Y_{10}(\hat{R}_j)\Big\}\, A_{10}(k). \end{aligned} \tag{26}$$

The increased complexity of this formula, due to the double summation over L and L_1, is easily apparent. In practice the sums on L,L_1 are truncated at values L_{max} for which $\delta_l(l > l_{max}) \sim 0$. For LEED theory, which typically includes energies up to ~ 250 eV, 8-10 phase shifts are sufficient. This allows the sum to be truncated for $l > 8$-10. However, the ARPEFS experiments presented here often involve photoelectron energies up to ~ 450-500 eV, thus requiring 15-20 phase shifts for convergence. Also, the inclusion of multiple scattering leads to further computational complexity in Eq. 26. When higher than single scattering is considered, the integrals $c(L,L_1,L_2)$ depend on all three indices since the incoming spherical wave is no longer restricted to $L_2 = (1,0)$. Thus, the combination of high kinetic energies and multiple scattering rapidly makes calculations employing Eq. 26 computationally time consumming and costly. On the other hand, the use of the simple plane-wave approximation popularized for EXAFS is also unacceptable due to the presence of strong forward scattering, multiple-scattering effects in ARPEFS in many cases.[7,17]

A means of overcoming this difficulty was presented in Refs. (6) and (7). Those studies showed that the homogenous wave model of Eqs. 20-23 provided a very good approximation to the exact form in most cases. This model produced much better results than the plane wave approximation for near forward scattering where spherical wave effects become important. Further, by examing Eq. 26, we can see that if we assume $Y^*_{10}(\hat{k})$ in the Gaunt integral can be approximated by

$$Y^*_{10}(\hat{k}) \approx Y^*_{10}(\hat{R}_j), \tag{27}$$

then the exact form is reduced to the homogenous wave model. Thus, by introducing a Taylor series expansion for $Y^*_{10}(\hat{k})$ about $\hat{R}_j$[18] in the Gaunt integral, Barton produced a series which reduces to the homogenous wave form (Eq. 22) and which can be used to systematically include higher levels of approximation. For convienence, a rotation to a coordinate system with the z-axis along $\hat{R}_j$[7] is performed so that the

Taylor series expansion is always performed about $\Theta = 0$. All of the calculations performed in this thesis for comparison to experimental ARPEFS used a level of approximation which included the first two additional orders above the zero-th, or homogenous wave, approximation. Futher discussions of the character of this approximation as well as other details of the calculations, such as the treatment of thermal effects and experimental resolution, can be found in Refs. (5) and (6).

REFERENCES

1. S.Y. Tong, and C.H. Li, in Chemistry and Physics of Solid Surfaces, vol. III, ed. R. Vanselow and W. England, CRC Press, (1982), p.287; C.H. Tong and S.Y. Tong, Phys. Rev. Lett. 43, 526, (1979).

2. P.J. Orders and C.S. Fadley, Phys. Rev. B 27, 781 (1983); E.L. Bullock, C.S. Fadley, and P.J. Orders, Phys. Rev. B 28, 4867 (1983); M. Sagurton, E.L. Bullock, and C.S. Fadley, Phys. Rev. B 30, 7332 (1984).

9. J.J. Barton, S.W. Robey, C.C. Bahr, and D.A. Shirley, 1st Intl. Conf. on the Structure of Surfaces, Berkeley, CA., Springer Series in Surface Sciences 2, ed. M.A. Van Hove and S.Y. Tong, (1985)

3. a) A. Liebsch, Phys. Rev. Lett. 32, 1203, (1974); b) T. Fujikawa, J. Elec. Spectro. Rel. Phen. 26, 79 (1982).

4. P.A Lee, Phys. Rev. B 12, 5261 (1976).

5. J.J. Barton, S.W. Robey, and D.A. Shirley, (to be published).

6. J.J. Barton and D.A. Shirley, Phys. Rev. A 32, 1019 (1985); J.J. Barton and D.A. Shirley, Phys. Rev. B 32, 1892,1906 (1985).

8. a) P.A. Lee and J.B. Pendry, Phys. Rev. B 11, 2795 (1975); b) C.A. Ashley and S. Doniach, Phys. Rev. B 11, 1279 (1975); c) P.A. Lee and G. Beni, Phys. Rev. B 15, 2862 (1977); d) B.K. Teo, in "EXAFS Spectroscopy: Techniques and Applications", Plenum Press, 1981, ed. B.K. Teo and D.C. Joy, p. 22.

7. J.J. Barton, Ph.D. thesis, Univ. of Calif., Berkeley (1985).

10. S.Y. Tong, M.A. Van Hove, and B.J. Mrstik, in Proceeding of the Seventh International Vacuum Conf. and the Third International Conf. on Solid Surfaces, Vienna, 1977, ed. R. Dobrozemsky et al, vol. 3, p. 2407.

11. J.E. Muller and W.L. Schaich, Phys. Rev. B 27, 6489 (1983).

12. H.C. Poon, D. Snider, and S.Y. Tong, Phys. Rev. B 33, 2198 (1985).

13. M. Sagurton, E.L. Bullock, R. Saiki, A. Kaduwela, C.R. Brundle, and C.S. Fadley, Phys. Rev. B 33, 2207 (1985).

14. J.L. Beeby, J. Phys. C 1,82 (1968).

15. C.H. Li, A.R. Lubinsky, and S.Y. Tong, Phys. Rev. B 17, 3128 (1978).

16. L. McDonnel, D.P. Woodruff, and B.W. Holland, Surf. Sci. 51, 249 (1975).

17. S.W. Robey, J.J. Barton, C.C. Bahr, G. Liu, and D.A. Shirley, (to be published).

18. W. Magnus and F. Oberhettinger, Formulas and Theorems for the Functions of Mathematical Physics, (Chelsea Pub. Co., New York, 1949) p. 54.

FIGURES

Fig. 1 This figure illustrates the important aspects of the scattering leading to ARPEFS. The incident soft x-ray photon excites a photoelectron which then scatters from neighboring atoms. The ARPEFS is caused by interference between the direct wave and the scattered wave at the detector. The angle α_j is the scattering angle of the photoelectron and the vector $\vec{R}_j$ gives the position of the scattering atom. The scattering is represented by the complex scattering amplitude, $f(\theta_j) = |f(\theta_j)|\, e^{i\phi_j}$. The angles β_j and γ (not shown) are the angles between the photon polarization and $\vec{R}_j$ and between the polarization and the vector to the detector, respectively.

Fig. 2 This figure defines the coordinates referred to in the text. The radius R_{mt} represents the muffin-tin radius of the "source" atom, and also the scattering atom at position $\vec{R}_j$. The vector $\vec{R}$ gives the position of the angle and energy resolving analyzer.

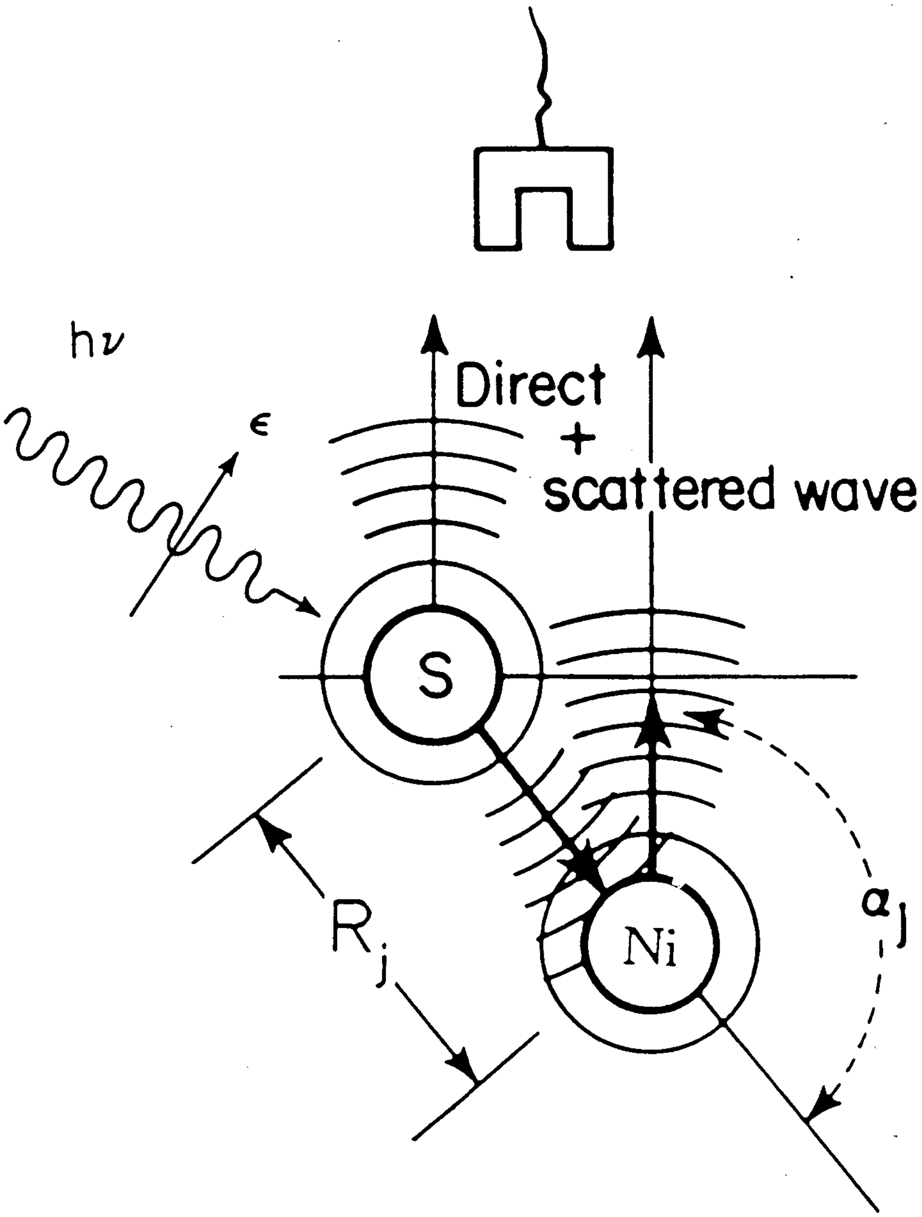

XBL 864-1271

Fig. 1

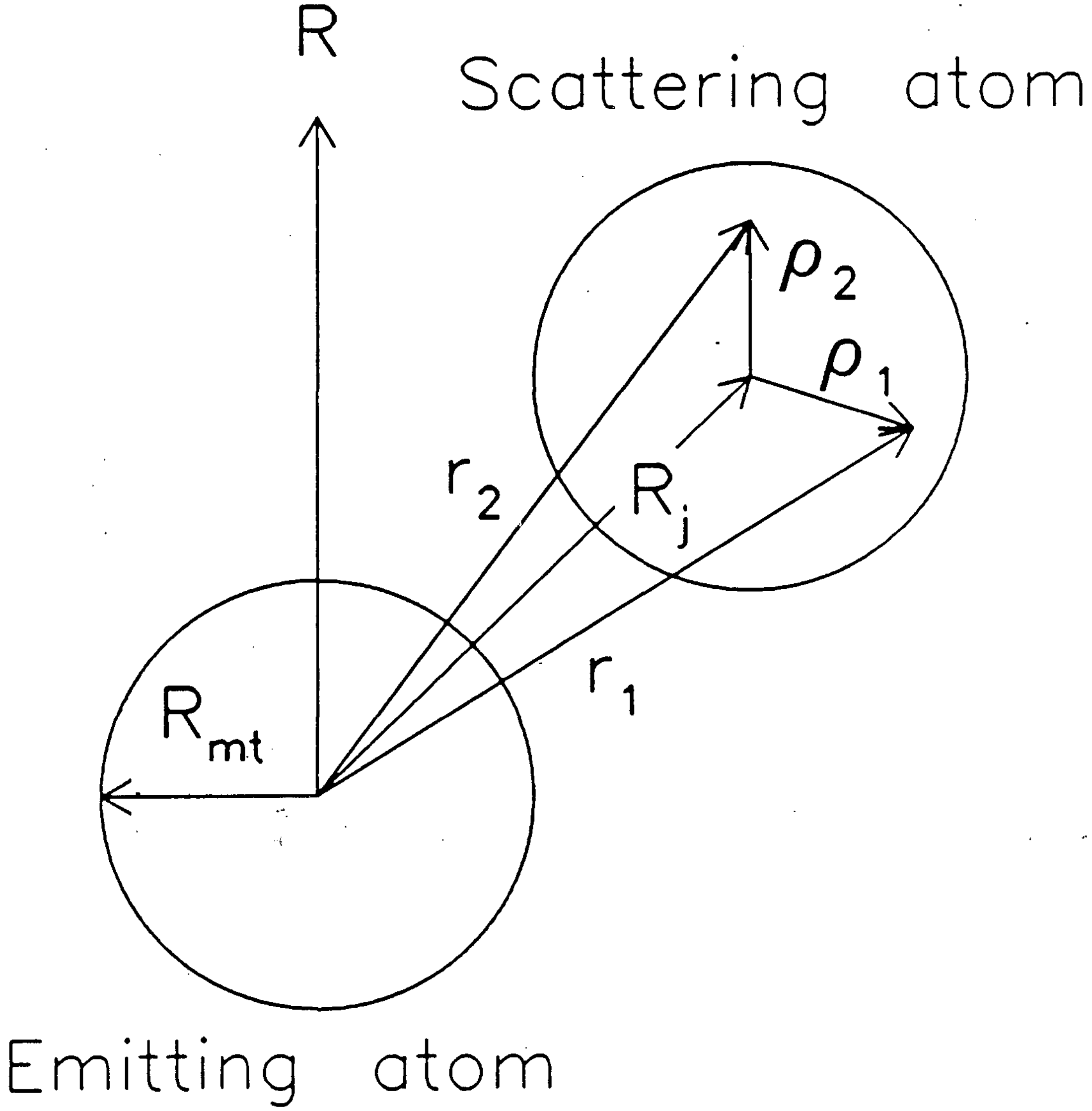

XBL 864-1272

Fig. 2

CHAPTER 3

Experimental Details

3.1 Introduction

The purpose of this chapter is to present a description of the experimental details of the measurements of ARPEFS to be described in later chapters. A schematic illustration indicating the major components of an ARPEFS experiment-- synchrotron source, monochromator, and UHV chamber and electron analyzer-- is given in Fig. 1. This discussion will center on those aspects which are common to all of the measurements-- details which are specific to a given system will be discussed in the chapters pertaining to those systems.

3.2 Experimental equipment

This section will provide a description of the facilities at the SPEAR storage ring and the UHV experimental chamber employed for these measurements. A detailed description of the beamline and monochromator can be found in Ref. (1), while more information on the chamber and analyzer is contained in Ref. (2).

3.2.1 Synchrotron facilities

These experiments were performed using synchrotron radiation from Beamline III-3 located at the Stanford Synchrotron Radiation Laboratory. On this beamline, synchrotron radiation from the SPEAR storage ring is incident on an approximately toroidal Pt coated mirror which deflects the beam by 2°. This reflection introduces a high photon energy cut-off at ~ 4.5 keV. The toroidal shape provides both horizontal and vertical focussing at a distance of 28 meters from the SPEAR source. The focussed beam measures 5 mm in the horizontal direction and 1 mm in the vertical direction. The soft x-ray UHV double-crystal monochromator on this beamline is described in detail elsewhere.[1] A selection of several crystal pairs can be interchanged without disturbing the UHV conditions. The allowed Bragg angle range of from 20°-80° enables the monochromator to cover a total spectral range of 800-4000 eV. The Bragg angle rotations are coupled to a change in the distance separating the two crystals so that the outgoing monochromatized photon beam maintains a fixed vertical height. For most of the work presented in this thesis, Ge(111) crystals were used to produce monochromatic x-rays in the spectral range from 2500 to 3800 eV. The resolving power of the instrument is 1.1×10^3. The monochromator is also equipped with a variety of filters prior to the first crystal to reduce the power load on that crystal, and thus reduce adverse effects due to crystal heating. Heating of the crystal causes changes in the crystal d-spacing. This in turn causes a change in the

Bragg angle, leading to energy shifts, and more importantly for this work, beam position shifts. A series of adjustable slits follow the monochromator and can be used to collimate the photon beam. The photon flux after the collimating slits is measured by collecting the total electron yield from a high transmission grid placed in the beam immediately prior to the entrance to the experimental chamber. The electron yield is measured by a channel electron multiplier connected through a battery box to a picoammeter. The synchrotron radiation entering the experimental chamber is ≥ 98% linearly polarized.

The monochromator is equipped with a maximum search feed-back loop to locate the proper Bragg condition for a given photon energy during a photon energy scan. The crystals are first moved to the approximate Bragg angle position and then one crystal is automatically rocked through a small angle. The signal measured by a channel electron multiplier and grid assembly is differentiated and a stop pulse is provided when the maximum is located.

3.2.2 UHV chamber and analyzer

The UHV experimental chamber was described in detail in previous work.[2] It consists of two levels of instrumentation. The upper level is used for sample preparation and characterization. It contains a four-grid LEED system employed for both LEED and Auger measurements, along with an ion gun for sample cleaning and a gas inlet system for preparing adsorbed overlayers. The lower level contains the hemispherical electrostatic analyzer employed for collecting angle-resolved photoelectron spectra. This analyzer is mounted on a carriage which allows rotations under UHV conditions of 360° about a vertical axis and 100° about a horizontal axis.

The input lens to the analyzer consists of two three-element Einzel lenses, with a decelerating stage in between. The decelerating stage allows the analyzer to be operated with a constant pass energy and, thus, with a constant resolution given by[2] 0.006 x PE. For ARPEFS measurements, the quantity of primary interest is the intensity in the core peak, so that resolution can be traded for increased counting rates. For this reason, the analyzer was normally operated with a pass energy of 160 eV, giving an analyzer contribution to the resolution of ~ 1 eV. The deceleration also determines the sensitivity of the instrument as a function of the measurement energy, giving a transmission that is theoretically proportional to 1/E for energies above ~ 100 eV. The angular acceptance varies from ± 3° at low energy (50-100 eV) to ± 1° for higher energies (>300 eV). An additional important feature of the analyzer is the use of a microchannel plate detector coupled to a resistive position sensitive anode to provide multichannel data accumulation. This provides an increase of >10 in the collection efficiency over single channel collection.

3.3 Data collection and reduction

The ARPEFS experiment consists of measuring the angle-resolved photoemission intensity from a specific core level-- usually a core level of an adsorbed atom on a clean, single crystal surface-- as a function of the photoelectron kinetic energy. Thus, for each experimental geometry, a series of photoelectron spectra with increasing kinetic energies are collected using a 15-20 eV energy window which includes the core level of interest. The window width should be chosen to include adequate segments of background on either side of the photoelectron peak to allow proper fitting (to be described below) to determine the peak intensity. The energy range of the experiment normally extends from 50 -400 eV above the core level threshold. This range is covered with 70 -100 spectra which, on the average, take 10 -15 minutes collection time apiece to acquire adequate statistics. This then requires a total data collection time of 10 -24 hours, depending on the system studied and the synchrotron beam conditions. This includes only actual data collection time and does not include time spent for new fills of the SPEAR storage ring which occur during the experiment. For use in later fitting and normalization, a background spectrum is accumulated for the total 400-500 eV kinetic energy range that is to be measured, consisting of a spectrum taken with the photopeak at lower kinetic energies. This provides a measurement of the secondary background not associated with the photopeak in the experimental energy range. Fig. 2 shows a typical measured inelastic background with a representative core level (S(1s)) spectrum in the inset. The solid lines represent the result of a fit to the core peak as described below.

The reduction of these data then requires extracting the intensity in the core peak and normalizing for the photon flux. The peak intensity is extracted by fitting to a model which employs a gaussian to describe the photoelectron peak, a gaussian step function to model the inelastic electrons associated with this peak, and either the empirically measured background or a polynomial function to model the remaining background due to other secondary processes. The final results are not greatly affected by the particular model (peak shape, background function, etc.) used in the fits. This is because the ARPEFS information is contained in the relative change in the measured intensity so that all that is required is a model which provides a consistent measure of this intensity. For instance, since the peak width is approximately constant, a preliminary analysis of the ARPEFS can be accomplished by simply using the peak height above the background. This is useful for inspecting the data during the accumulation of the scan. The use of different reasonable models for fitting will typically produce results that vary on the 2 -3 % level.

The necessity of accurately determining the peak area leads to restrictions on the materials which can be conveniently studied by ARPEFS. Elements with several strong Auger transitions producing Auger peaks in the energy range from 100 - 400 eV often make data reduction extremely difficult, if not impossible. This is the analog of the problems encountered in SEXAFS measurements based on monitoring Auger emission when a photopeak passes through the Auger window. This problem may be avoided by performing ARPEFS measurements using core levels with binding energies less than those which give rise to the Auger transitions.

The intensities obtained by fitting must be normalized for the incident photon flux. This normalization is important primarily for removing sharp changes such as those due to monochromator crystal "glitches" or new fills of the SPEAR storage ring. Two different methods have been employed in this work. The first method consists of using the flux measured by the channel electron multiplier and grid assembly mentioned above. A suitable choice of grid material must be made to ensure that there is no structure in the grid absorption in the experimental range (i.e. no absorption edges). This measurement must then be corrected for the absorption of the grid in this range. The advantage of this method is its simplicity. However, because the grid is typically much larger than the sample, this measurement is not sensitive to small beam movements which lead to changes in the actual flux at the focal point of the input lens of the analyzer. Thus, new fills of the storage ring can result in discontinuous jumps in the ARPEFS curve due to beam movement. Several data points (5 -6) should be repeated after each fill so that the results from the two fills can be scaled appropriately. Also, the present data acquisition programs sample this flux measurement at only three points during the accumulation of a particular spectrum. Because of the rather long collection times, the photon flux can vary significantly during this period, especially under noisy beam conditions. This could be improved by accumulating a running average of the flux monitor throughout the collection of each spectrum.

Another method of normalization necessitates the use of the empirically measured background spectrum in the fitting process. This spectrum must be accumulated during a period of time when the photon flux is not rapidly changing, so that it is performed with approximately constant flux. Subsequently, when the fits are performed to extract the photopeak intensity, the scale factors between this background spectrum and the individual spectra in the ARPEFS scan determined from the fit provide the scale factors between the flux for each data point normalized to the flux for which the background spectrum was taken. At its best, this method typically provides a smoother result than the measurement employing the high transmission grid and also produces better fill-to-fill normalization. However, it too can be sensitive to beam movement which causes a change in the background function from the measured one. Also, since the background spectrum is typically measured in segments with a single or several widely spaced photon energies, rapid changes in the secondary background with photon energy due, for instance, to core thresholds in the substrate also produce problems. The sample mounting can also affect the results obtained using this normalization method. For the experiments presented here, the samples were mounted on Ta sample plates because of the high temperature stability of Ta and the ease of spot-welding to this material. However, on several occaisons structure in the kinetic energy range of 150 -220 eV has been observed in the background, which was sensitive to changes in sample and beam positions. These effects were severe enough in some cases to render the empirically measured background function useless for fitting. Thus, because of the large beam spot size in the horizontal direction, it is important to use as large a sample as possible, and to mount the sample in a manner that completely ensures that only electrons emitted from the sample material enter the analyzer. This should be coupled with careful collimation of the photon beam prior to beginning the experiment.

In essence the two methods of normalization are similar in nature-- the measurement of the empirical background function amounts to replacing the total yield measurement from the grid with a very restricted partial yield measurement from the sample to determine the flux. Neither method adequately accounts for beam movement so that this problem must be solved by maintaining the beam in the same position throughout the scan by constantly re-optimizing the sample count rate, assuming that the sample was properly aligned at the start of the scan. Also, it is important in this respect to allow the first monochromator crystal to reach an equilibrium temperature after a new fill since there are large beam movements during this preliminary heating period.

There have been several proposals for schemes to reduce the problem of beam movement and energy shifts on this beamline, which must be accomplished by reducing the problems of changes in temperature of the first crystal. These include either heating the crystal to maintain it at constant temperature or empirically determining the magnitude of the effect as a function of, for example, the beam current in the ring and then providing proper corrections on this basis. However, these proposals have existed for several years with no results, so that it must be assumed that there will be no significant change in the situation in the forseeable future. A possible alternative to the manual re-optimization for each spectrum that is necessary to correct for this problem would involve using an additional maximum search loop after the one employed to determine the proper Bragg angle condition. This maximum search would maximize the crystal translation based on the total counts observed by the analyzer. Possible problems with this scheme would involve the lack of a well defined maximum for the proper beam position and the low signal level.

Once the photopeak has been properly normalized, the resulting intensity as a function of the photoelectron kinetic energy is, in analogy with EXAFS[3], composed of a slowly varying, atomic-like portion and a rapidly oscillating contribution due to the interference effects of electron scattering from neighboring ion cores. The total measured intensity can be written

$$I(E) = (\chi(E)+1)\ I_0(E). \qquad (1)$$

Here $I(E)$ represents the total intensity as a function of the photoelectron kinetic energy, E, $\chi(E)$ is the oscillatory interference function, and $I_0(E)$ is a slowly varying function.

$I_0(E)$ can contain contributions from several sources. In an idealized experiment, $I_0(E)$ arises from the energy dependence of the photoexcitation matrix element. However, $I_0(E)$ can also contain slowly varying structure introduced by data collection or reduction procedures described above, as well as components of ARPEFS with small scattering path lengths. Slowly varying structure can be introduced by the beam movement alluded to earlier or by systematic changes in the fits due to the change in slope of the inelastic electron background or other structure in the background. Because the exact form of $I_0(E)$ is unknown, the low frequency structure is extracted by fitting the data with a quadratic or cubic polynomial or a smooth cubic spline. The unavoidable shortcoming of this procedure is that real ARPEFS structure with scattering path lengths less than 1.5-2 Å can be unintentionally distorted or completely removed. This point will be further discussed in the chapters pertaining to specific experiments.

With $I_0(E)$ determined as outlined above, $\chi(E)$ can then be formed as

$$\chi(E) = (I(E)/I_0(E)) - 1. \qquad (2)$$

Other descriptions of this data reduction process can be found elsewhere.[4] The extraction of structural information from this data can proceed by either of two methods-- comparisons to theoretical calculations or EXAFS-like Fourier transform analyses. Examples of both methods will be discussed in the following chapters.

3.4 Experimental angle determination

The determination of the necessary angles comprising a particular experimental geometry also deserves some comment. At present, these angles are determined by aligning the crystal normal to a viewport of the experimental chamber using He-Ne laser auto-collimation. The angular position of this window is then used to set electron emission angle (determined by the analyzer position) employing an angular scale marked on the analyzer carriage. This could be improved by directly aligning the crystal with the analyzer. A method of performing this alignment, by mounting an alignment tube directly on the analyzer is currently planned. This will allow positioning of the crystal directly normal to the analyzer to be accomplished to much less than 1°. Since the estimated errors of 2-3°in the present procedure arise mainly due to possible errors in the absolute positions used to determine the relative angle between the crystal and the analyzer, and not to the precision of movements from the reference points, this should allow for emission angle determinations to within 1°.

REFERENCES

1. Z. Hussain, E. Umbach, D.A. Shirley, and J. Feldhaus, Nucl. Instrum. Methods 195, 115 (1982).
2. S.D. Kevan, Ph.D. thesis, Univ. of Calif., Berkeley (1980).
3. P.A. Lee, P.H. Citrin, P. Eisenberger, and B.M. Kincaid, Rev. Mod. Phys. 53, 769 (1981).
4. J.J. Barton, C.C. Bahr, S.W. Robey, Z. Hussain, and D.A. Shirley, (to be published).

FIGURES

Fig. 1 Schematic illustration of the major components employed for ARPEFS measurements in this thesis. Synchrotron radiation is collimated at the entrance slit to reduce the bandpass. The beam is then incident on a toroidial mirror which focusses in two dimensions onto the sample. Prior to the sample, the beam is monochromatized by Bragg reflection from a pair of matched Ge crystals. The photoelectrons are collected in an angle-resolving electron energy analyzer.

Fig. 2 This figure illustrates a typical measured inelastic background. The inset gives a typical core level spectrum along with the results of a fit to extract the peak area, as described in the text.

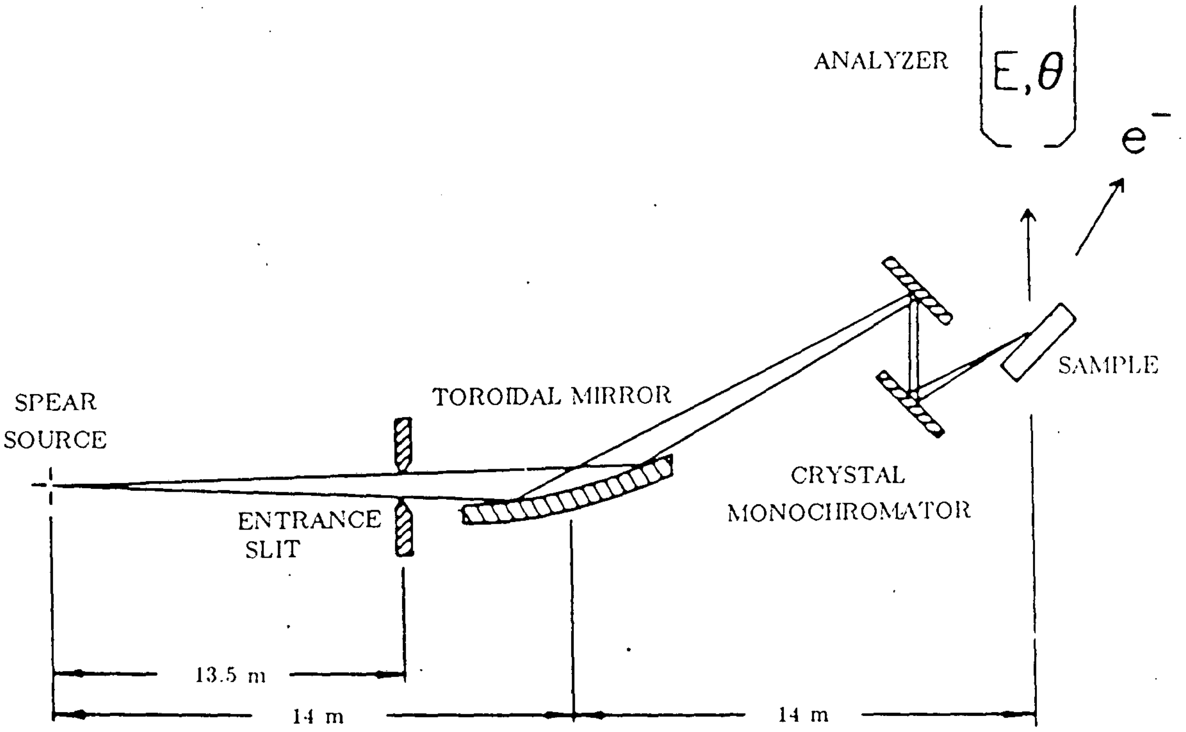

XBL 864-1299

Fig. 1

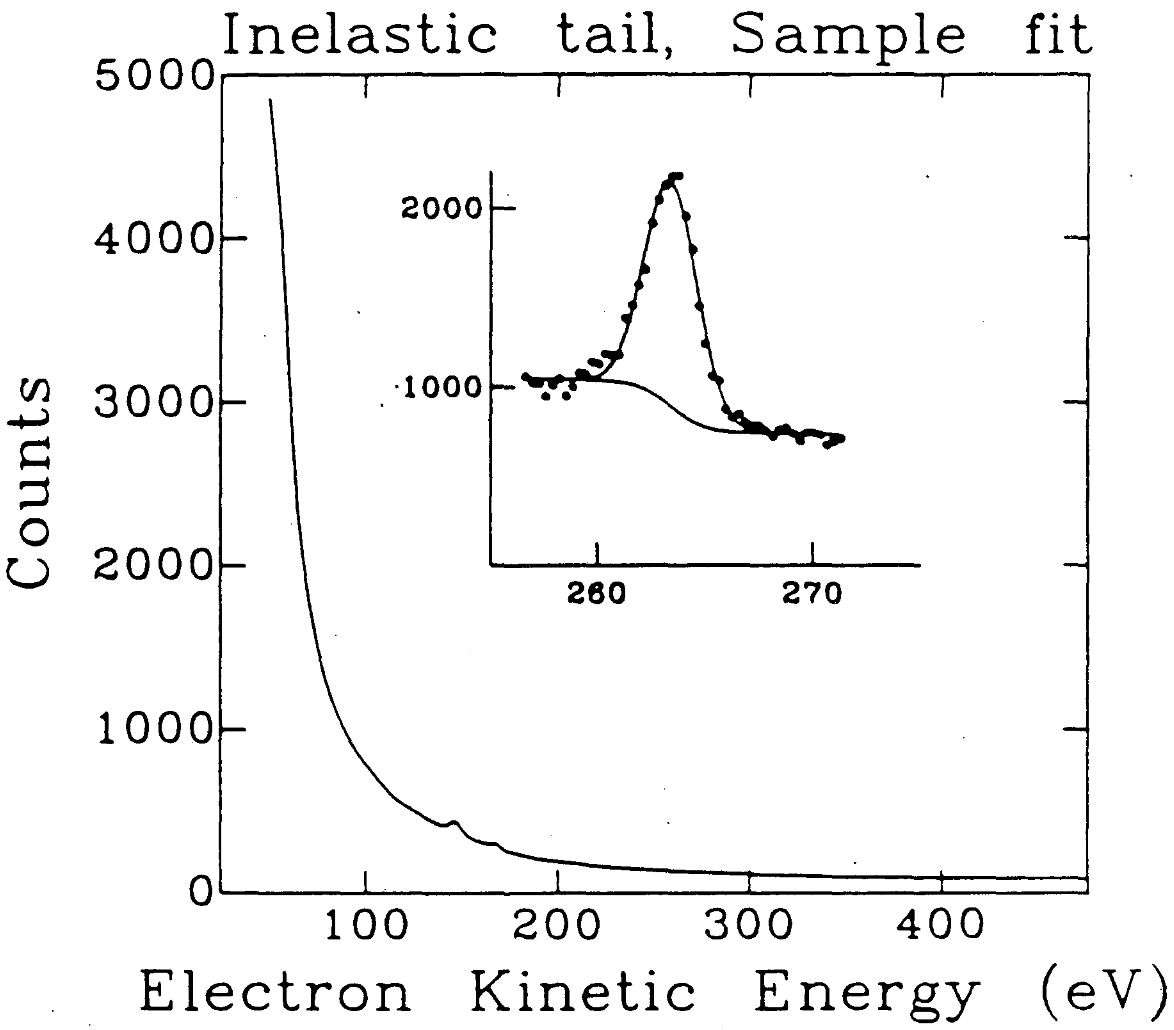

XBL 864-1300

Fig. 2

CHAPTER 4

An ARPEFS Investigation of c(2x2) S/Ni(011)

ABTSTRACT

Measurements of the extended fine structure in the photoemission intensity from the S(1s) core level were performed for a c(2x2) overlayer of S on Ni(011). Four experimental geometries were employed, making this the most complete ARPEFS study to date. Surface structural information was extracted from the ARPEFS using a combination of Fourier transform techniques and comparisons to multiple-scattering calculations. The results of this analysis are in excellent agreement with previous studies of this system indicating that S adsorbs in a rectangular hollow site 2.20 ±.02 Å above a second layer Ni atom. We further present evidence for a buckling of the second Ni layer, giving an expansion in the separation between the first Ni layer and the second layer Ni atoms in atopped positions of 11 % from the bulk value, while second layer Ni atoms left unatopped in the c(2x2) structure assume essentially bulk positions. We also examine in detail the effects of multiple scattering on the extraction of this structural information from ARPEFS and present results for surfaces with S coverages greater than 1/2 ML.

4.1 Introduction

In this chapter we report ARPEFS experiments based on photoemission from the S(1s) level in the system c(2x2) S/Ni(011). This research was motivated by several goals, all of which are meant to provide a critical evaluation of the ability of the ARPEFS technique to provide surface structural information. First, the c(2x2) S/Ni(011) was chosen in part because it has been well studied in previous LEED[1,2] and ion-scattering[3] experiments. This system therefore provides a stringent test for ARPEFS to generate a unique, accurate, and correct surface structure. In this context, for example, the ion-scattering analysis indicated an expansion of the first Ni interplanar separation by 6%. To be competitive, ARPEFS would have to confirm this result.

Second, the analysis of the ARPEFS data can be performed at three levels of increasing sophistication. Two of these are derived directly from the EXAFS-ARPEFS analogy. The first is based simply on Fourier transforming $\chi(k)$ to form a spectrum, F(r), with intensities at various "path length diferences". These distances can then be compared with expectations based on trial geometries. A second, more quantitative, level consists of selecting a peak in F(r) that arises mostly from one path length difference, if one is available, and back-transforming to derive the value for that distance. At the third level, the ARPEFS data are fitted with a theoretical curve for which structural parameters are thereby optimized. Our goal in analyzing the c(2x2) S/Ni(011) data is to ascertain the extent and validity with which structural information can be obtained from each level of analysis. Until now this question has been uncertain and even controversial, for lack of adequate data.

Previous ARPEFS studies[4,5] have concentrated on data taken for high symmetry crystallographic directions. However, there is no reason to expect that the adsorption site will maintain the bulk symmetries, especially when considering more complicated systems. This study has attempted to select experimental geometries which help elucidate the surface structure.[6]

The remainder of this chapter is organized as follows. Section 4.2 describes experimental details and also provides a brief description of the reduction of the raw data to the $\chi(k)$ form. It concludes with the presentation of $\chi(k)$ curves for the c(2x2) S/Ni(011) system collected for several experimental geometries. Section 4.3 discusses the analysis of the data, first using Fourier transform methods, followed by an r-factor analysis performed using comparsions to multiple-scattering calculations. In Section 4.4 we present some results obtained for the S/Ni(011) system at greater than 1/2 monolayer (ML) coverage. A summary and conclusions are given in Section 4.5

4.2 Experimental details

As discussed in Chapter I, the ARPEFS experiment consists of measuring the angle-resolved photoemission intensity from a specific core level-- usually a core level of an adsorbed atom on a clean, single crystal surface-- as a function of the photoelectron kinetic energy. In this section, we present a description of the ARPEFS measurement for c(2x2) S/Ni(011). First, we will describe the the sample preparation procedures and provide a description of the geometries employed to obtain the ARPEFS data. We conclude with the presentation of the $\chi(k)$ curves for these geometries.

4.2.1 Sample preparation

The Ni(011) crystal was cut (7x7x1mm) from high purity (99.999%) single crystal stock, and mechanically polished to within <1° of a (011) orientation as determined by Laue backscattering. It was then chemically etched[7] before mounting on a high precision sample manipulator for insertion in the experimental chamber. The manipulator allowed linear motion along three perpendicular axes as well as rotations about both an axis in the crystal surface and about the crystal normal. Sample heating was accomplished by electron bombardment from a tungsten filament located behind the Ta sample plate on which the Ni crystal was mounted. Temperatures were measured using an infrared pyrometer.

After installation in the experimental chamber, which maintained a typical pressure of 2×10^{-10} torr, the crystal was cleaned by repeated cycles of argon ion etching and annealing to 800°C. This procedure was sufficient to remove all impurities except carbon. The carbon was then removed by heating the crystal to 700^{0}C after exposure to 1×10^{-8} torr of O_2 for several minutes. Auger electron measurements were performed using a set of four-grid LEED optics in the retarding field mode. These measurments showed no detectable traces of carbon, oxygen, or sulfur. The c(2x2) overlayers of sulfur were formed by ambient exposure of approximately 1.5-2 L of H_2S, followed by annealing to 150^{0} C. Auger measurements for the c(2x2) structure showed no trace of impurities other than sulfur. The ratio of the S(152 eV) Auger intensity to that of Ni(61 eV) was about 0.2, and was reproducible for the overlayers prepared for the ARPEFS measurements.

4.2.2 Geometries

ARPEFS measurements were performed for several different experimental geometries. The emission and photon polarization angles for each geometry were determined as described in Chapter 3 by He-Ne laser auto-collimation through the experimental chamber viewports. The angles determined in this manner have an estimated accuracy of ±2°.

The experimental geometries employed in performing the ARPEFS measurements, described below, are illustrated in Fig. 1. This figure depicts a section of the [011] Ni surface, indicating the photoelectron emission angles for which ARPEFS data were collected. We include the S atoms in the rectangular hollow site. This will be shown to be the correct adsorption site in the analysis below. The geometries are as follows:

(a) Emission along the surface normal. The photon polarization vector was directed 40° from the surface normal toward [100].

(b) Photoelectron emission 38° from the surface normal toward [100] with the polarization 78° from the normal toward [100].

(c) Emission 50° from the surface normal toward [100]. The polarization vector was in the surface along [100].

(d) Emission along [001]. The polarization was 75° from the surface toward $[0\bar{1}1]$.

The normal emission data primarily contains information about near-neighbor atoms below the adsorbed sulfur atom. Geometries (b), (c), and (d) were chosen to provide sensitivity to atoms on either side of the adsorbed sulfur-- in particular, first layer near-neighbor Ni atoms. The combination of geometries (a) and (c) will be shown to be sufficient to define the adsorption site. Geometry (b) was chosen to investigate the changes in the ARPEFS with moderate angle changes, and geometry (d) was chosen for comparison to normal emission data from c(2x2) S/Ni(001).[8] For geometries (b) and (c), the azimuthal angle was ~ 3° from [100] due to limitations of the sample motion.

For each geometry a series of photoelectron spectra at different kinetic energies were collected using an 18 eV energy window which included the S(1s) core level. The reduction of these data to $\chi(E)$ curves was described in Chapter 3. For Fourier transform data analysis, it is necessary to convert $\chi(E)$ to $\chi(k)$. The photoelectron kinetic energy, E, measured outside the solid is related to the wavenumber of the photoelectron inside the solid by

$$k = 1/h\,[2m_e(E+V_0)]^{1/2}, \qquad (3)$$

where m_e is the electron mass and V_0 is the inner potential of the solid. The value of V_0 is typically about 10 eV, but the exact value is unknown and is slightly energy dependent for ARPEFS energies. The inner potential is therefore treated as an adjustable parameter. The $\chi(k)$ curves for each of the geometries indicated in Fig. 1 are presented in Fig. 2. An inner potential of 10 eV was used for this figure.

4.3 Data analysis

The most general method of analysis that can be employed to extract structural information from ARPEFS data involves applying procedures similar to those employed in LEED studies. The data are compared to calculations using an appropriate reliability factor as a quantative measure of the level of agreement. The geometry assumed in the calculation is then varied until a minimum is located in the r-factor, indicating the best agreement between theory and experiment. The results of such an analysis using comparisons to multiple-scattering calculations will be presented in Section 4.3.2 However, consideration of the form of Eq. (1) compared to the analogous expression describing EXAFS[9] presents the possibility of using more direct Fourier transform techniques. This approach was suggested in the work of Lee[10], and later an exploratory study of its applicability was performed by Hussain et al.[11], using theoretical simulations of ARPEFS data to obtain an adequately long data range.

The application of Fourier transform techniques to extended data range ARPEFS data was first performed for c(2x2) S/Ni(001).[4] This work indicated that Fourier transform techniques can yield useful information. We shall evaluate the extent to which this relatively simple, direct analysis can provide information about the adsorption geometry of c(2x2) S/Ni(011). We will also examine the effect of multiple scattering on the extraction of this information.

4.3.1 Fourier transform analysis

This subsection will be further divided into three parts. First we present a qualitative discussion of the Fourier transforms of ARPEFS data for c(2x2) S/Ni(011) based on the ideas presented in Chapter 2. This will be followed by a quantitative analysis employing the filtering and backtransform procedures developed for the treatment of EXAFS data.[9] Finally, we will illustrate the effects of multiple scattering that are evident in these data.

a) Qualitative discussion

Considering the form of $\chi(k)$ given in Eq. 1, and the above analogy with EXAFS, one would expect peaks to appear in the Fourier transform of this function at positions given by the path length difference, $\Delta R_j = r_j(1-\cos\Theta_j)$, for scattering from neighboring atoms. For a given scattering atom, this path length difference changes with the electron emission angle, leading to different structure in the Fourier transform for each different emission angle. Data taken for several emission angles should allow one to establish the adsorption site through comparison of the Fourier transform to expected path length values for trial sites, provided the Fourier transforms can be interpreted in a reasonably simple manner.

The positions of the peaks in the Fourier transform will differ slightly from the value of ΔR_j, due to the additional scattering phase shift ϕ_j. However, this phase shift is nearly independent of k, with only a small linear contribution leading to small shifts. Large shifts in ΔR_j can occur when there is strong structure in the phase shift, as happens when the scattering angle approaches a value for which there is a zero in the scattering amplitude-- the Generalized Ramsauer-Townsend resonance.[12] This complication can be studied independently by considering the angle and energy dependence of the appropriate complex scattering amplitude.

We now turn to an examination of the S/Ni(011) data. Fourier transforms of the normal emission, the 38°, and the 50° data are presented in Fig. 3. Most of the structure in these transforms is due to ARPEFS. The discussion which follows will concentrate on the dominant features in each transform.

The normal emission transform is dominated by a strong peak at 4.2 Å with smaller structure at approximately 3 Å and 7.5 Å. The data set taken with an emission angle of 50° shows a strong peak at 4.1 Å, though this peak is significantly weaker than the 4.2 Å peak in the normal emission (the 50° transform is scaled by a factor of two). This geometry also gives structure in the 1-2 Å range and at 8 Å. Data taken with an emission angle of 38° yield two dominant peaks, at ~ 1.2 Å and 3.7 Å.

Inspection of these Fourier transforms, coupled with the ideas presented in Chapter 2 and consideration of the plausible adsorption sites for S on the Ni(011) surface-- atop on the first layer, short bridge, long bridge, or rectangular hollow-- leads to the conclusion that adsorption occurs in the rectangular hollow. The atoms giving dominant contributions to this structure can be identified with reference to Fig. 4. The very strong 4.2 Å peak in the normal emission data is due to backscattering from the 2nd layer Ni atom labeled (2) in Fig. 4. The intensity in this backscattering peak is considerably enhanced due to forward scattering through the sulfur atom. The 4.1 Å peak in the 50° data is dominated by scattering from two symmetrically equivalent atoms in the first Ni layer which have scattering angles of ~ 144°, close enough to backscattering to maintain a reasonably large scattering amplitude. These atoms are labeled (1) in Fig. 4. The peak at 3.7 Å in the 38° data is also due almost exclusively to these same atoms. The reduction in intensity of the 38° peak relative to that in the 50° case is consistent with a decrease in the scattering amplitude in going from ~ 144° scattering for the 50° geometry to ~ 137° scattering for the 38° data.

Additionally, the structure at 3 Å in the normal emission data strongly supports adsorption in the rectangular hollow. The other sites do not provide an explanation for this peak, which has a shorter path length difference than the dominant 4.2 Å peak at normal emission. For the rectangular hollow this structure is easily explained in terms of scattering from the four near-neighbor Ni atoms in the first layer. Thus, by examination of the Fourier transforms, we find convincing evidence that the S adsorption site is the rectangular hollow, in agreement with the previous ion scattering and LEED experiments. The Fourier transform structure is inconsistent with other possible adsorption sites. Although other sites could provide explanations of the structure for one geometry, a combination of two data sets (in particular the normal emission and 50° data) decidedly favors the rectangular hollow site.

b) Filter and backtransform analysis

Having identified the adsorption site, and thus the particular atoms contributing to the dominant peaks in the Fourier transform for each geometry, more precise quantative information can now be obtained by employing the filtering and backtransform analysis procedures developed for EXAFS data.[9] The analysis consists of windowing the Fourier peak of interest, backtransforming this peak and extracting the experimental phase function. The total phase function, ϕ_T, is given by the argument of the cosine in Eq. (1),

$$\phi_T = kr_j(1-\cos\theta_j) + \phi_j. \tag{5}$$

If the appropriate theoretical scattering phase shift, ϕ_j, is removed, the remaining function is linear in k with a slope given by $\Delta R_j = r_j(1-\cos\theta_j)$, the desired path length difference. A complication exists due to the unknown value of V_0, the inner potential. This parameter must be used to convert the experimentally determined electron kinetic energy outside the solid to the wavenumber inside the solid. The inner potential is thus treated as an adjustable parameter which is varied until the most linear function, $kr_j(1-\cos\theta_j)$, is obtained.[9]

The results of this analysis, performed on the 4.2 Å peak in the normal emission data, the 3.7 Å peak in the 38° data, and the 4.1 Å peak in the 50° data, are presented in Table I. These structures were chosen because they are overwhelmingly due to single or symmetrically equivalent atoms, so that a single path length difference can be extracted in each case. The other large peak in the 38° data at 1.2 Å is not treated because this structure cannot be easily identified with a single scattering path length. Also, since this structure is in the low path length region, it is strongly influenced by the data reduction procedures as discussed in Section 4.2.

The path length given by

$$\Delta R_j = 4.36 \text{ Å} = r_j(1-\cos\Theta_j),\ \Theta_j=\pi \qquad (6)$$

for the normal emission data indicates a bond length of 2.18 Å between the S and the Ni atom in the 2nd layer directly below. The data taken off-normal deserve some comment due to the 3° azimuthal rotation from the plane containing [100]. The major effect of this misalignment will be to produce two slightly different scattering paths, instead of two symmetrically identical paths, contributing to the large peak at 4.1 Å. However, the small difference between these two paths is well beyond the resolution of the measurment. Since the change in the scattering phase shift and amplitude for the two different scattering angles is small, the analysis will produce a value of the path length which is the average of the two values and, within the accuracy of the experiment, is equivalent to the value that would be obtained with no azimuthal rotation. With this in mind, the value of 4.18 Å for the path length difference in the 50° data indicates, after some simple geometric considerations, a bond length between the S atom and the near neighbor atoms in the first Ni layer of 2.31 Å. Alternatively, this is equivalent to specifying a value of 0.82 Å for $d_{\perp}$, the height of the sulfur atom above the first nickel layer.

The value extracted for the weaker 3.7 Å peak in the 38° data, corresponding to scattering from the same set of two atoms as for the 50° case, is 4.02 Å. The larger shift of the peak in the Fourier transform from the backtransformed value, compared to the previous two cases, is partially due to the previously mentioned Generalized Ramsauer-Townsend effect. The ~ 137° scattering angle for the structure in the 38° data is close enough to a zero in the Ni scattering amplitude at 129° to produce a larger shift. However, the path length value obtained from the backtransform analysis is of primary importance, and this value is in good agreement with the value of 4.00 Å that is predicted based on the 2.31 Å bond length determined from the 50° data. Thus, considering the smaller amplitude of the structure in the 38° data, the results of the backtransform analyses show very good consistancy between the two independent measurements. The errors indicated in Table I, and also in Table II below, are based on the precision of the procedure and estimations of the effects of errors in the theoretical phase shifts and errors in determining experimental angles.

With the bond lengths of the S atom to its near neighbors in the first and second Ni layers known, the details of the adsorption site can now be determined. As stated, the 2.31 Å bond length to the first layer Ni atoms indicates a value of $d_{\perp}$= 0.82 Å. This value, in conjunction with the value of 2.18 Å for the S-2nd Ni plane separation, then provides a value of 1.36 Å for the interplanar separation between the first and second Ni layers. This represents an expansion of this separation by 9 % from its bulk value of 1.245 Å. Table II summarizes the results of this analysis and also presents the results of the previous ion scattering experiment for comparison. In this table, S-Ni_1 and S-Ni_2 represent the bond lengths to atoms (1) and (2) in Fig. 4, respectively. The parameter d_{12} is the interplanar separation between the first and second Ni layers and Δ% is the percent change in this spacing from the bulk value.

The excellent agreement of the backtransform analysis with the ion scattering experiment supports the previous assignments of the dominant structure in the Fourier transforms. This also supports the idea that Fourier transforms for an unknown system can be interpreted in a reasonably simple manner, thus aiding in determining the adsorption site and, in favorable cases, allowing the extraction of bond lengths. The ability to use this attractive feature of the ARPEFS technique does, however, require careful consideration of the possible adsorption geometries so that the experiment can be devised to make best use of the strong modulation which will normally occur for near-backscattering geometries to distinguish between possible sites. For instance, although the Fourier transform of the 38° data provides information that is helpful in determining the adsorption site, the stronger structure in the 50° data is clearly preferable.

c) Multiple scattering effects

Before turning to an r-factor analysis of the data, we will illustrate the evidence for multiple scattering displayed in this data. As noted previously, the backtransform analysis requires the removal of the scattering phase shift, ϕ_j. As in the case of the scattering amplitude, the phase shift also requires the consideration of multiple-scattering. In addition to enhancing the intensity of a single scattering, forward scattering events will also add contributions to ϕ_j. This affects primarily the normal emission data-- the backscattered wave from the 2nd layer Ni atom must necessarily be forward scattered through the S atom as it propagates to the detector. The backtransform analysis of the normal emission data has accounted for this effect by employing a double-scattering phase shift. An attempt to analyze these data using only the single backscattering phase shift, $\phi(\pi)$, leads to a path length value of 4.40 Å instead of 4.36 Å, but more importantly, it also requires a non-physical value of $V_0 \approx 30$ eV to fit the data. Thus a single-scattering model attempts to compensate for the approximately constant additional phase shift due to double scattering by variation of the V_0 parameter outside an acceptable range.

We further illustration of this effect in Fig. 5. The large dot curves in Figs. 5(a) and (b) represent the filtered and backtransformed data for the dominant peaks in the 50°and normal transforms, respectively. The solid curve in Fig. 5(a) shows a theoretical simulation of the backtransformed 4.1 Å peak in the 50°data. As stated, this peak should be well described with single scattering. The solid curve was calculated using a single scattering model,

$$\chi(k) = 2\,N\,e^{-\Delta R_j/\lambda}\,e^{-\sigma_j^2 k^2 (1-\cos\Theta_j)}\,\cos(kr_j(1-\cos\Theta_j)+\phi_j). \qquad (6)$$

The value of λ, the electron mean free path, was obtained from the values of Seah and Dench[13] and σ_j^2, the appropriate mean-squared realitive displacement due to thermal vibrations, was then determined by the best fit to the backtransformed data. The value of σ_j^2 thus obtained was 0.009 Å². The values for the number of contributing atoms, N = 2, and the path length difference, $\Delta R_j = 4.18$ Å, are known. The important point is that reasonable values of λ and σ_j yield a good simulation of the backtransformed data, as shown in Fig. 5(a).

Considering now the normal emission data in Fig. 5(b), we expect that with λ and σ_j taking values close to those which provided a good simulation of the 50° data, we should obtain a qualitatively similar simulation for this data. The fact that the scattering events contributing to the 4.1 Å peak in the 50° data are in the surface layer while the scattering atom which dominates the normal emission peak at 4.2 Å is in the second layer would be expected to lead to somewhat different values for the thermal vibrations. However, both cases involve atoms which are near neighbors so that the difference should not be large. The result, assuming only single scattering, is presented as the solid line in Fig. 5(b). It can be seen that the data show a much larger amplitude and there is also a large, approximately constant, phase shift. The same V_0 value was used to convert the photoelectron kinetic energy to wavenumber, k, in both the normal emission and the 50° case, V_0= 9 eV. Correction of the remaining large phase shift error again requires a value of $V_0 \approx$ 30 eV if the single scattering model is forced to fit the data.

The dot-dash line in Fig.5(b) presents the result of the same simulation, but including the effect of the additional multiple-scattering through the intervening S atom. This simulation also included an exact treatment of the spherical wave scattering. The agreement is much better in this case and nearly as good as that provided by the 50° example. Thus, it is clear from the magnitude of these effects that multiple-scattering must be included if quantative interpretations of ARPEFS are sought.

4.3.2 Multiple scattering calculations

The Fourier transform analysis presented in the previous section concentrated primarily on only the dominant structure in the transforms. There is also weaker structure in the transforms which indicates that the ARPEFS contains additional structural information. In fact, partial explanations can be offered for this weaker structure as follows. The structure at 7.5 Å in the normal emission data has a large contribution from four symmetrically placed atoms in the 3rd Ni layer-- (3) in Fig. 4-- while the peaks in the 7-8 Å range for the 38° and 50° data are largely due to near backscattering from atom (4) in the 2nd layer. The low path length structure in the off-normal data is caused by the atoms in the first Ni layer in front of the adsorbed S atom, with additional contributions from near-neighbor S atoms, although mixed with low frequency experimental noise. These explanations are not meant to imply that the scattering atoms identified with a given peak are necessarily the sole contributions to the intensity in that path length range, only that the structure in this range has large contributions from these sources. Attempts to extract structural information using filtering and backtransform techniques are not wholly satisfactory due to weakness of the structure and inadequate resolution to separate several similar scattering path lengths. An alternative approach to the analysis consists of direct comparison of the $\chi(E)$ curves to theoretical curves calculated assuming a specific adsorption geometry, in a manner analogous to the treatment of LEED data. This method provides a straightforward means of testing the data for additional, less dominant structural parameters. Even here, however, the ability to interpret the Fourier transforms in a relatively simple manner provides a useful guide in assessing to which structural variables an experimental geometry will be most sensitive.

In this section we present the results of such an analysis based on comparisons to multiple-scattering, cluster calculations. These calculations are described in detail elsewhere.[14,15] A brief outline of the major features will be presented here.

As discussed above, a quantitative theory of ARPEFS requires the inclusion of important multiple-scattering and spherical wave effects. The cluster calculations performed in this work have included multiple scattering to fourth order as well as the dominant corrections to the plane wave approximation due to the spherical nature of the photoelectron wave using the approximations presented by Barton et al.[15] The finite mean free path was treated as an exponential damping factor, $e^{-r/\lambda}$, with $\lambda=ck^n$, where normally $n=1$. The value of c was determined by fitting to the values given by Seah and Dench[13] for Ni. Thermal effects were treated using a correlated Debye model which accounted for increased thermal vibrations near the surface and anisotropies in different crystallographic directions.[14] The inputs to this model were determined using theoretical calculations of the mean square displacements for the Ni(011) surface[16] as a guide. The bulk Debye temperature, Θ_D^b, was taken as 390 K, and the Ni surface Debye temperatures were set at 270 K, 270 K, and 310 K, for the [011], [100], and $[1\bar{1}0]$ directions respectively. The Debye temperatures for the sulfur overlayer were assumed to be given by the Ni surface values appropriately adjusted for the difference in masses, giving 365 K, 365 K, and 420 K for the [011], [100], and $[1\bar{1}0]$ directions. The ±3° angular resolution of the experiment was included as described in Ref. (14). The effect of the inner potential was included as an energy independent shift of the kinetic energy scale.

The phase shifts used in these calculations were computed using a modified version of the program developed by Pendry for LEED.[17] The Ni potential was obtained from the self-consistent LDA calculations of Moruzzi et al.[18] The S phase shifts were calculated using a potential obtained from atomic Hartree-Fock wavefunctions. The wavefunctions were truncated and renormalized at a muffin-tin value R_{max} = 1.05 Å. Several values of R_{max} were tested and produced no strong differences in the results of the analysis. The exchange potential was calculated using an Xα approach with α taken from the work of Schwarz.[19] A total of 16 phase shifts were calculated for each potential for energies up to 500 eV.

The first step in the analysis consisted of smoothing the data by filtering at 10 Å. Calculations were then be performed including a cluster size large enough to include all path lengths with values ≤10 Å. For the off-normal geometries, the low path length structure less than 2 Å was filtered due to uncertainties in measuring this structure. The calculations were then performed using these same low path length cutoffs.

For the present analysis, a simple r-factor was chosen. It consists of forming

$$r = \int [I_e(E)-I_t(E)]^2 \, dE \,/\, \int I(E)^2 dE \qquad (7)$$

Here $I_e(E)$ is the intensity of the experimental curve as a function of the energy and $I_t(E)$ is the intensity of the theory. The analysis proceeded by assuming an adsorption geometry and performing the multiple-scattering calculation. The level of agreement between the theory and experiment was evaluated by calculating r. The geometry was varied until a minimum in r was located. For each geometry comparisons were made to calculated curves with V_0 values of 8, 10, and 12 eV. The r factors determined in this manner were then averaged to give a final r value. This r-factor is simple by present day LEED standards,[20] but nonetheless provided consistent results for the values of parameters obtained from different experimental curves. Due to the ± 2-3° accuracy with which experimental geometries are determined, the emission angle was varied to obtain the best simulation of the experimental curves. The angles obtained were within 3° of the expected value in all cases. The final structural parameters determined by the r-factor analysis were only slightly (~ 0.02 Å) dependent on the angle used, except for the determination of $d_\perp$ (the distance of the sulfur atom above the Ni surface) from the [001] data. For this geometry, there are several Ni near-neighbors which have scattering angles of ~ 129°-- two atoms in the first Ni layer and the

Ni atom directly below the S atom. This angle is very close to the scattering for which the Generalized Ramsauer-Townsend resonance is observed in Ni.[12] The scattering amplitudes and phases of these atoms thus depend strongly on the scattering angle, or equivalently, the emission angle. The minimum in the r-factor was found to shift by 0.07 Å for angle changes of 3°. However, the value of $d_\perp$ = 0.81 Å presented below for an emission angle of 45° had an r-factor minimum that was slightly lower than those found for other angles.

In Fig. 6 we present a comparison of the filtered normal emission data to calculations performed for several different values of the S-to-2nd layer Ni distance (S-Ni_2). The strong dependence on this parameter is evident, clearly indicating by visual inspection that the curve for a value of 2.2 Å is much closer to experiment than those for 2.1 Å or 2.3 Å.

Figs. 7 and 8 show the optimized calculations compared to the filtered data for all experimental geometries. The agreement ranges from good to excellent, with the exception of some portions of the [001] curve. As discussed above, much of the structure in this data set is strongly influenced by scattering at angles near a resonance in the Ni scattering amplitude. The results for this geometry are thus more sensitive to the input scattering phase shifts and errors in the experimental angles.

Plots of the r-factor obtained by varying the S-Ni_2 and $d_\perp$, for each geometry, are given in Figs. 9 and 10 respectively. The results are summarized in Table III. There is very good consistency between the values obtained for each data curve, as well as good agreement with results of the Fourier transform analysis presented previously. The values obtained by averaging the results for each geometry are indicated in the last column. A value of 2.20 ±0.02 Å is determined for S-Ni_2 compared to 2.18 ±0.02 Å found for the Fourier transform analysis. This analysis also indicates an expansion of (11 %) in the first Ni interplanar spacing. The exception to this consistent agreement is the value of the S-Ni_2 distance obtained from the 50° data, which indicates a value ~ 0.1 Å lower than the other values. This is outside the expected deviation based on the values obtained from the other curves. Thus, the value of S-Ni_2 for the 50° data was not included in the averaged value. A possible explanation for this discrepancy will be discussed below.

Having obtained very good agreement in the major structural pararmeters with the Fourier transform results, we can now extend this r-factor analysis and try to obtain additional information. As indicated earlier, there is less intense structure in the Fourier transforms of the data, for which partial explanations have been offered. This structure provides a guide for testing the ARPEFS for further information. However, before proceeding to such an analysis, we will first comment briefly on the use of single-scattering versus multiple-scattering theories for this purpose.

Fig. 11 contains a comparison of data taken at normal emission and at 50° with the optimized results obtained for multiple-scattering (MS) and single-scattering (SS) theories. It is clear that the SS calculation provides good reproduction of the features in the experimental data for both geometries, though the quantitative agreement is better for the MS case. This is particularly true for the normal emission data. An r-factor analysis performed using SS calculations produces results that are similar to those obtained from the theory which includes the dominant multiple-scattering effects, but with shifts of 0.05 to 0.1 Å. The most pronounced example of this is illustrated in Fig. 12. This figure contains plots of the r-factor obtained for variation of the S-Ni_2 distance for the normal emission data, using single-scattering and multiple-scattering calculations. There is a shift of the SS minimum to a value indicating a S-to-2nd layer Ni bond length of 2.27 Å, 0.07 Å larger than the value obtained from the multiple-scattering analysis. This is, of course , another illustration of the effect of neglecting the double scattering phase shift discussed in section 4.3.1(c). In general, structural parameters obtained from a SS analysis will vary by 0.05 to 0.1Å with the experimental geometry, depending on whether or not there are important multiple scattering contributions-- particularly additional forward scattering events. The apparent values of non-structural parameters which determine intensities, such as the electron mean-free path and σ_j^2, will also appear to be dependent on the geometry, due to the forward scattering enhancement discussed previously. Because the values given in Table III indicate that the precision (and most likely accuracy also) in the measurements is below the 0.1 Å level, and because we are interested in investigating the possibility of obtaining structural information on this scale, the inclusion of at least the dominant multiple-scattering effects is necessary. However, the simplicity of the SS calculations makes them very attractive for performing a preliminary analysis or for use in cases where possible errors on the order of 0.1 Å are not important.

We now discuss the results of efforts to obtain additional structural information. In particular, we wish to consider a possible explanation of the discrepancy noted previously in the value of S-Ni_2 obtained from the 50° data. The Fourier transform for this geometry exhibits a relatively strong feature at 8 Å which is due primarily to scattering from the 2nd layer Ni labeled (4) in Fig. 4. The photon polarization was directed within 12° of this atom and the scattering was very close to backscattering. In contrast the 2nd layer Ni atom directly below the S atom lies in the nodal plane of the outgoing photoelectron p-wave. Thus, this geometry is sensitive to the distance to the second Ni layer as measured to the uncovered Ni atoms, whereas the normal emission case is very sensitive to the Ni atom directly below the S atom. The results presented in Table III thus suggest the possibility that Ni atoms in these two sites are inequivalent, with the uncovered Ni_2 atoms ~ 0.1 Å higher than the atopped Ni_2 atoms.

We have tested this explanation by performing additional calculations considering a buckled second layer. For the 50° data, a minimum in the r-factor was found for a buckling which placed the uncovered Ni atoms 0.13 Å higher than the atopped Ni atoms, thus giving a value of the distance to the first Ni plane for the uncovered site which is essentially the same as a bulk interplanar separation. The 38° data also exhibit a lowered value of the minimum in the r-factor for a buckling of 0.13 Å. The normal emission data shows very little sensitivity to the buckling, as would be expected since the photon polarization was directed nearly perpendicular to the surface, and the [001] data indicate a minimum for no buckling. Considering the much better fits obtained for the 38° and 50° data relative to the [001] data, for the reasons mentioned previously, we feel that these results support the possibility of a buckled second layer.

The existence of a buckling of this nature is easy to accept. There is no a priori reason to expect the uncovered and atopped 2nd layer Ni atoms to assume equivalent positions. One might expect that the uncovered site would be closer in structure to the clean Ni surface, for which it is known that the 1st interplanar separation is contracted by 5-10 %[4,21] relative to the bulk, as compared to the expansion seen in the sulfur atopped site. This would lead to the uncovered 2nd layer Ni atoms assuming a position closer to the first Ni layer than the atopped atoms, as suggested by the data.

As a final case displaying the possibility of additional information, we consider the normal emission data. As indicated earlier, the peak at ~ 7.5 Å in the Fourier transform of the normal emission data has a large contribution due to scattering from 4 atoms in the 3rd Ni layer. This suggests that the data for this geometry might provide some indication of the interplanar separation between the 2nd and 3rd Ni layers. Calculations were performed to test this hypothesis, and the results are presented in Fig. 13. These calculations were performed with a buckled 2nd Ni layer as described above. The parameter, d_{23}, on the horizontal axis of Fig. 13, then represents the separation between the 3rd layer Ni atoms and the 2nd layer Ni atoms in the atopped position. The r-factor values are given for two normal emission measurements and also for the 38° data. Both normal emission results indicate a broad minimum which is contracted from the bulk value. However, the deviation in the results obtained from the two measurements is approximately of the same magnitude as the apparent contraction. The 38° data indicate a value which is essentially the same as the bulk value. Note that the vertical scale for Fig. 13 is decreased by a factor of 2 relative to those in Figs. 9 and 10. Thus, the minima displayed for the variation of this parameter are very broad on the scale of most of the curves displayed in Figs 9 and 10, and are more similar to the r-factor curve exhibited for variation of $d_{\perp}$ for the normal emission data in Fig. 10. The other two experimental geometries exhibited even less sensitivity to the variation of d_{23}, and thus are not displayed. The broad minima exhibited in this figure indicate that the changes produced by variation of this parameter are slight, and are thus susceptable to errors in the data and use of a rather simple r-factor. On balance, however, a simple average of these results, applying equal weight to each of the measurements, indicates a value of this separation which is contracted from the bulk value by 3 ±4 % (0.04 Å). This further means that the separation between the 3rd layer Ni atoms and the 2nd layer, unatopped Ni atoms is expanded by ~ 7 % due to the buckling. Continuing the analogy to the clean surface, this is to be compared with an expansion of 3-4 % in the 2nd to 3rd layer separation determined for clean Ni on the basis of LEED and ion scattering data.[21]

4.4 Higher coverage results

We also studied the adsorption of S on Ni(011) for coverages above 1/2 ML. As S is adsorbed beyond the c(2x2) or 1/2 ML point, distinct changes are observed in the LEED pattern. The (1/2,1/2) spots become elongated in the $[0\bar{1}1]$ direction, finally splitting to form a doublet. The separation between the two spots forming the doublet increases with increasing S coverage.

This behavior was observed in several earlier studies and two explanations for the doubled (1/2,1/2) spots were proposed. Perdereau et al.[22] suggested that continued S adsorption was accompanied by a homogeneous decrease of the S-S distance in the $[0\bar{1}1]$ direction. This results in a surface on which many of the S atoms are shifted from the rectangular hollow site determined for the c(2x2) structure toward a long-bridge site. One of the spots in the doublet observed in the LEED pattern is then explained by single-scattering while the other is produced by multiple-scattering.

The other, more plausible, model was presented by Mroz.[23] In his work, the doubling of the (1/2,1/2) spot was explained by considering the diffraction from a surface consisting of domains of N sulfur atoms separated by anti-phase boundaries. By calculating the interference function for such a case, Mroz showed that the (1/2,1/2) spots would be split by an amount

$$d = 1/(2N-1), \qquad (8)$$

where d is measured realitive to the distance between the integral order spots in the $[0\bar{1}1]$ direction. The coverage associated with a given splitting, or equivalently, a given domain size, is then determined by

$$\Theta_N = N/(2N-1). \tag{9}$$

ARPEFS data obtained for a S/Ni(011) sample which exhibited a doubling of the (1/2,1/2) LEED spot is presented in Fig. 13. This sample was prepared in the same manner as the c(2x2) samples except that the H_2S exposure was continued until a doubling of the (1/2,1/2) spot was observed. This required ~ 5 L.

The lower curve in Fig. 13, curve (b), gives I(E) for the 38° c(2x2) data presented previously. The upper curve shows data obtained from the higher coverage sample. The curves are identical except for the increased total signal from the higher coverage surface, indicating that the S remains in the rectangular hollow. Using the relative intensity change between the two curves and assuming a coverage of ~.5 ML for the c(2x2) case, we can estimate a coverage of 0.65 ML for the higher coverage sample. With this increase in coverage of 30%, a model such as that proposed by Perdereau et al. would lead to much different ARPEFS due to the large number of S atoms which are shifted out of the rectangular hollow. Thus, these data rule out a homogeneous decrease of the S-S distance in the $[0\bar{1}1]$ direction as suggested by those authors.

We can estimate the domain size, N, by two methods. Using Eq. (8) and the value of d determined from the LEED pattern (d = 0.2 ±0.01), we find N ~ 3. Alternatively, assuming a coverage of 0.5 for the c(2x2) surface and using the increase evident in Fig. 13, we can estimate a coverage of 0.65 ±0.1 ML for the higher coverage surface. Employing Eq. (9), we then obtain N ~ 2. The higher coverage surface is thus determined to consist of anti-phase domains 2-3 sulfur atoms across in the $[0\bar{1}1]$ direction with the S adsorbed in the rectangular hollow site.

4.5 Conclusions

We have presented a study of the surface structure of c(2x2) S/Ni(011) using an analysis of the angle-resolved photoemission extended fine structure. The results obtained employing a Fourier transform analysis and also by comparisons to theoretical calculations are in good agreement, and also agree well the results of previous studies.[1-3] Both methods of analysis enabled us to determine details of the surface structure such as the expansion of the first interplanar spacing reported by the ion scattering experiment.[3] On the basis of the r-factor analysis, we have also suggested the possibility of a buckling of the 2nd Ni layer. Studies of this surface at higher sulfur coverages indicate that additional S is incorporated by the formation of anti-phase domains in the $[0\bar{1}1]$ direction.

The good results obtained using the Fourier transform analysis indicate the usefulness of this method. Consideration of possible adsorption sites should allow one to select experimental geometries which will serve to test these sites by highlighting backscattering from near-neighbors. If proper experimental geometries are chosen, then examination of the Fourier transformed data for different directions can rule out several possibilities. The geometries selected for this experiment attempted to illustrate this point. In fact, examination of the Fourier transformed normal emission data alone provides strong evidence for the elimination of all sites except the rectangular hollow.

However, the ability to plan an experiment which will allow one to most efficiently take advantage of the attractive features inherent in the Fourier transform analyses does require careful consideration of possible sites, and also the energy and angle dependence of the scattering amplitude of the materials involved. This initial planning is probably somewhat more critical to the efficient use of this technique, especially considering the realities of performing experiments at a synchrontron, than for other techniques normally employed for surface structure studies.

The possibility exists that for complicated systems, the structure will correspond to none of the sites that have been considered. Even so, examination of the Fourier transform will provide useful information. Also, the excellent agreement obtained with relatively simple theories will then allow additional structures to be tested. Finally, the very different information which can be obtained for additional experimental geometries will prove to be a great advantage. This will provide the ability to conclusively test additional structures if adequate access to synchrontron radiation is available.

We have also illustrated the effects of multiple scattering on the analysis of ARPEFS data. We have indicated that these effects cannot be ignored in quantitative interpretations. However, the dominant effects are easily understood qualitatively and do not alter dramatically the conceptual simplicity of the single-scattering model.

REFERENCES

1. J.E. Demuth, D.W. Jepsen, and P.M. Marcus, Phys. Rev. Lett. 32, 1182 (1974).
2. P.M. Marcus, J.E. Demuth, and D.W. Jepsen, Surf. Sci. 53, 501 (1973).
3. J.F. van der Veen, R.M. Tromp, R.G. Smeek, and F.W. Saris, Surf. Sci. 82, 468 (1979).
4. J.J. Barton, C.C. Bahr, Z. Hussain, S.W. Robey, J.G. Tobin, L.E. Klebanoff, and D.A. Shirley, Phys. Rev. Lett. 51, 272 (1983).
5. C.C. Bahr, J.J. Barton, Z. Hussain, S.W. Robey, J.G. Tobin, and D.A. Shirley, (to be published).
6. J.J. Barton, S.W. Robey, C.C. Bahr, and D.A. Shirley, 1st Intl. Conf. on the Structure of Surfaces, Berkeley, CA., Springer Series in Surface Sciences 2, ed. M.A. Van Hove and S.Y. Tong, (1985)
7. 30% glacial acetic acid, 30% nitric acid, 10% sulfuric acid, 15% acetic acid.
8. J.J. Barton, C.C. Bahr, S.W. Robey, Z. Hussain, and D.A. Shirley, (to be published).
9. P.A. Lee, P.H. Citrin, P. Eisenberger, and B.M. Kincaid, Rev. Mod. Phys. 53, 769 (1981).
10. P.A Lee, Phys. Rev. B 12, 5261 (1976).
11. Z. Hussain, D.A. Shirley, C.H. Li, and S.Y. Tong, Proc. Natl. Acad. Sci. USA, 78, 5293 (1981).
12. J.J. Barton, Ph.D. thesis, Univ. of Calif., Berkeley (1985).

13. M.P. Seah and W.A. Dench, Surf. Int. Anal. 1, 1 (1979).

14. J.J. Barton, S.W. Robey, and D.A. Shirley, (to be published).

15. J.J. Barton and D.A. Shirley, Phys. Rev. A 32, 1019 (1985); J.J. Barton and D.A. Shirley, Phys. Rev. B 32, 1892,1906 (1985).

16. R.F. Wallis, B.C. Clark, R. Herman, and D.C. Grazis, Phys. Rev. 180, 726 (1969); B.C. Clark, R. Herman, and R.F. Wallis, Phys. Rev. 139, 860 (1965).

17. J.B. Pendry, Low Energy Electron Diffraction, (Academic Press, London, 1974).

18. V.L. Moruzzi, J.F. Janak, and A.R. Williams, Calculated Electronic Properties of Metals, (Pergamon Press, New York, 1978).

19. K. Schwarz, Phys. Rev. B 5, 2466 (1972).

20. M.A. Van Hove and R.J. Koestner, in Determination of Surface Structure by LEED, ed. P.M. Marcus and F. Jona, (Plenum Press, New York, 1984) p.357.

21. M.L. Xu and S.Y. Tong, Phys. Rev. B 31, 6332 (1985); R. Feidenhans'l, J.E. Sorensen, and J. Stensgaard, Surf. Sci. 134, 329 (1983).

22. M. Perdereau and J. Oudar, Surf. Sci. 20, 80 (1970).

23. S. Mroz, Surf. Sci. 83, L625 (1979).

Table I. Path length values (in Å) obtained from the dominant peaks in the normal emission (0°), 38° and 50° Fourier transforms, using the analyses discussed in the text. Note that the analysis consistently produced values of V_0 within 1 eV of each other.

Expt. geometry	ΔR	V_0(eV)
0°	4.36(4)	10
38°	4.02(5)	9
50°	4.18(4)	9

Table II. Structural parameters (in Å) determined from the path length values presented in Table I. A description of the parameters presented is provided in the text. The results of the ion scattering experiment performed by Van der Veen et al in Ref. 9 are included for comparison.

Parameter	ARPEFS	Ion scattering
S-Ni_1	2.31(3)	2.32
S-Ni_2	2.18(2)	2.18
$d_\perp$	0.82(7)	0.87(3)
d_{12}	1.36(7)	1.31(4)
Δ%	+9(6)%	+6(3)%

Tabel III. Structural parameters (in Å) obtained by comparison to multiple-scattering calculations for the four experimental geometries dicussed in the text. S-Ni_2, $d_\perp$ and Δ% are the same parameters displayed in Table II, except as discussed in the text. The indicated errors represent the precision of the measurement and were determined from the values of $\chi^2$from the fit to theory and the curvature of the minimum for that particular parameter. The last column indicates the averages of all geometries for $d_\perp$ and the average of the [011], 38° and [001] data for S-Ni_2 and Δ%.

Parameter	[011]	38°	50°	[001]	Avg.
S-Ni_2	2.20(1)	2.19(1)	2.10(1)	2.21(1)	2.20(2)
$d_\perp$	0.85(3)	0.81(1)	0.78(2)	0.81(2)	0.81(3)
Δ%	8%	11%		12%	11(3)%

FIGURES

Fig. 1 View of the Ni(011) surface with a c(2x2) S overlayer, indicating principal crystallographic directions and the photoelectron emission directions for which ARPEFS data were collected.

Fig. 2 ARPEFS data in $\chi(k)$ form for the experimental geometries indicated in Fig. 1 and described in the text. Figs. 2(a-d) correspond to the respectively labeled directions in Fig. 1.

Fig. 3 Fourier transforms of the $\chi(k)$ data given in Fig. 2 for geometries a,b, and c. A gaussian broadened (1 Å) window function was used to reduce truncation effects. Note the change in scale for the lower two panels.

Fig. 4 This figure displays the cluster of atoms around the adsorbed S atom which provide the dominant structure in the ARPEFS data. For an explanation, see the text.

Fig. 5 Theoretical simulations of filtered data for the 50° emission data and the [011], or normal emission, data. The dotted curves are the data filtered to include only the strongest peak in the Fourier transform for each respective geometry. The solid lines are simulations employing a single-scattering theory, and the dash-dot line is the result of a calculation including double scattering.

Fig. 6 Comparison of the normal emission data to multiple-scattering calculations for several values of the S-to-2nd layer Ni distance, indicating the sensitivity of the normal emission geometry to this parameter.

Fig. 7 Comparison of the filtered normal emission and 38° ARPEFS data (dotted lines) to multiple-scattering calculations (solid lines) for the best-fit geometry determined as described in the text.

Fig. 8 Same as Fig. 7 for the [001] and 50° emission data.

Fig. 9 Values of the r-factor versus the S-to-2nd layer Ni ($S-Ni_2$) distance.

Fig. 10 Values of the r-factor versus the distance of the S atom above the first Ni plane, $d_\perp$.

Fig. 11 Comparison of the results of multiple-scattering theory to single-scattering theory for the two experimental geometries indicated.

Fig. 12 Comparison of r-factors obtained using a multiple-scattering theory to those obtained for a theory including only single-scattering for the normal emission geometry versus S-Ni_2. The single-scattering theory indicates a minimum which is shifted by 0.07Å.

Fig. 13 Values of the r-factor obtained for variation of the separation between the 2nd and 3rd Ni layers for two normal emission measurements and the 38° emission measurement.

Fig. 14 Comparison of ARPEFS data taken with an emission direction of 38° for the c(2x2) 1/2 ML surface (lower curve) to that obtained from a surface with an increased S coverage (upper curve).

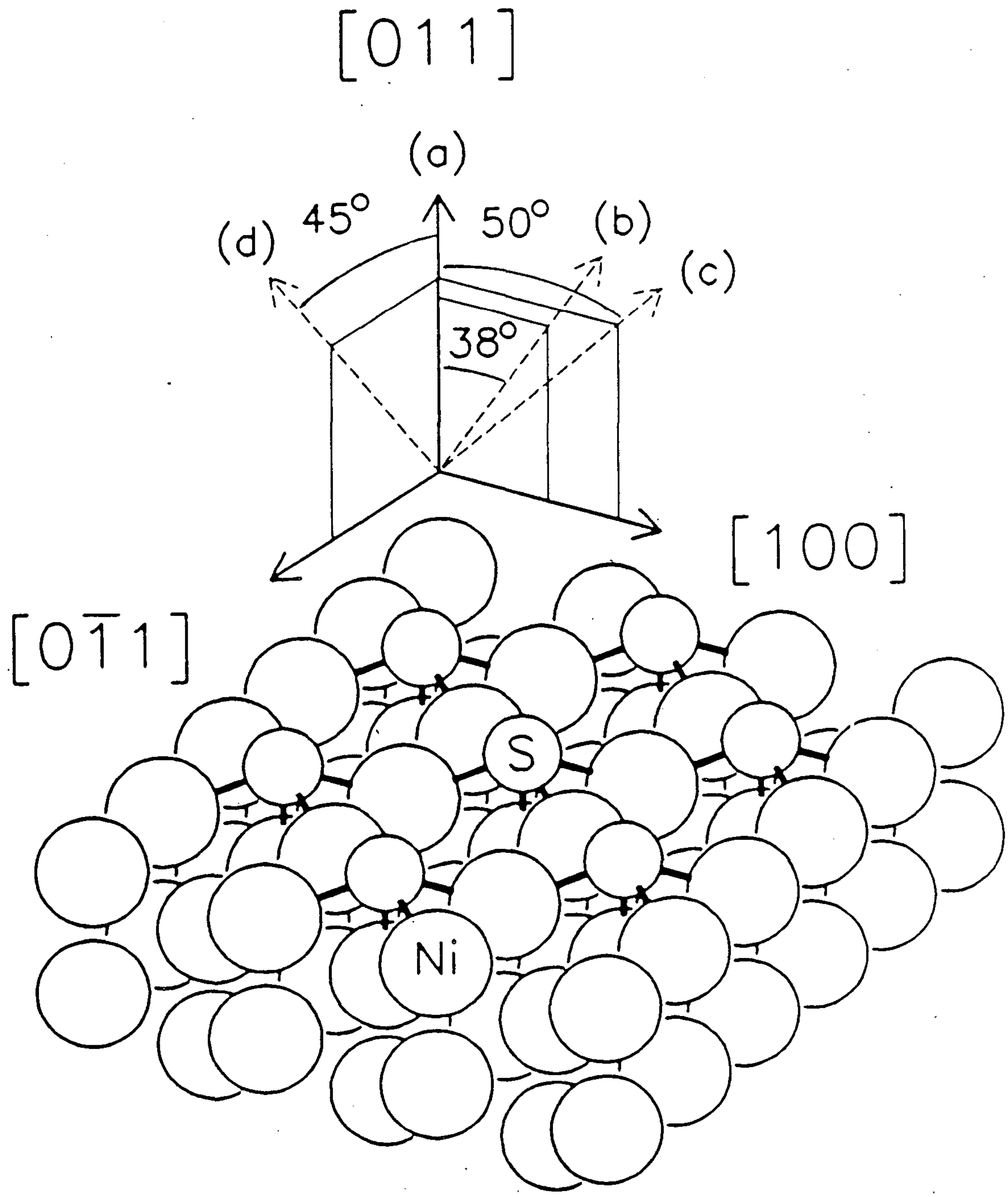

XBL 864-1286

Fig. 1

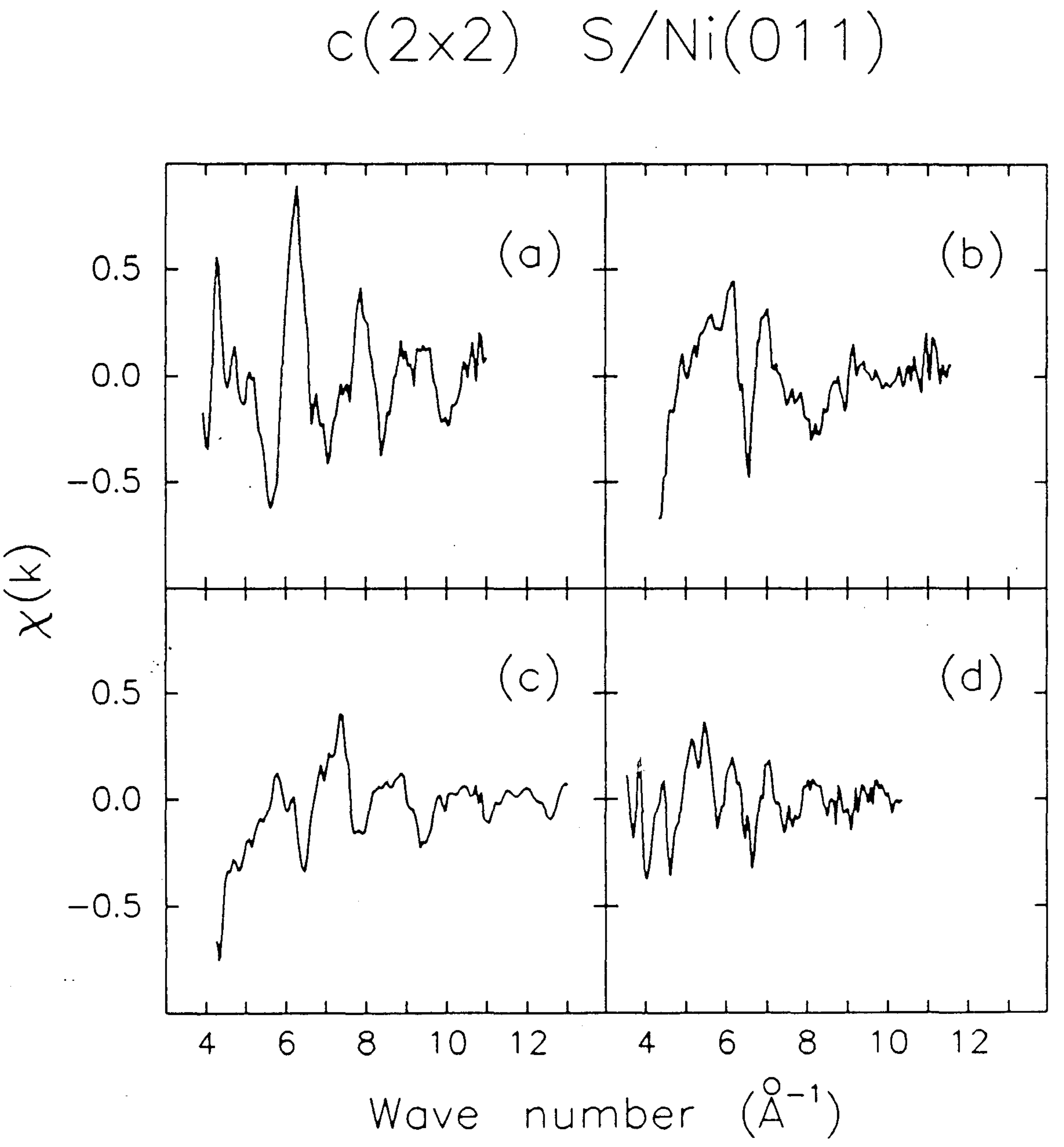

XBL 864-1551

Fig. 2

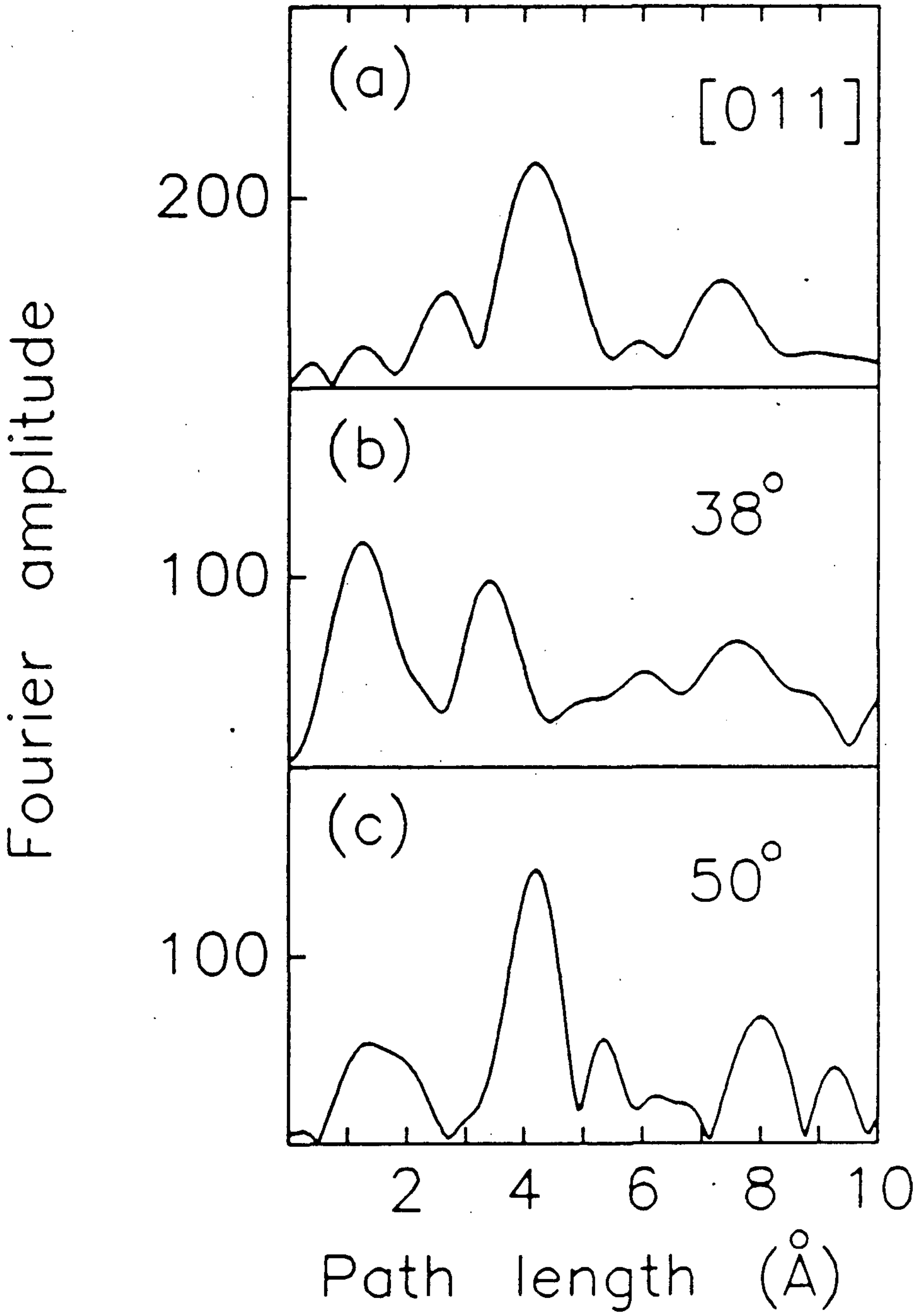

XBL 864-1273

Fig. 3

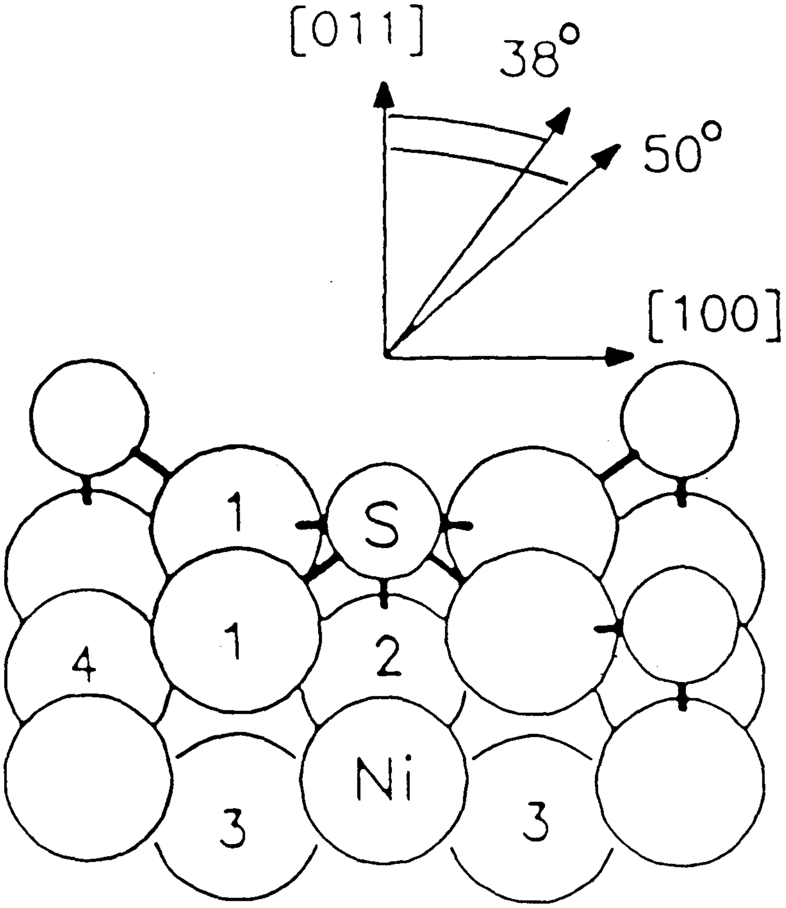

XBL 864-1288

Fig. 4

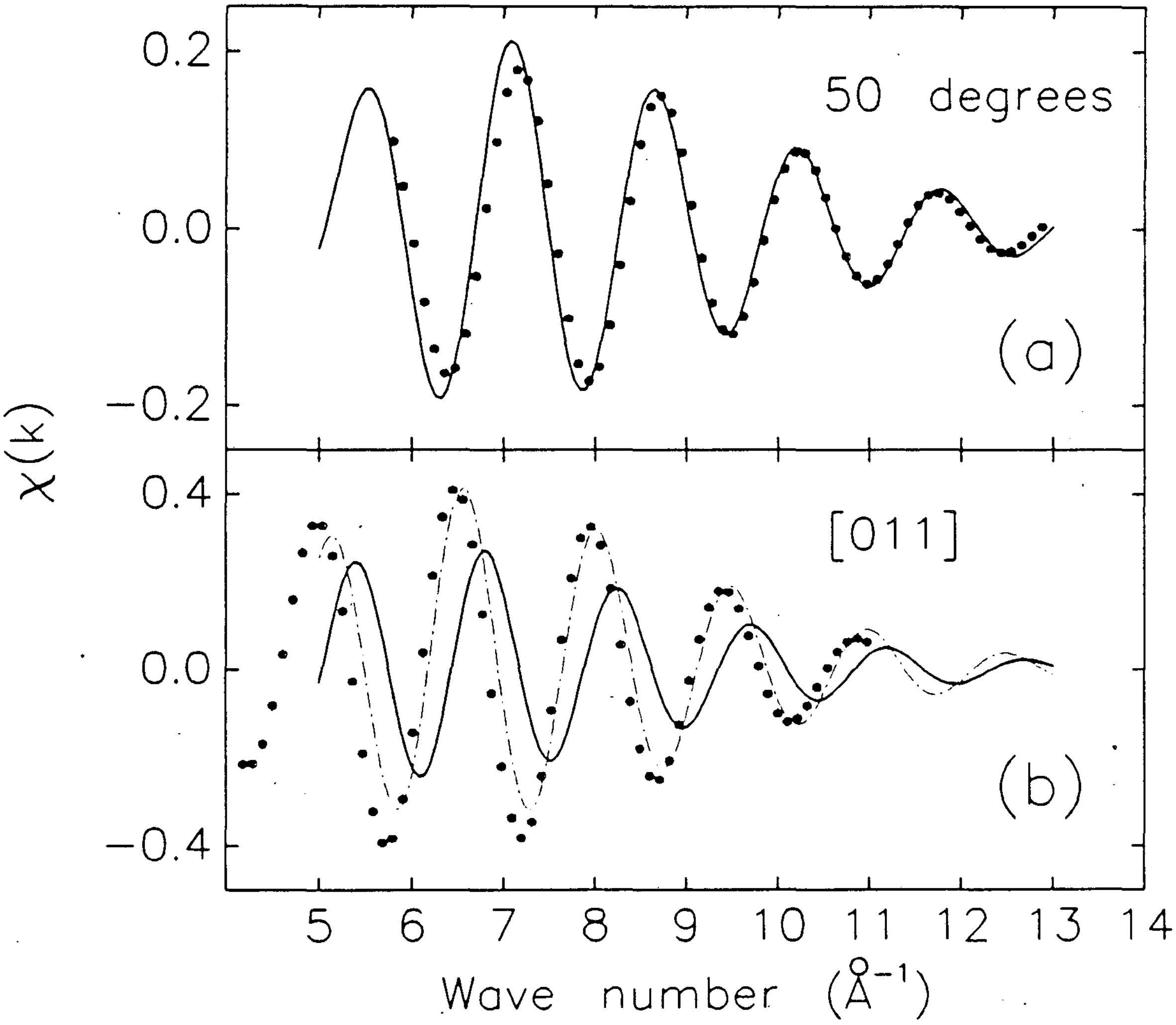

XBL 864-1559

Fig. 5

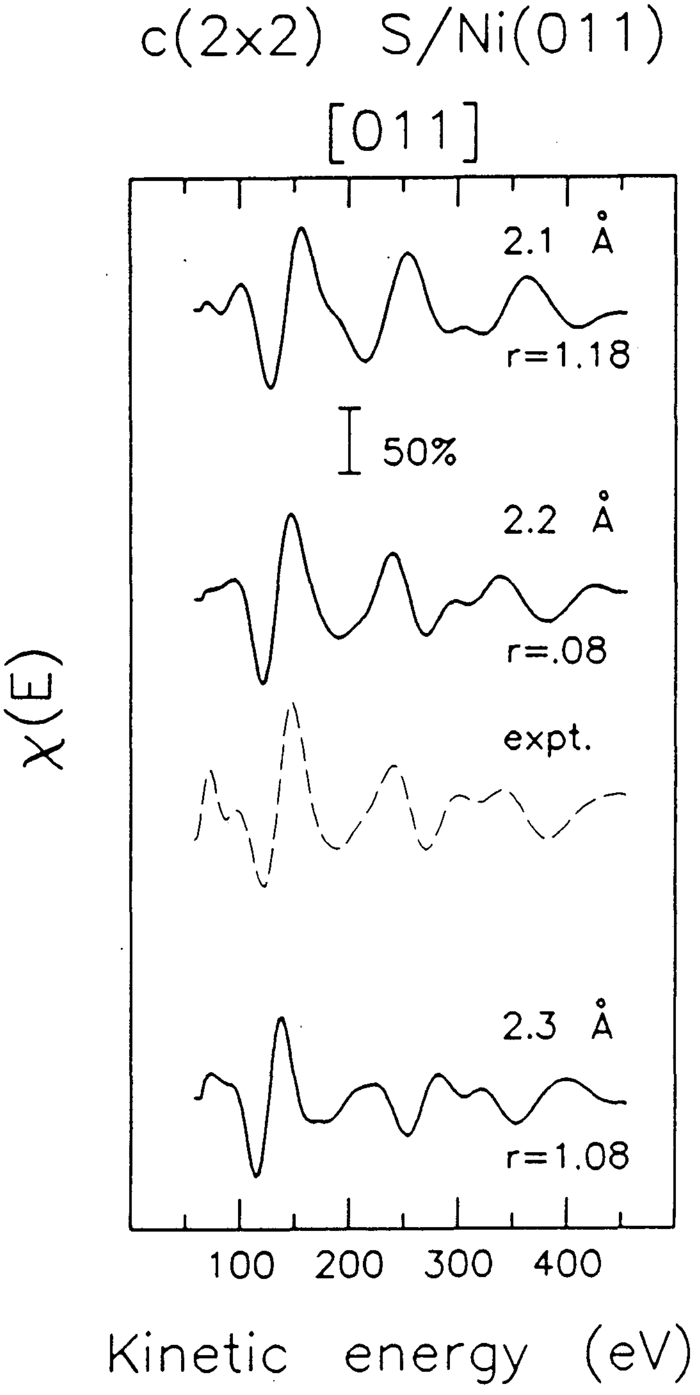

XBL 864-1290

Fig. 6

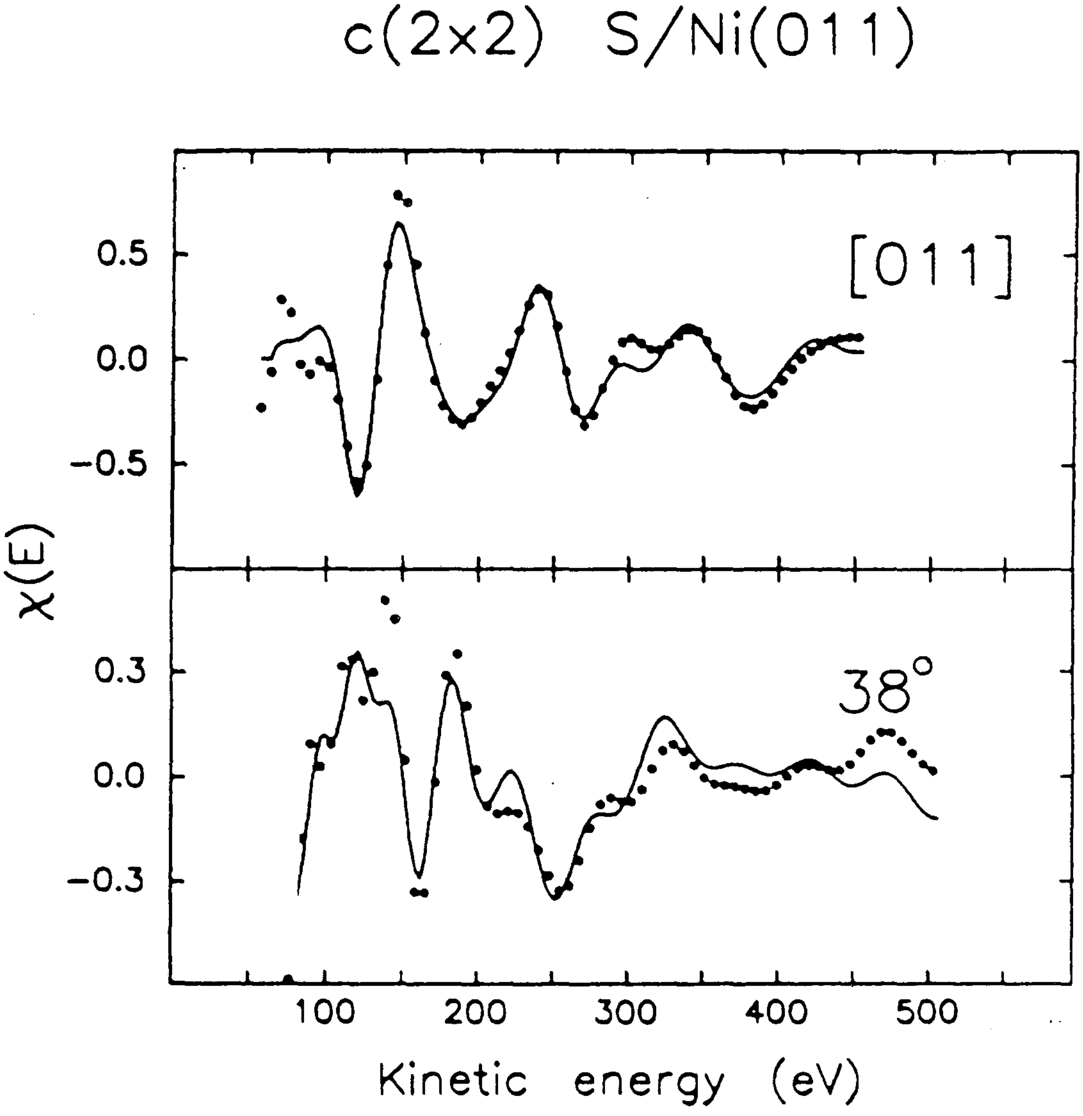

XBL 864-1291

Fig. 7

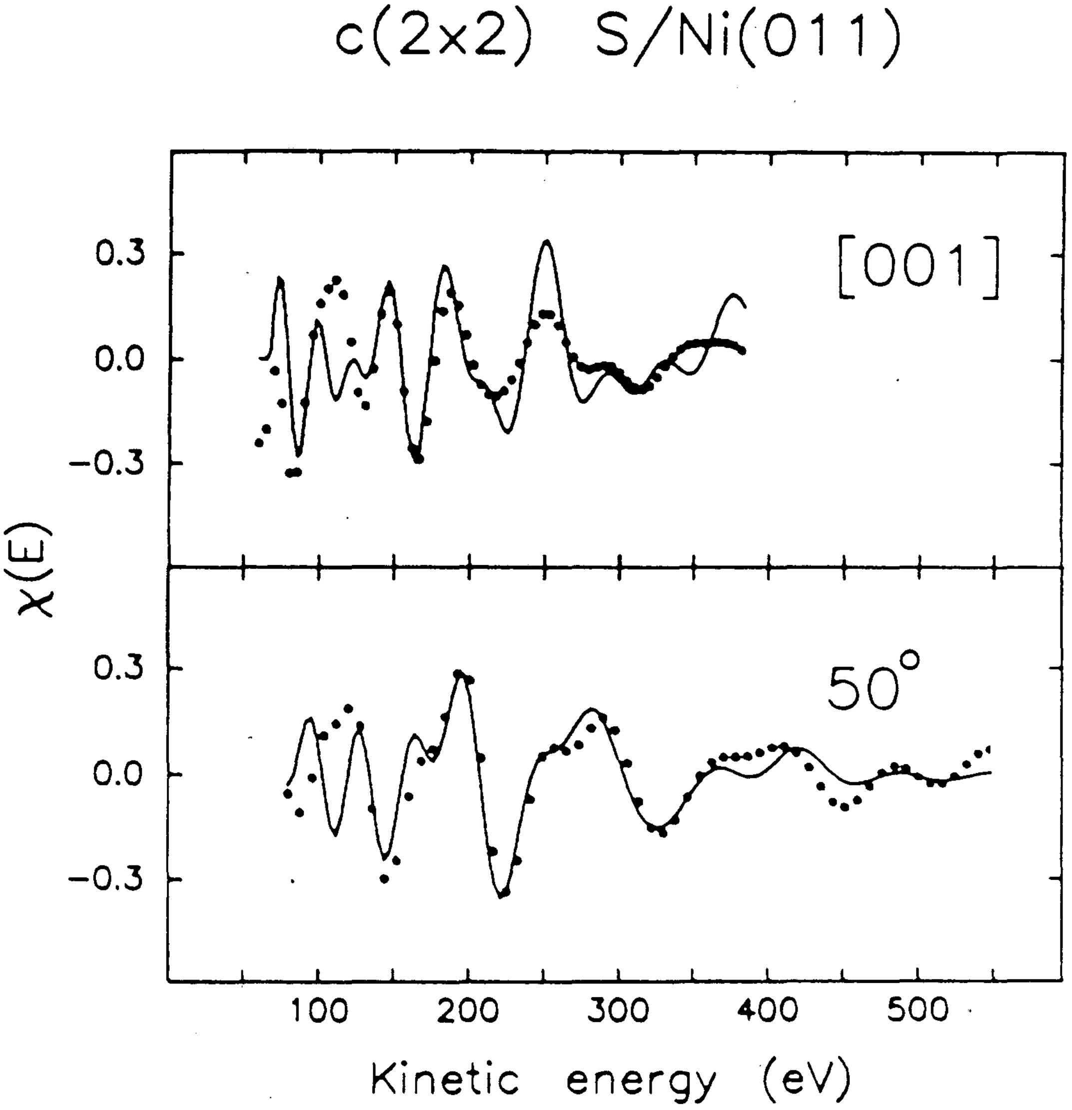

XBL 864-1292

Fig. 8

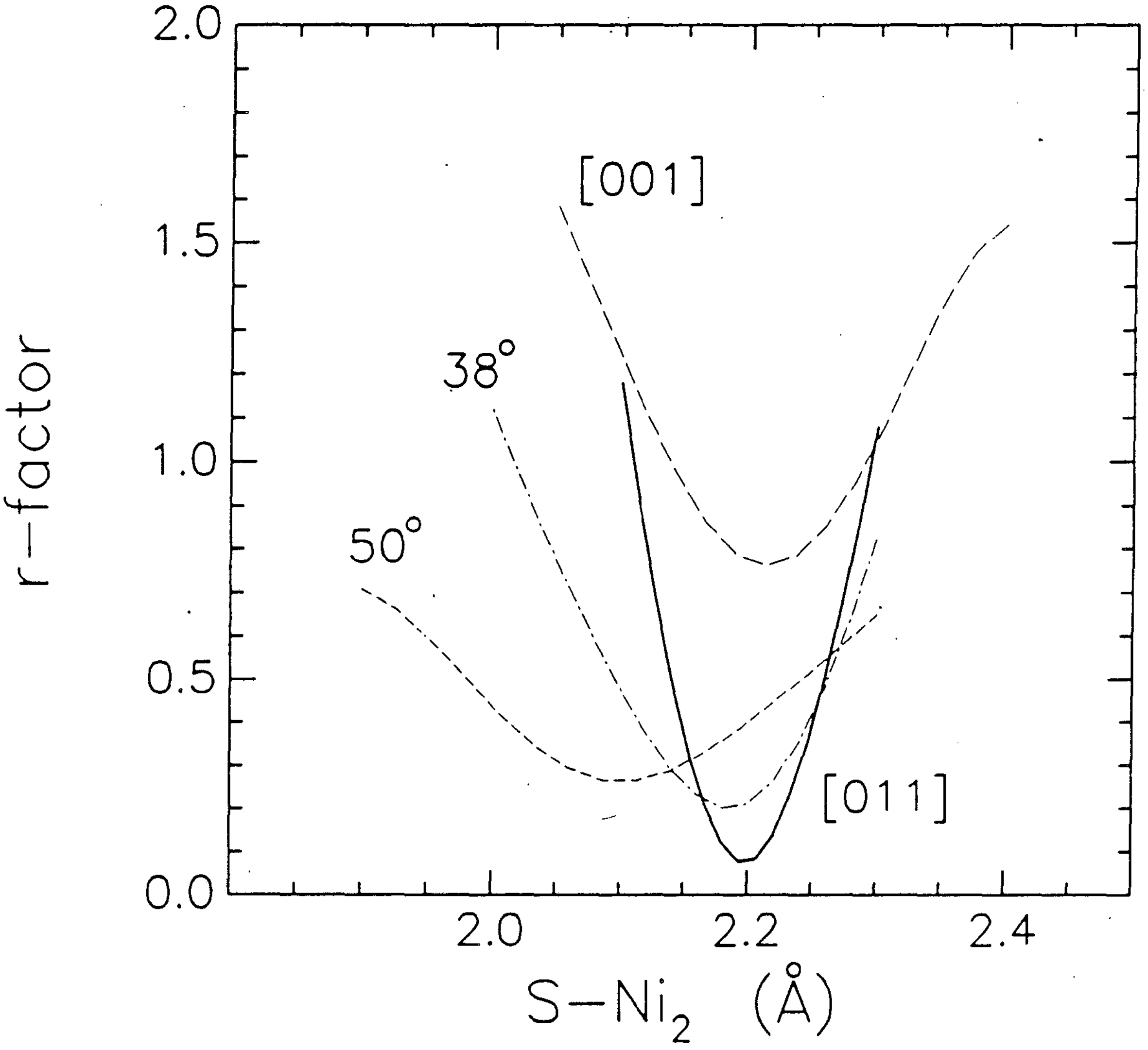

XBL 864-1293

Fig. 9

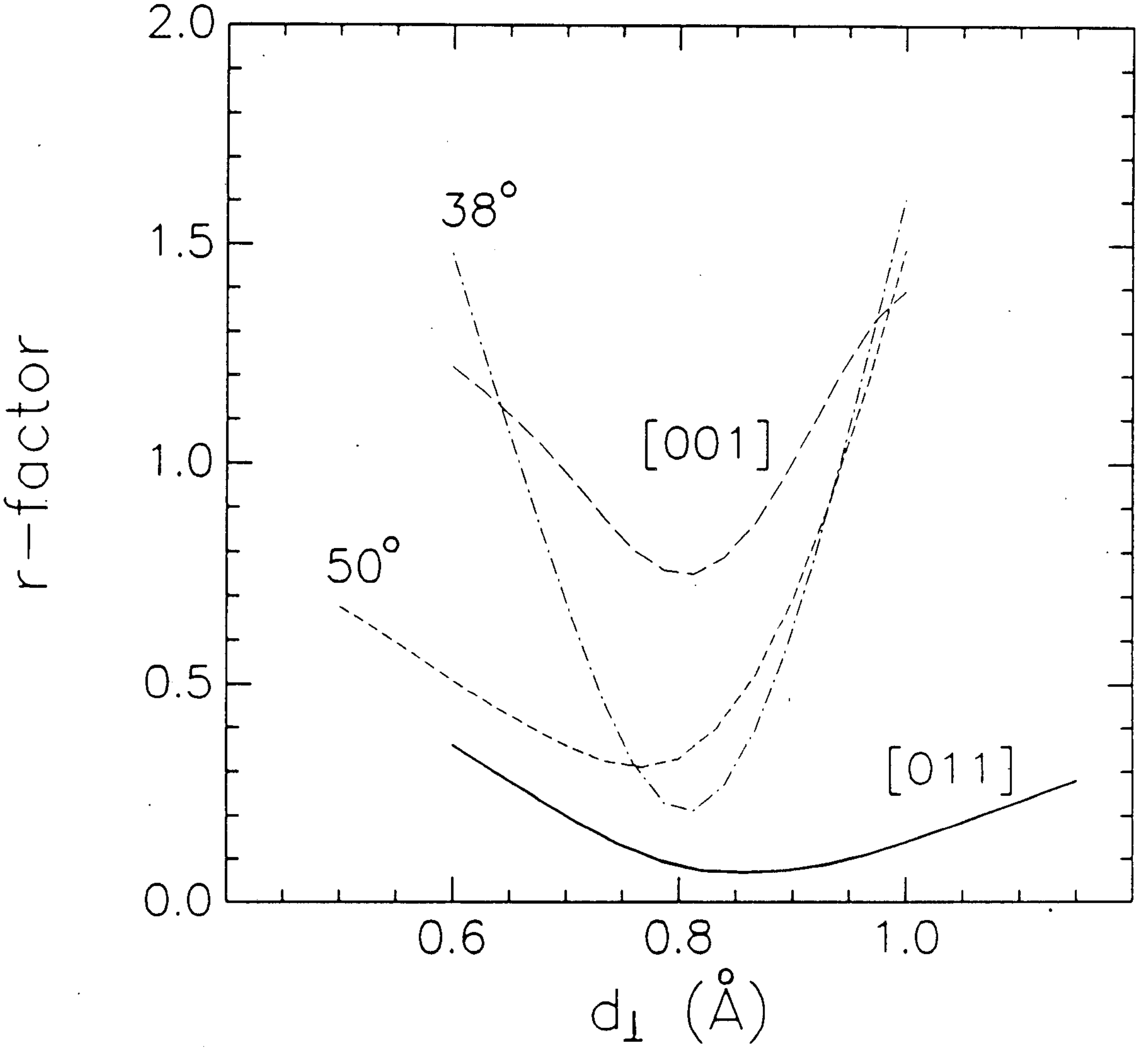

XBL 864-1294

Fig. 10

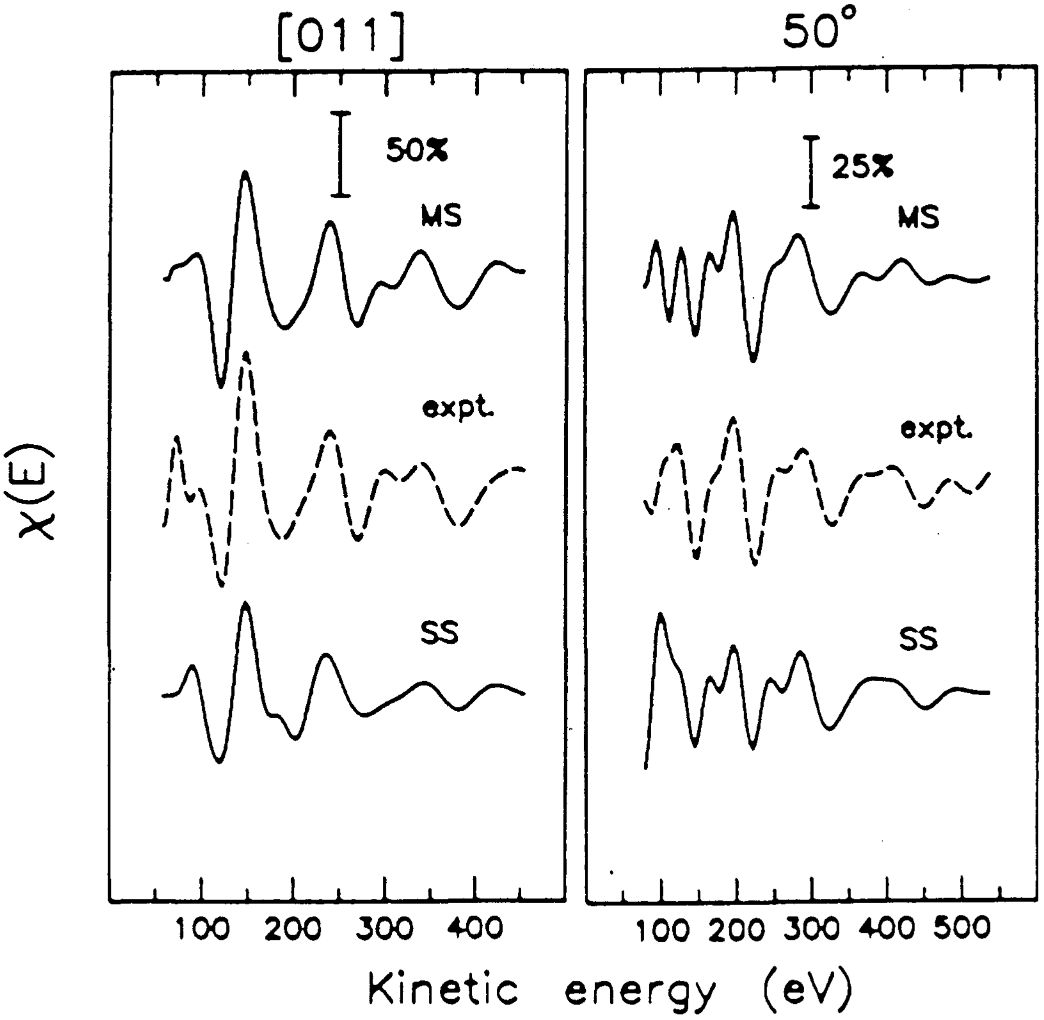

XBL 864-1295

Fig. 11

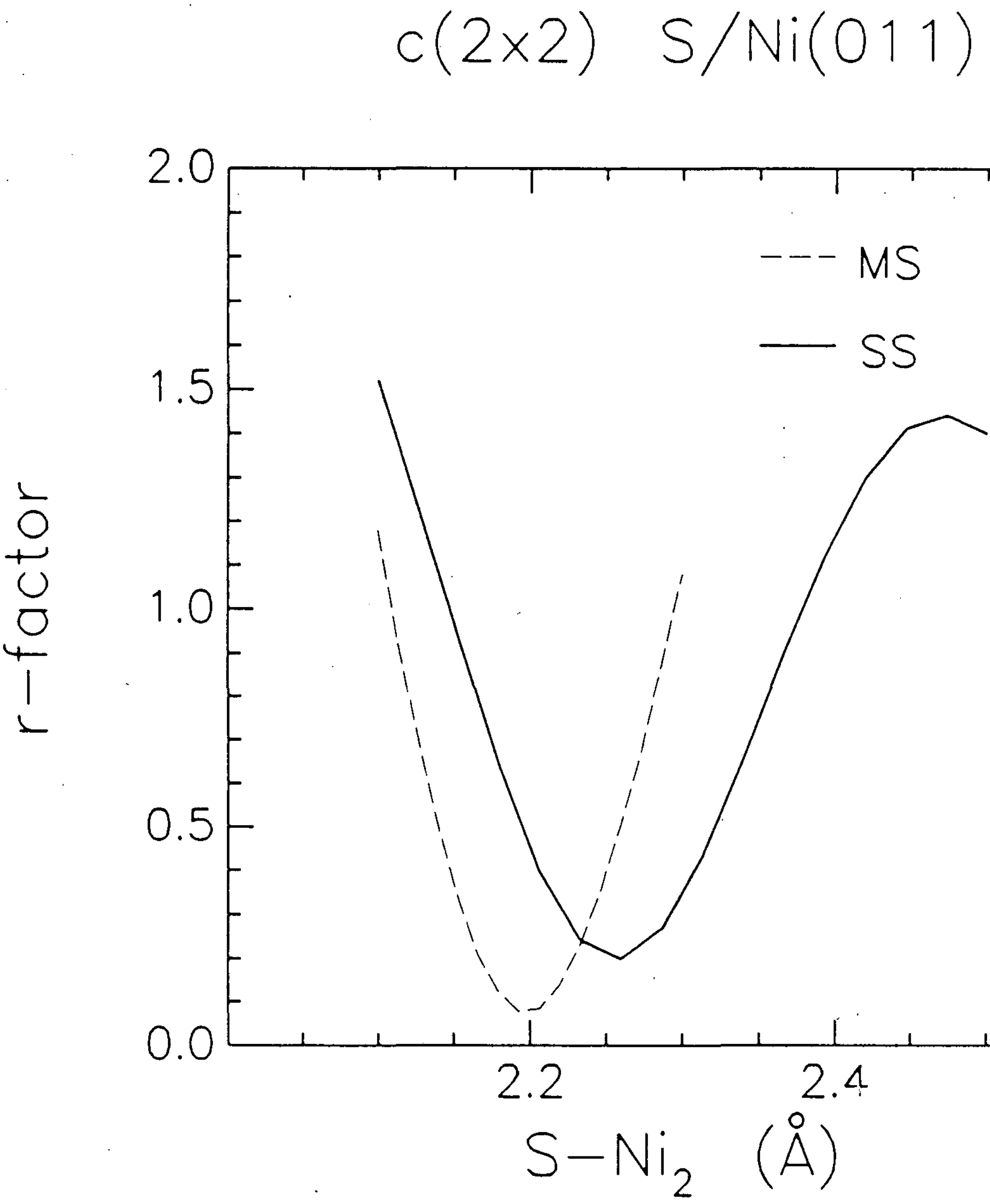

XBL 864-1296

Fig. 12

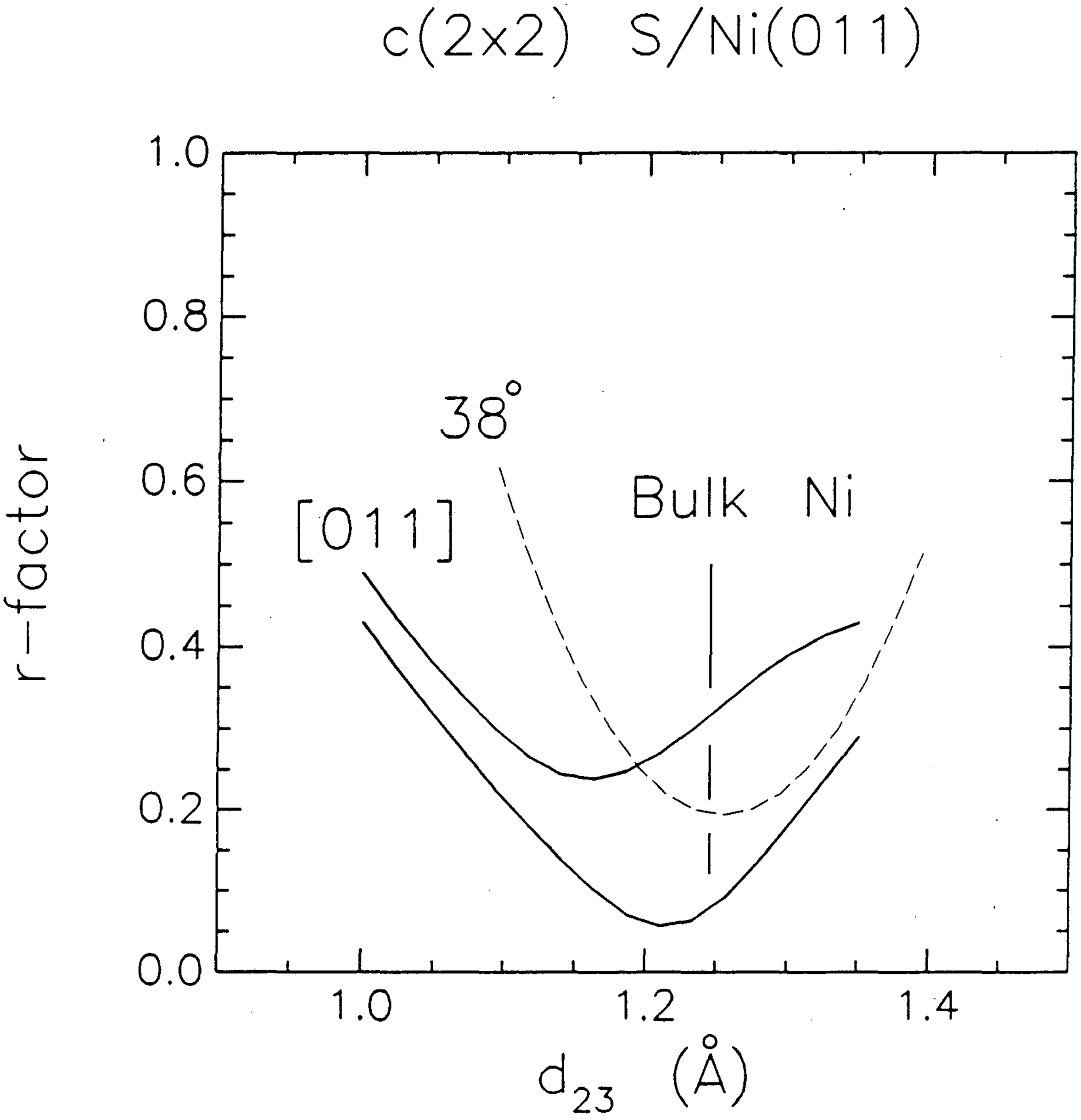

XBL 864-1297

Fig. 13

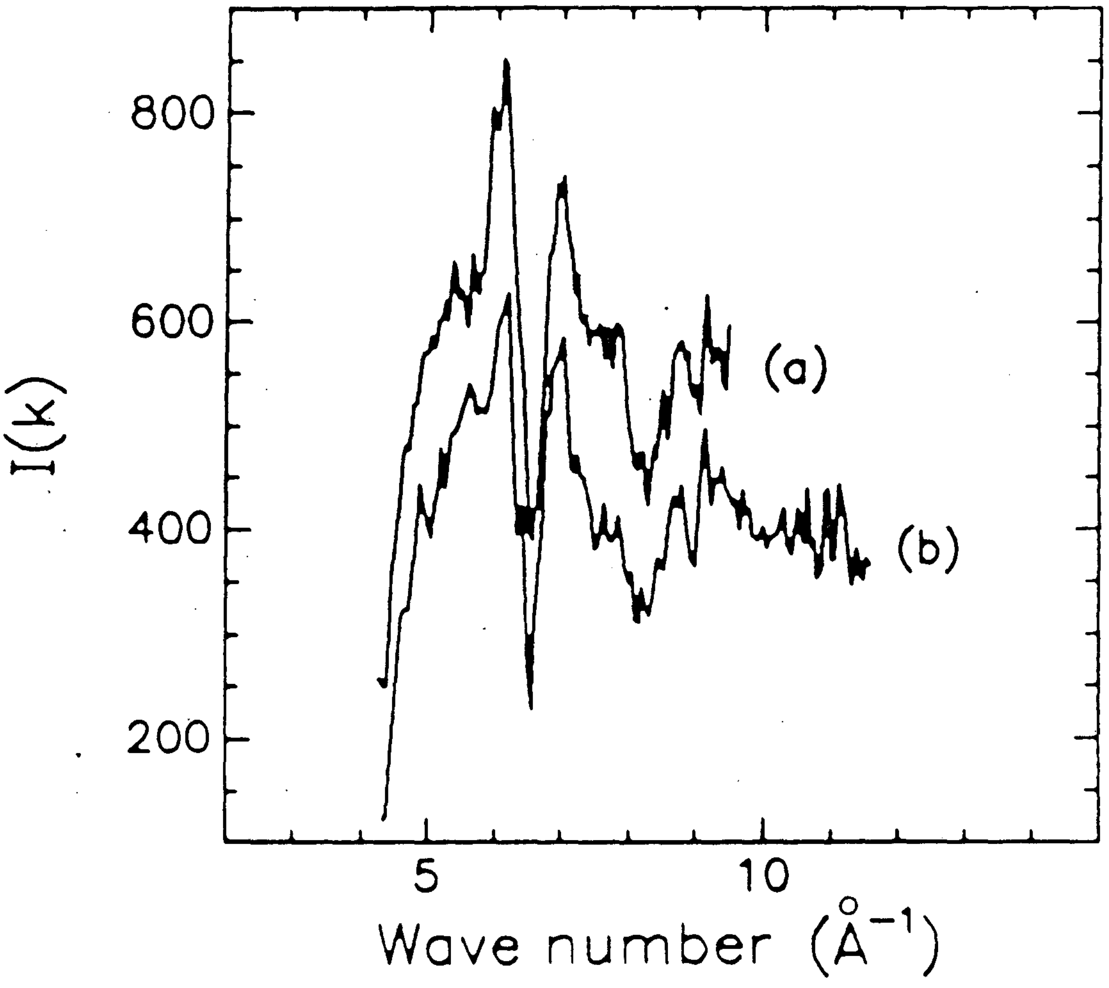

XBL 864-1298

Fig. 14

CHAPTER 5

The Surface Structure of (2x2) S/Ge(111)
Determined Using ARPEFS

ABSTRACT

Measurements of the extended fine structure in the photoemission intensity from the S(1s) core level were performed for a (2x2) overlayer of S on Ge(111). This is the first application of ARPEFS to a adsorption on a semiconductor substrate. The adsorption site and local geometry were determined from the ARPEFS using comparisons to multiple-scattering calculations. The results of this analysis indicate adsorption in a 2-fold bridge site 1.03 ±0.05 Å above the Ge surface. The separation between the first and second Ge layers is contracted by 9 ±6 %, and some Ge-Ge bond lengths between the Ge bilayers are expanded by 8 ±3 %. This adsorption site is different from that determined for another chalcogenide, Te, on the Ge(111) surface on the basis of SEXAFS measurements, but it is the same as those found for Te/Si(111) and Se/Si(111).

5.1 Introduction

Techniques such as low energy electron diffraction (LEED)[1], ion scattering[2], surface-extended x-ray absorption fine structure (SEXAFS)[3], and, more recently, angle-resolved photoemission extended fine structure (ARPEFS)[4] have been employed with great success to obtain surface structural information. The majority of studies have invloved chemisorption of simple atomic and molecular species on metallic substrates. Fewer studies have been performed on semiconductor surfaces. However, the qualitatively different nature of semiconductor surfaces compared to metallic surfaces, arising from the strong directional bonding, offers interesting opportunities for surface structural studies on these surfaces. In the simplest approximation, one might expect that saturation of "dangling bonds" present on semiconductor surfaces would be the dominant effect, leading, for instance, to atop sites for monovalent adsorbates, two-fold sites for divalent atoms, etc. Of course, this simple picture is complicated by the presence of the clean surface reconstructions and dependences on typical bond lengths of the adsorbate compared to the separation of the dangling bonds on the surface. For example, consider the important case of oxygen adsorption on Si. The most widely accepted model for the stable chemisorption configuration involves bridge bonding as might be expected. However, because of the shortness of Si-O bonds (1.6-1.7 A), the oxygen atom is postulated to insert into a bond between a surface layer Si atom and a Si atom in the second layer.[5] Evidence has also been presented indicating that the initial adsorption of O_2 occurs via the formation of peroxy bridges between surface Si atoms.[6]

These considerations suggest a systematic study of adsorbates with differing valencies on semiconductor surfaces. The aim would be to develop ideas concerning the relative importance of the various factors influencing bonding at these surfaces. Experiments designed to elucidate this questions were recently presented by Citrin et al.[3b] These authors performed SEXAFS measurements for monovalent and divalent atoms (I and Te) adsorbed on Si(111) and Ge(111) surfaces. Previous work was also performed for the adsorption of Cl on these surfaces.[3c] There have also been several studies employing x-ray standing wave fluoresence methods to determine adsorption sites for Br adsorbed on Si(111)[7-9] and Ge(111)[10] and also Se on Si(111)[11].

The results of these studies indicated that for most of the systems, a simple idea of chemisorption with unity bond order provides a reasonable explanation of the adsorption behavior. Thus, Cl and I adsorbed by saturating a single dangling bond in an atop configuration. Divalent atoms (Te/Si studied by SEXAFS and Se/Si studied using x-ray flouresence) were found to adsorb in 2-fold bridge sites with the accompanying saturation of two dangling bonds. An exception was found in the case of Te adsorbed on Ge(111). For this system, the SEXAFS study indicated adsorption in a different site-- a 3-fold surface site with a Ge atom in the 2nd layer (or 2nd component of the first Ge bilayer) directly below. X-ray standing wave studies of Br/Si(111) have also indicated deviations from a local bonding model of chemisorption, with some indications of Br adsorption in 3-fold sites above fourth layer Ge atoms. However, this result has been reported to depend on the method of sample preparation, possibly due to co-adsorption of contaminants.[9]

Considering the interesting deviation exhibited by the Te/Ge(111) system, we have examined the surface structure of another divalent atom, S, on Ge(111). The adsorption of S on Ge (111) exhibits characteristics which are very similar to those found by Citrin et al. for the Te/Ge(111) system, in terms of the saturation coverage (~1/2 ML) and the stable (2x2) LEED pattern obtained. This study should thus not only provide surface structural information on a previously unstudied system, but also serve as an interesting comparison with the behavior found for Te/Ge(111). This work also provides the first application of ARPEFS to adsorption on a semiconductor substrate.

Surface structural information was obtained from the S/Ge system by performing measurements of ARPEFS.[4] This technique involves measurements of the intensity of the angle-resolved photoemission (ARP) from a core level of the adsorbate as a function of the photoelectron kinetic energy. Surface structural information is contained in ARP due to final state interference caused by scattering of the photoelectron from neighboring atoms. Recent studies of adsorption on clean metal surfaces[13] have indicated that excellent surface structural results can be obtained from ARPEFS using an analysis based on a combination of comparisons to theoretical calculations and Fourier transform techniques.

The major conclusions which can be drawn from these previous experimental[4,13] and theoretical[14,15] investigations are that, due to the peaking of the magnitude of the scattering amplitude in the forward-scattering and back-scattering directions, the finite electron mean-free path, thermal correlation effects, and the overall 1/r dependence of the ARPEFS, scattering events involving near neighbors and near-backscattering will produce strong ARPEFS modulations. Also, specific atoms can be enhanced relative to others by proper choice of the photon polarization direction. These ideas suggest the possibility that adsorption sites can be efficiently tested by choosing experimental geometries which will emphasize backscattering from near neighbors in those sites. The presence or abscence of the expected strong backscattering structure will provide a distinct indication of the possibility of adsorption in that site. Experimental geometries chosen with these ideas in mind may also allow the use of Fourier transform techniques to determine bond lengths precisely.

Since it has also been shown that multiple scattering effects cannot be neglected in ARPEFS[15,16], it is important to consider the implications of this for an ARPEFS experiment. Because of the strong forward peaking of the scattering amplitude ,the dominant multiple-scattering events will be those which include forward scattering. Since additional near-forward scatterings will introduce practically no extra path length difference, the inclusion of multiple scattering will serve primarily to enhance the amplitude of a single scattering event when that event is proceeded or followed by forward scattering. The additional forward scatterings act to focus the electron amplitude along the forward direction. Since backscattering events in an ARPEFS experiment will always be followed by a subsequent forward scattering through the emitting atom, the inclusion of multiple scattering will serve to enhance backscattering events even more strongly than is predicted by a single scattering theory. Thus, the qualitative aspects of performing an experiment to determine an adsorption site are unaffected by this dominant multiple-scattering effect.

In general, however, it is also necessary to perform comparisons to multiple-scattering calculations to extract detailed information about the adsorption geometry, and these calculations must account quantitatively for multiple-scattering effects. In addition to modifications of the scattering amplitude due to multiple scattering, there will also be contributions to the scattering phase shift for each additional forward scattering. The calculations which were performed for comparison to the data for S/Ge(111) included these multiple-scattering effects. These calculations will be described in more detail in Section 5.3.

The remainder of this chapter is organized as follows. Section 5.2 describes experimental details and presents the $\chi(k)$ curves for the (2x2) S/Ge(111) system collected for the two experimental geometries employed in this study. Section 5.3 then provides a discussion of the

ARPEFS and a quantative analysis employing comparsions to multiple-scattering calculations. A summary and conclusions are given in Section 5.4

5.2 Experimental details

In this section, we present a description of the experimental details of this measurement of ARPEFS for (2x2) S/Ge(111). This includes a discussion of the sample preparation procedures, followed by a description of the geometries employed for this experiment. We include a brief discussion of an important aspect of the data reduction, and conclude with the presentation of the $\chi(k)$ curves.

5.2.1 Sample preparation

A single crystal of Ge was cut (7x8x1mm) and mechanically polished to an orientation of ≦ 1° from a (111) plane. The orientation was determined by Laue backscattering after etching in a solution of 100 ml Mirrolux (Cabot Corp., Tuscola, Il.) and 25 ml 30 % H_2O_2. The crystal was mounted on a high precision sample manipulator for insertion in the experimental chamber, which maintained a typical pressure of 2×10^{-10} Torr. The manipulator allowed linear motion along three perpendicular axes and rotations about both an axis in the crystal surface and about the crystal normal.

The clean Ge(111) (2x8) LEED pattern was obtained by Ar^+ sputtering at an energy of 500 eV and annealing to 650° C. The sample was heated by electron bombardment from a W filament located behind the Ta sample plate on which the crystal was mounted. Temperatures were measured using a Chromel-Alumel thermocouple attached to the sample plate next to the Ge crystal. The (2x8) LEED pattern formed using this procedure displayed sharp 1/8 order spots, and Auger electron measurements performed employing the LEED optics in the retarding-field mode indicated no sign of impurities.

Sulfur overlayers were formed by exposure of the clean surface to H_2S. In order to achieve a saturation coverage of S it was necessary to perform several cycles of exposure to H_2S followed by annealing to 300-350°C. This behavior is presumably due to at least partial dissociation of the H_2S on this surface, leading to the necessity of desorbing excess hydrogen at 325°C[18] to allow for the adsorption of additional sulfur. Thus, although the total exposure varied from sample to sample, the saturation coverage indicated by the ratio of the S(152 eV) Auger intensity to the Ge(89 eV) Auger intensity was well reproduced. This saturation coverage was found to correspond to about 1/2 ML as estimated by the Auger measurements and photoemission intensity measurements performed using the S(1s) and Ge(2s) core levels, in agreement with the saturation coverage obtained for Te/Ge(111) by Citrin et al.

Similar adsorption behavior was also observed in previous studies of the absorption of S and Se on crushed Ge powders by Boonstra and Van Ruler.[17] Those authors were able to initially adsorb the equivalent of 1/4 monolayer on the clean Ge powders (~ 70 % (111) plane). They then heated to between 200°C and 400°C and observed the desorption of hydrogen. Additonal exposures to H_2S then lead to the adsorption of a total of 1/2 ML.

A final anneal to 350°C after achieving a coverage of 1/2 ML resulted in the formation of a sharp (2x2) LEED pattern. This, too, is in agreement with LEED patterns obtained previously for S and Se adsorption on Ge(111)[19] and the Te/Ge(111) SEXAFS study. These similarities would seem to indicate common adsorption characteristics for the divalent atoms, S, Se, and Te, on the Ge(111) surface. Once formed, the S overlayers showed no degradation in terms of adsorption of contaminants over many hours.

5.2.2 ARPEFS geometries

ARPEFS measurements were performed for two experimental geometries. The emission and photon polarization angles for each geometry were determined as described in Chapter 3. These angles have an estimated accuracy of ±2°.

For the first geometry, photoelectrons emitted along the surface normal were collected, with the photon polarization directed 30° from the normal towards a [100] direction. The second ARPEFS geometry involved electron emission 60° from the surface normal towards the [100] direction, 54.7° from the normal. The polarization was aligned along the emission direction.

5.2.3 Data collection and reduction

For each geometry, a series of photoelectron spectra were collected in increments of 0.1 $Å^{-1}$. This scan was performed using an energy window of 20 eV which included the S(1s) core level. The subsequent treatment of these data has been described in detail previously.[20] Briefly, it consists of extraction of the intensity in the S(1s) core peak for each kinetic energy and normalization of this intensity for photon flux to form I(E), the total intensity as a function of the photoelectron kinetic energy, E. The total measured intensity can be written

$$I(E) = (\chi(E)+1)\ I_0(E). \tag{1}$$

The function $\chi(E)$ is the oscillatory contribution to the total intensity which contains the structural information and $I_0(E)$ is a slowly varying function. As in EXAFS[21], $I_0(E)$ can be determined by fitting with a smooth cubic spline and removed to give,

$$\chi(E) = I(E)\ /I_0(E)\ -1. \tag{2}$$

This procedure, however, deserves additional comment for ARPEFS experiments, and in particular for the data collected for this system.

The normal emission ARPEFS for the (2x2) S overlayers contained a significant amount of structure indicating possible scattering with path lengths of ~ 2 Å. In the case of an EXAFS measurement, this structure would correspond to non-physical bond lengths of <1 Å, and would be due to low frequency errors in the measurement. However, for an ARPEFS experiment, the presence of this structure in the normal emission data could also be indicative of a sub-surface adsorption site. Several tests were performed to determine if this low frequency structure was indeed due to ARPEFS. First, normal emission experiments performed on two (2x2) S/Ge(111) samples both indicated low frequency structure with reasonable agreement in terms of the amplitude and frequency, but with a significant relative phase shift in the low frequency oscillation. Thus, adding the two data sets led to a large reduction in the amplitude of the low frequency structure. Also, this structure was found to be sensitive to the background removal procedure. Finally, theoretical investigations of several models for sub-surface adsorption, including sub-surface substitutional and interstitial sites, while reproducing the structure adequately with respect to the expected frequency, did not explain the relative phase shift between the two data sets. This discrepancy could not be explained even considering possible angular differences of as much as 5-10° between the two measurements, well beyond the accuracy in determining these angles. These models also produced worse agreement overall in the reproduction of the experiment than that obtained for adsorption in a surface 2-fold site, to be discussed below. Thus, the most likely cause of the low frequency structure in these data are errors introduced in the data collection and reduction procedures due, for instance, to photon beam movement on the sample induced by monochromator crystal heating and cooling.

Having established that the low frequency oscillations do not contain ARPEFS, structure with frequencies below 2 Å in the ARPEFS for both geometries was removed either by Fourier filtering or by fitting with a smooth cubic spline as indicated above. The off-normal geometry is expected to have real ARPEFS structure in this low frequency range, even for an adsorption site above the surface. However, due to the experimental difficulties in measuring ARPEFS in this range, filtering was also performed for those data. In comparisons to theoretical calculations care was then taken to filter the calculations in the same manner.

Examination of the data using Fourier transforms requires the conversion of $\chi(E)$ to $\chi(k)$. The photoelectron kinetic energy, E, measured outside the solid is related to the wavenumber, k, of the photoelectron inside the solid by

$$k = 1/h\,[2m_e(E+V_0)]^{1/2}, \qquad (3)$$

where m_e is the electron mass and V_0 is the inner potential of the solid. The value of the inner potential is typically about 10 eV, but the exact value is unknown and is slightly energy dependent for ARPEFS energies. Because we are primarily interested in the qualitative features of the Fourier transforms to be presented later, this conversion was accomplished using a value of V_0= 10 eV.

ARPEFS $\chi(k)$ curves for the two experimental geometries described above are presented in Figs. 1 and 2. The error bars indicate the statistical uncertainty in the data. The dip in the off-normal curve at ~ k = 6 (~ 150 eV) occurs in a region where the S (1s) photopeak is coincident in energy with the S Auger peak. However, this affects the data significantly for only 3 experimental points and careful fitting in this region can minimize the effect. The structure in the $\chi(k)$ curve in this region is thus not due to this coincidence.

5.3 Data analysis

Excellent results have been obtained in the past using comparisons to multiple-scattering calculations to extract structural information from ARPEFS. The results of this study are also depend on comparisons to theory to conclusively identify the adsorption geometry. It has also been shown, however, that information can be obtained by qualitative examination of $\chi(k)$ curves and Fourier transforms, due to the relatively simple nature of the scattering processes involved. Thus, before considering the results of detailed comparisons to theory, we will first present a discussion of the qualitative features of the data that are apparent from examinations of the $\chi(k)$ curves in Figs. 1 and 2, and the Fourier transforms exhibited in Fig. 3.

5.3.1 Qualitative discussion

Several possible S adsorption sites were considered. As indicated previously, several models for sub-surface incorporation were considered, primarily to help ascertain whether the low frequency structure in the normal emission data could be due to low path length near-forward scattering events. These models were found to be inadequate and will not be discussed further. The most extensive consideration was given to the various high symmetry sites that are present on the Ge(111) surface. These sites are illustrated in Fig. 4. This figure presents two views of the (111) surface-- Fig. 4(a) presents a view looking down along the [111] direction and Fig. 4(b) presents another perspective with the surface normal rotated 40° away from the reader. The four sites indicated in this figure are atop, 3-fold hollow (a 3-fold surface site directly above a fourth layer Ge atom), 3-fold eclipsed (a 3-fold surface site directly above a second layer Ge atom), and the 2-fold bridge site. The following discussions will concentrate on these four sites.

Before beginning a consideration of the ARPEFS, it is useful to consider the characteristics of the Ge-S bonding which might be expected for these sites, in view of the information available on bulk compounds containing Ge-S bonds. A survey of these compounds reveals a range of bondlengths of from 2.05 -2.44 Å, with a strong bias towards bonds of 2.15 -2.20 Å. In particular, germanium monosulfide is a layered compound with an orthorombic structure.[22] Each S atom is bonded to 3 Ge near-neighobors with bond lengths of 2.44 Å and nearly tetrahedral bond angles. There are additional Ge-S bonds of ~ 3.3 Å. Germanium disulfide has a monoclinic space group[23] with tetrahedral units consisting of Ge atoms surrounded by 4 S atoms, with the S atoms forming bridges between adjacent Ge atoms. The Ge-S bond varies from 2.17 Å to 2.29 Å and the Ge-S-Ge bond angle takes values of 98°-102°.

This information should be useful in considering likely bonding arrangements for a given site. For instance, adsorption in an atop site would probably involve a Ge-S bond in the range given above. In view of the structure of GeS, a reasonable possibility for adsorption in a 3-fold hollow site would involve bond lengths close to 2.44 Å and nearly tetrahedral bond angles to the 3 first layer Ge atoms. This would require a value of about 0.8 Å for the height of the S atom above the Ge surface.

For the 3-fold eclipsed site a similar arrangement might seem likely. However, for an unreconstructed site and reasonable (< 2.5 Å) Ge-S bond lengths, the S atom is too close to the 2nd layer Ge. Based on the information given above for bulk Ge-S compounds, we would expect that the S atom would be at least 2 Å above the 2nd layer so that if significant bonding to the first layer occurs, it would be accompanied by moderately large reconstruction involving of the Ge atoms in the first and/or 2nd layers.

The 2-fold bridge site has an analog in the GeS_2 structure, as well as the majority of other Ge-S compounds, most of which involve S atoms bridging between two Ge atoms. With this analogy in mind and assuming an unreconstructed Ge(111) surface and Ge-S bonds of 2.2 Å, one is lead to postulate a value of around 1 Å for the height of the S atom above the Ge surface.

With these rather general ideas of possible adsorption structures in mind, we now turn to a qualitative examination of the ARPEFS data.

The important aspects of the ARPEFS that are evident from Figs. 1, 2, and 3 are as follows:

(1) The normal emission data are dominated by a single peak in the Fourier transform with a path length (or path lengths) of ~ 3.5-4 Å and with an oscillation amplitude of ~ 20-25 %.

(2) The off-normal data exhibit no very strong structure (nothing above 5-10 %) and show no dominant peaks in the Fourier transform.

The structure in the normal emission data is inconsistent with adsorption in a 3-fold hollow site. For this site, one would expect two peaks in the Fourier transform, or at least broad structure with two centroids in the 3-5 Å range, due to scattering of approximately the same amplitude from 3 Ge near-neighbors in the first layer and a similar set of 3 atoms in the 2nd layer. The path lengths for these two sets of atoms would be ~ 3 Å and ~ 4.4 Å for the GeS-type bonding arrangement described previously. This magnitude of path length separation should be clearly resolvable for the data range measured. Variations of the height of the sulfur atom above the Ge surface and moderate reconstructions of the Ge atom positions, while maintaining reasonable Ge-S bond lengths, would not significantly affect this aspect of the expected Fourier transform structure.

An explanation of the normal emission ARPEFS in terms of adsorption in an atop site is also difficult. Although the Fourier transform peak at 4 Å could be due to a bond to a first layer Ge atom within the range discussed above, the amplitude of the $\chi(k)$ oscillation is much smaller than would be expected for a direct backscattering geometry. For atop adsorption, the ARPEFS would be strongly dominated by backscattering from the Ge atom below the S. Previous ARPEFS studies of S/Cu[13b], for which the Cu backscattering amplitude is similar to Ge, would lead one to expect ARPEFS oscillations of 40-50 % for near-neighbor backscattering at a bond length of about 2 Å.

The 3-fold eclipsed site would also involve near-neighbor backscattering for normal emission ARPEFS. However, in this site, there is the possibility that the structure at 4 Å in the Fourier transform may not be due solely to this backscattering. For a nominally unreconstructed site and with the sulfur atom 2.2 Å above the 2nd layer Ge atom, the 3 Ge atoms in the first layer will also have path lengths at normal emission of ~ 4 Å. Theoretical simulations (to be discussed later) indicate that this leads to destructive interference and a reduction of the strong backscattering oscillation. Thus, we now turn to consideration of the off-normal data to test this site further.

The off-normal geometry was chosen specifically to test for strong backscattering which should be apparent for adsorption in the 3-fold sites. For the chosen emission angle of 60° towards [100], there should be strong structure at ~ 5 Å due to scattering from a first layer near-neighbor Ge atom if adsorption occurred in the 3-fold eclipsed site, as postulated for the Te/Ge(111) system. Even considering moderate reconstructions, the constraints of maintaining reasonable bond lengths, along with the constraints already placed by the normal emission data, would lead to scattering from this atom which would be within 10° of backscattering, thus giving a much stronger oscillation amplitude than that which is apparent in the off-normal curve presented in Fig. 2. A similar situation would occur for adsorption in the 3-fold hollow site involving backscattering from a 2nd layer Ge atom, so that the off-normal results support neither 3-fold site.

Adsorption in a 2-fold bridge would explain the 4 A structure in terms of scattering primarily from a 2nd layer Ge near-neighbor atom with a scattering angle of 150°, including the reduced oscillation amplitude. Due to the different possible orientations of the Ge-S-Ge bridge relative to the emission direction, it is difficult to discuss qualitatively the off-normal ARPEFS for the 2-fold site. However, these different orientations would be expected to lead to smearing of the ARPEFS, in agreement with the lack of structure observed experimentally.

This very qulaitative discussion, by itself, clearly does not prove adsorption in a 2-fold bridge. However, it does provide evidence against the 3-fold or atop geometries. To proceed further in determining the adsorption geometry, we will examine the results of comparisons to multiple-scattering calculations.

5.3.2 Multiple scattering calculations

The calculations performed for comparisons to the ARPEFS for (2x2) S/Ge(111) were based on a treatment which provided excellent agreement with ARPEFS from other systems, and are described in detail elsewhere.[15] A brief outline of the major features of the calculations that are pertinant to S/Ge(111) will be presented here.

Previous work has shown that a quantitative theory of ARPEFS requires the inclusion of important multiple-scattering and spherical wave effects. The cluster calculations performed for this system included multiple-scattering to fourth order and also included the dominant corrections to the plane wave approximation due to the spherical nature of the photoelectron wave using the results presented in Ref. (25) The finite mean free path was treated as an exponential damping factor, $e^{-r/\lambda}$, with $\lambda=ck$. The value of c was determined as c = 0.75 by fitting to the mean free path results for Ge determined by Stern et al.[24] on the basis of their EXAFS measurements. Thermal effects were treated using a correlated Debye model which accounts for increased thermal vibrations near the surface.[15] The inputs to this model were adjusted based on EXAFS determinations of the mean-squared relative displacements for bulk Ge[24] and GeS.[26] Values for the enhancement of the surface vibrations over those in the bulk by up to a factor of 2 were employed, but had little effect on the relative levels of agreement attained for different adsorption geometries. The finite angular resolution of the experiment was also included.[15] The effect of the inner potential was treated as an energy independent shift of the kinetic energy scale.

The phase shifts used in these calculations were computed using a modified version of the program developed by Pendry for LEED.[27] The Ge potential was obtained from a muffin-tin calculation employing overlapping Hartree-Fock atomic wave functions. The S phase shifts were also calculated using a potential obtained from atomic Hartree-Fock wave functions. In this case, the wave functions were truncated and renormalized at a muffin-tin value R_{max} = 1.05 Å. Several values of R_{max} were tested and produced no strong differences in the results of the analysis. The exchange potential was calculated using an $X\alpha$ approach with α taken from the work of Schwarz.[28] A total of 16 phase shifts were calculated for each potential for energies up to 500 eV.

As discussed in Section 5.2.3, the data were filtered to remove frequencies below 2.0 Å. In addition, for the initial calculations performed to test the agreement of the various sites, the normal emission ARPEFS was filtered to remove frequencies above 5 Å. Calculations were then performed with these same cut-offs. This upper cut-off retains the dominant structure in the data, as is apparent from the Fourier transform in Fig. 3, and also includes a path length range large enough to include scattering from a set of atoms in each site which is sufficient to clearly distinguish one site from another. Further calculations for the normal emission geometry were also performed with an upper cut-off of 10 Å. The off-normal calculations were all performed with an upper cut-off of 10 Å.

The overlayer structure for the 2-fold site was assumed to consist of 3 domains of a (2x1) structure, in accordance with the 1/2 ML coverage and the (2x2) LEED pattern, while both p(2x2) and 3 domains of (2x1) were tested for the other sites. This assumption is not critical, and only affects the ARPEFS calculated for the off-normal emission to any significant degree. Even in this case, the effects are mainly at low path length values which have been excluded from consideration as described above. For each possible adsorption site, a series of calculations was performed with different distances of the sulfur atom above the Ge surface (from 0.5 -1.5 Å), and also with varying values of the first Ge interplanar separation (from 0.5 -1.1 Å). Calculations performed for the 2-fold bridge consisted of equal contributions from the possible orientations of the S bridge with respect to the emission and polarization directions.

The same r-factor employed in Chapter 4 was also used in this analysis. It consisted of forming,

$$r = \int [I_e(E)-I_t(E)]^2 dE \,/\, \int I(E)^2 dE. \qquad (5)$$

Here $I_e(E)$ is the intensity of the experimental curve as a function of the energy and $I_t(E)$ is the intensity of the theory. For each geometry comparisons were made to calculated curves with V_0 values of 8, 10, and 12 eV, in an attempt to partially account for the unknown value of the inner potential. These r values were then averaged to produce a final r value. Due to the ±2-3° accuracy with which experimental angles are determined, the angles used in the calculations were allowed to vary in order to obtain the best simulation of the experimental curves. These optimum angles were within 2° of the expected values in all cases. The final structural parameters determined by the r-factor analysis were quite insensitive to the exact angle used.

Fig. 5 presents the results of calculations for the 2-fold bridge, the 3-fold hollow, and the 3-fold eclipsed sites for the normal emission geometry employing an upper path length cut-off of 5 Å. For each site, the calculation presented represents the best agreement to the data obtained for variation of the S to first layer Ge distance (S-Ge_1) and the separation of the first and second Ge layers (Ge_1-Ge_2). The results for the atop geometry are not displayed because of the lack of any reasonable agreement. Displayed in Fig. 6 are the results of calculations performed for the off-normal geometry using the same geometries employed for Fig. 5. The much larger oscillation amplitude exhibited for the 3-fold sites is a consequence of the near-backscattering geometries for these two cases, as discussed earlier.

Figs. 5 and 6 clearly favor adsorption in the 2-fold bridge site. Contour plots of the r-factor for this site are presented in Figs. 7 and 8. Fig. 7 presents the variation of the r-factor with Ge_1-Ge_2 along the vertical axis and S-Ge_1 along the horizontal axis. A clear line of minima is indicated for values of these two parameters such that the S-Ge_2 distance is 1.8 Å. This line of minima indicates that the normal emission geometry is more sensitive to the position of the second layer Ge near-neighbor atom than to the first layer atoms. This is due to the closer proximity of the second layer atom to 180° scattering and the orientation of the photon polarization. Moving along this line, the region of absolute minimum indicates values of S-Ge_1 of 1.05 ±0.02 Å and Ge_1-Ge_2 of 0.75 ±0.02 Å. A similar contour plot is displayed in Fig. 8 for the off-normal geometry, indicating a value of S-Ge_1 of 1.00 ±0.02 Å and Ge_1-Ge_2 of 0.70 ±0.02 Å. The errors given represent only the precision of the measurement determined by the values of χ^2 from the fit to theory and the curvature of the minima. These results taken together indicate adsorption in a 2-fold bridge site 1.03 ±0.05 Å above the Ge surface and with a contraction of the separation between the first and second Ge layers by 0.07 ±0.05 Å (9 ±6 %). The errors quoted here are based on the standard deviation of the measurements, with estimates of the effects of experimental angle errors (~ 0.02 Å) and phase shifts (~ 0.02 Å).

Because the SEXAFS study of Te/Ge(111) indicated adsorption in the 3-fold eclipsed site, the data were tested for shifts of the S atom toward the 3-fold eclipsed and the 3-fold hollow sites. These shifts were found to be limited to < 0.1 Å, although this conclusion is based primarily on comparisons to the off-normal data, for which the weak experimental structure makes comparisons to theory difficult. The normal emission geometry is not sensitive to shifts of this magnitude in the horizontal direction. Also due to the somewhat long Ge-Ge distance and the 125° Ge-S-Ge angle compared to values of ~ 100° typically found in bulk compounds, reconstructions involving shifts of the two Ge first layer atoms to which the S atom is bonded towards each other were considered, but this also led to slightly worse agreement.

Calculations were also performed for the normal emission geometry with an upper cut-off of 10 Å in an attempt to determine the spacing between the second and third Ge layers. Near-backscattering from a Ge atom in the third layer, which is then enhanced by forward scattering through a second layer Ge atom, should make this geometry sensitive to the Ge_2-Ge_3 spacing. The results of these calculations are given in Fig. 9. This figure indicates a best value of 2.60-2.65 Å for the bilayer spacing, compared to a bulk value of 2.45 Å. This represents an expansion of 8 ±3 % in the Ge-Ge bond length between these layers. This result applies only to the Ge-Ge bond between the second and third layers directly below the 2-fold adsorption site-- no information could be obtained for the other bond spacings. Fig. 10 and Table I present a summary of the structural parameters.

Models involving sulfur dimers were also considered. The investigation of these possibilities was motivated by suggestions of peroxy adsorption geometries for oxygen on Si. Limited calculations were performed for dimer bridges between two surface Ge atoms and also for dimer structures, such as that illustrated in Fig. 11, for which the dimer is rotated out of the plane containing the two Ge atoms, to allow for bond angles of 90-100° at the S atoms. None of these models produced as good agreement as that found for the 2-fold bridge geometry.

5.4 Conclusions

We have performed ARPEFS measurements for the (2x2) S/Ge(111) surface which is formed upon annealing a surface covered with 1/2 ML of sulfur. The sulfur was determined to occupy the 2-fold bridge position 1.03 ±0.05 Å above the Ge surface. These studies also indicate a contraction between the first and second Ge layers of 9 % and an expansion between the second and third Ge layers of 8 ±3 %. The weakening of the Ge-Ge bond may provide an explanation for the mechanism by which the etching of Ge in sulfur vapor occurs.[29] This, however, does not explain the similar etch rates observed for the different faces of Ge.[29]

The different structures obtained in this study and the SEXAFS study of Te/Ge(111) are hard to explain considering the other apparent similarities between the two systems. The locally unreconstructed adsorption site proposed for Te/Ge is somewhat unusual considering the closeness of a second layer Ge atom to the adsorbed Te. In addition, the other two cases of divalent atomic adsorption on (111) surfaces of homopolar semiconductors-- Se/Si(111) and Te/Si(111)-- both indicated 2-fold bridge sites.

Further studies of adsorption on semiconductor substrates using the ARPEFS technique are planned. Preliminary LEED and AES studies of the adsorption of phosphorus on Ge(111) have been performed, and ARPEFS studies are planned. This system will extend the investigation to trivalent adsorbates and should provide an interesting comparison to the recent angle-resolved photoemission studies and total energy calculations performed for As/Ge(111) and As/Si(111).[30] It has been proposed that As passivates these surfaces by occupying first layer substitutional sites.

While these studies can be viewed as attempts to understand the basic aspects of the chemisorption and bonding which occurs on these surfaces, they may have important technological implications as well. These systems may provide information that is important in understanding the changes in the CVD growth rates of Si when in situ doping by the addition of PH_3 and B_2H_6[31] is attempted. Different adsorption sites or differing amounts of surface strain introduced in accomodating the adsorbate may lead to the reduction or enhancement of the normal Si growth rates. For instance, the passivation of the Si(111) surface found for As overlayers [30] may provide an explanation of the greatly reduced growth rate when PH_3 is introduced. There have also been suggestions that "surface doping" with adsorbed gases might be employed to control Schottky barrier heights[32]-- knowledge of the adsoption structure will help in understanding the character of the "dopant".

REFERENCES

1. Determination of Surface Structure by LEED, ed. P.M. Marcus and F. Jona, (Plenum Press, New York, 1984).
2. J.F. Van der Veen, Surf. Sci. Reports 5, (1985).
3. a) J.E. Rowe and P.H. Citrin, in "Proceedings of the 17th Intl. Conf. on the Physics of Semiconductors", ed. J.D. Chadi and W.H. Harrison, (Springer-Verlag, New York, 1985) p. 89; b) P.H. Citrin, P. Eisenberger, and J.E. Rowe, Phys. Rev. Lett. 48, 802 (1981); c) P.H. Citrin, J.E. Rowe, and P. Eisenberger, Phys. Rev. B 28, 2299 (1983).
4. J.J. Barton, C.C. Bahr, Z. Hussain, S.W. Robey, J.G. Tobin, L.E. Klebanoff, and D.A. Shirley, Phys. Rev. Lett. 51, 272 (1983).
5. M. Green and K.H. Maxwell, J. Phys. Chem. Solids 13, 145 (1960).
6. U. Hofer, P. Morgan. W. Wurth, and E. Umbach, Phys. Rev. Lett. 55, 2979 (1985).
7. J.A. Golovchenko, J.R. Patel, D.R. Kaplan, P.L. Cowan, and M.J. Bedzyk, Phys. Rev. Lett. 49, 560 (1982).
8. G. Materlik, A. Frahm, and M.J. Bedzyk, Phys. Rev. Lett. 52, 441 (1984).
9. B.N. Dev, V. Aristov, N. Hertel, T. Thundat, and W.M. Gibson, J. Vac. Sci. Technol. A3(3), 975 (1985).
10. M.J. Bedzyk and G. Materlik, to appear in Phys. Rev. B.
11. B.N. Dev, T. Thundat, and W.M. Gibson, J. Vac. Sci. Technol. A3(3), 946 (1985).

12. J.J. Barton, S.W. Robey, C.C. Bahr, and D.A. Shirley, 1st Intl. Conf. on the Structure of Surfaces, Berkeley, CA., Springer Series in Surface Sciences 2, ed. M.A. Van Hove and S.Y. Tong, (1985).

13. S.W. Robey, J.J. Barton, C.C. Bahr, G. Liu, and D.A. Shirley, (to be published); C.C. Bahr, J.J. Barton, Z. Hussain, S.W. Robey, J.G. Tobin, and D.A. Shirley, (to be published).

14. P.J. Orders and C.S. Fadley, Phys. Rev. B 27, 781 (1983); E.L. Bullock, C.S. Fadley, and P.J. Orders, Phys. Rev. B 28, 4867 (1983); M. Sagurton, E.L. Bullock, and C.S. Fadley, Phys. Rev. B 30, 7332 (1984).

15. J.J. Barton, S.W. Robey, and D.A. Shirley, (to be published).

16. S.Y. Tong, and C.H. Li, in Chemistry and Physics of Solid Surfaces, vol. III, ed. R. Vanselow and W. England, CRC Press, (1982), p.287; C.H. Tong and S.Y. Tong, Phys. Rev. Lett. 43, 526, (1979).

17. A.H. Boonstra and J. Van Ruler, Surf. Sci. 4, 141 (1966).

18. L. Surnev and M. Tikhov, Surf. Sci. 138, 40 (1984).

19. A.J. Van Bommel and F. Meyer, Surf. Sci. 6, 391 (1967).

20. a) J.J. Barton, C.C. Bahr, S.W. Robey, Z. Hussain, and D.A. Shirley, (to be published); b) J.J. Barton, Ph.D. thesis, Univ. of Calif., Berkeley (1985); c) S.W. Robey, Ph.D. thesis, Univ. of Calif., Berkeley (unpublished).

21. P.A. Lee, P.H. Citrin, P. Eisenberger, and B.M. Kincaid, Rev. Mod. Phys. 53, 769 (1981).

22. V.G. Bissert and K.-F. Hesse, Acta. Cryst. B34, 1322 (1978).

23. V.G. Dittmar and H. Schafer, Acta. Cryst. B31, 2060 (1975).

24. E.A. Stern, B. Bunker, and S.M. Heald, in "EXAFS Spectroscopy: Techniques and Applications", Plenum Press, 1981, ed. B.K. Teo and D.C. Joy, p. 59.

25. J.J. Barton and D.A. Shirley, Phys. Rev. A 32, 1019 (1985); J.J. Barton and D.A. Shirley, Phys. Rev. B 32, 1892,1906 (1985).

26. P. Rabe, G. Tolkein, and A. Werner, J. Phys. C 13, 1857, (1980).

27. J.B. Pendry, Low Energy Electron Diffraction, (Academic Press, London, 1974).

28. K. Schwarz, Phys. Rev. B 5, 2466 (1972).

29. S.M. Repinsky and O.I. Semyonova, Thin Solid Films, 75, 391 (1981).

30. R.I.G. Uhrberg, R.D. Bringins, M.A. Olmstead, R.Z. Bachrach, and J.E. Northrup, Bull. Amer. Phys. Soc. 31, 373 (1986); R.D. Bringans, M.A. Olmstead, R.I.G. Uhrberg, and R.Z. Bachrach, Bull. Amer. Phys. Soc. 31, 373 (1986).

31. F.C. Eversteyn and B.H. Put, J. Electrochem. Soc. 120, 106 (1973); B.S. Meyerson and M.L. Yu, J. Electrochem. Soc. 131, 2366 (1984).

32. V. Montgomery, R.H. Williams, and G.P. Srivastava, J. Phys. C 14, L191 (1981).

Table I. Summary of the structural parameters determined from the ARPEFS measurement. The definitions of the parameters S-Ge$_1$, Ge$_1$-Ge$_2$, and Ge$_2$-Ge$_3$ are the distance of the sulfur above the first Ge layer, the separation between the first and second Ge layers, and the separation between the second and third Ge layers respectively. The final parameter is the Ge-S-Ge bond angle.

Parameter	Value
S-Ge$_1$	1.03(5) Å
Ge$_1$-Ge$_2$	0.73(5) Å
Ge$_2$-Ge$_3$	2.65(7) Å
Ge-S-Ge angle	125°

FIGURES

Fig. 1 Normal emission $\chi(k)$ data. The upper curve gives the raw data and the lower solid curve represents the same data after Fourier filtering to remove "frequencies" above 10 Å. The error bar at the top displays the level of statistical uncertainty in the data. These data represent the average of two normal emission measurements.

Fig. 2 Same as Fig. 1 for the off-normal data, except that only one measurement was performed for this geometry.

Fig. 3 Fourier transforms of the data from Figs. 1 and 2, using a gaussian broadened (1 Å) window function to reduce truncation effects.

Fig. 4 Two views of the Ge(111) surface illustrating the adsorption sites discussed in the text. The upper panel presents a view looking down on the surface and the lower panel gives a perspective with the surface normal rotated away from the reader. Two 2-fold bridge sites are included to illustrate the different possible orientations of the sulfur bridge.

Fig. 5 This figure illustrates the best fits to the normal emission data (filtered at 5 Å) determined from r-factor comparisons for the 2-fold bridge, the 3-fold hollow, and the 3-fold eclipsed sites.

Fig. 6 Off-normal theory compared to the data (filtered at 10 Å) for the same geometries used in Fig. 5.

Fig. 7 Contour plot of the r-factor for the normal emission data. The horizontal axis gives the distance of the S atom above the first Ge plane, and the vertical axis gives the separation between the first and second Ge layers (bulk value = 0.8 Å). The contours are in increments of 0.3.

Fig. 8 Same as Fig. 7 for the off-normal data. Each contour is incremented by 0.5.

Fig. 9 Comparison of the normal emission data (filtered at 10 Å) to theory for several values of the separation between the second and third Ge layers (first and second Ge bilayers).

Fig. 10 Segment of the (111) surface indicating the adsorption site and local structure determined from ARPEFS. The surface is cut along a $(1\bar{1}0)$ plane-- the Ge atoms connected by thick bonds are in a plane closer to the reader than those connected by thin bonds. The sulfur is also in the second, thin-bond plane. Our results do not give information about the planarity of the Ge layers, and hence the spacing values of 1.05 Å (S-Ge_1), 0.75 Å (Ge_1-Ge_2), and 2.65 Å (Ge_2-Ge_3) apply only to the Ge atoms below the 2-fold adsorption site.

Fig. 11 This figure presents one of the models for S dimer adsorption that were considered. The dimers are rotated to allow for bond angles at the S atom of ~ 90°-100°. Other models without rotated dimers were also tested.

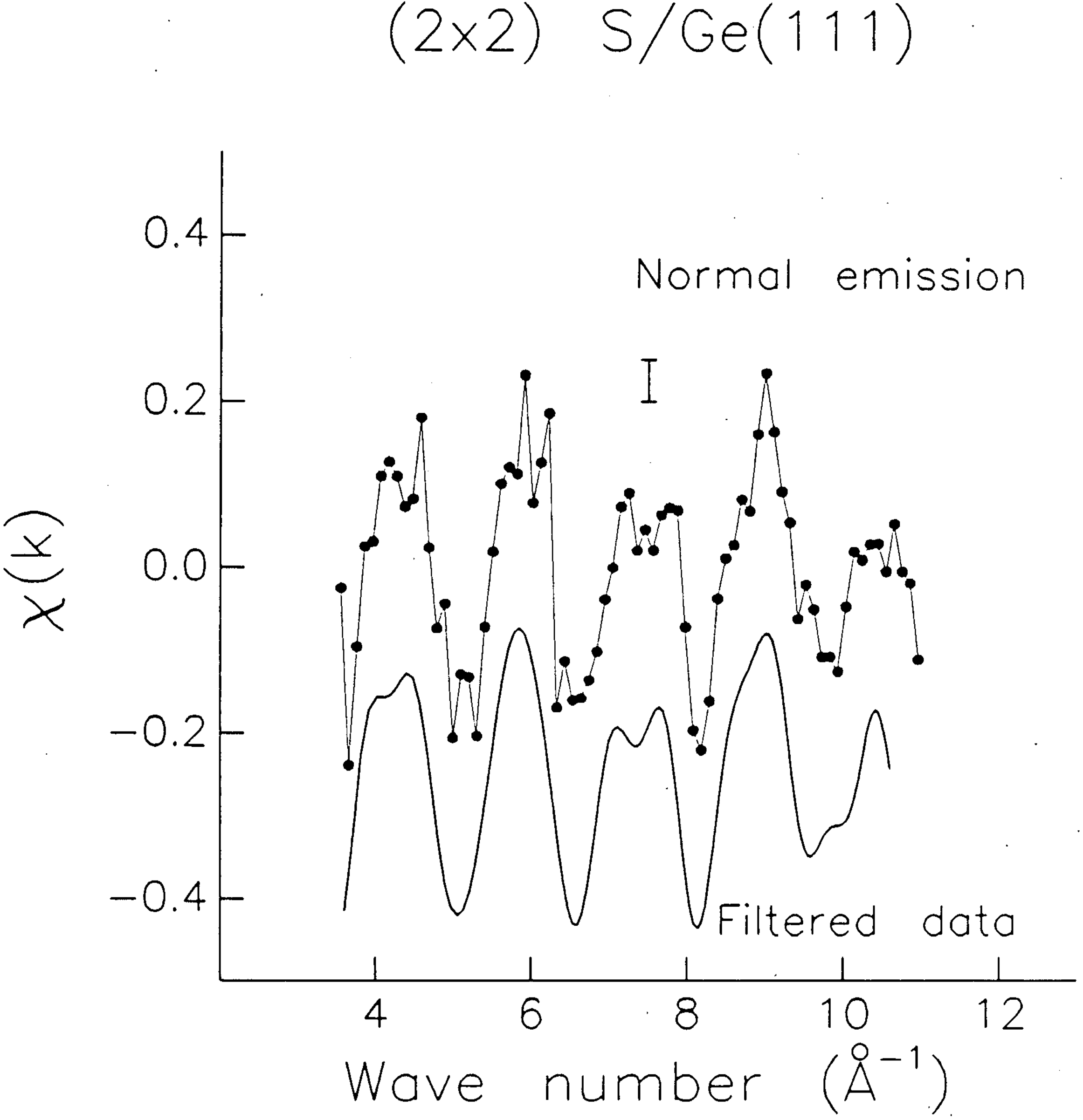

XBL 864-1552

Fig. 1

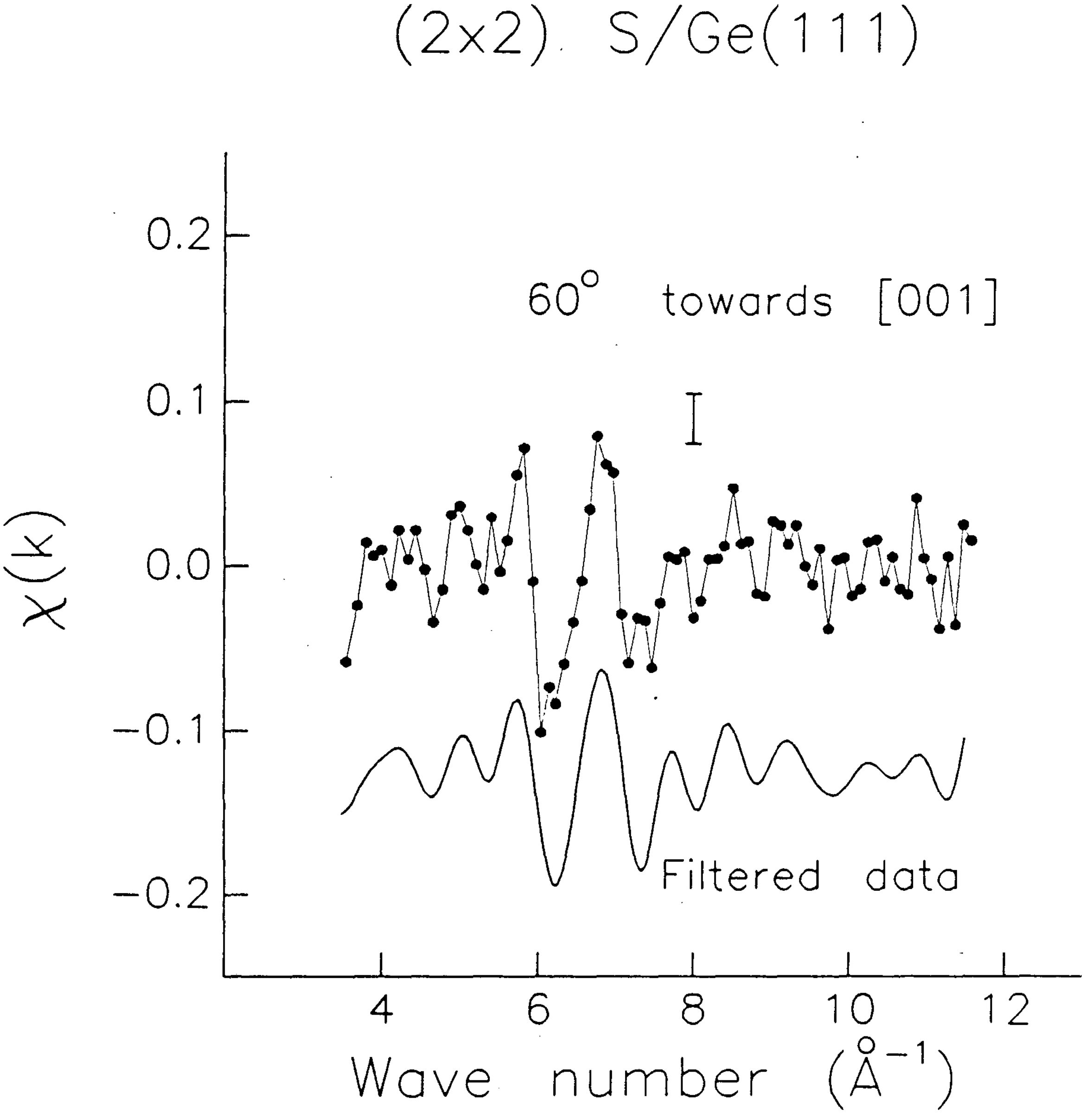

XBL 864-1550

Fig. 2

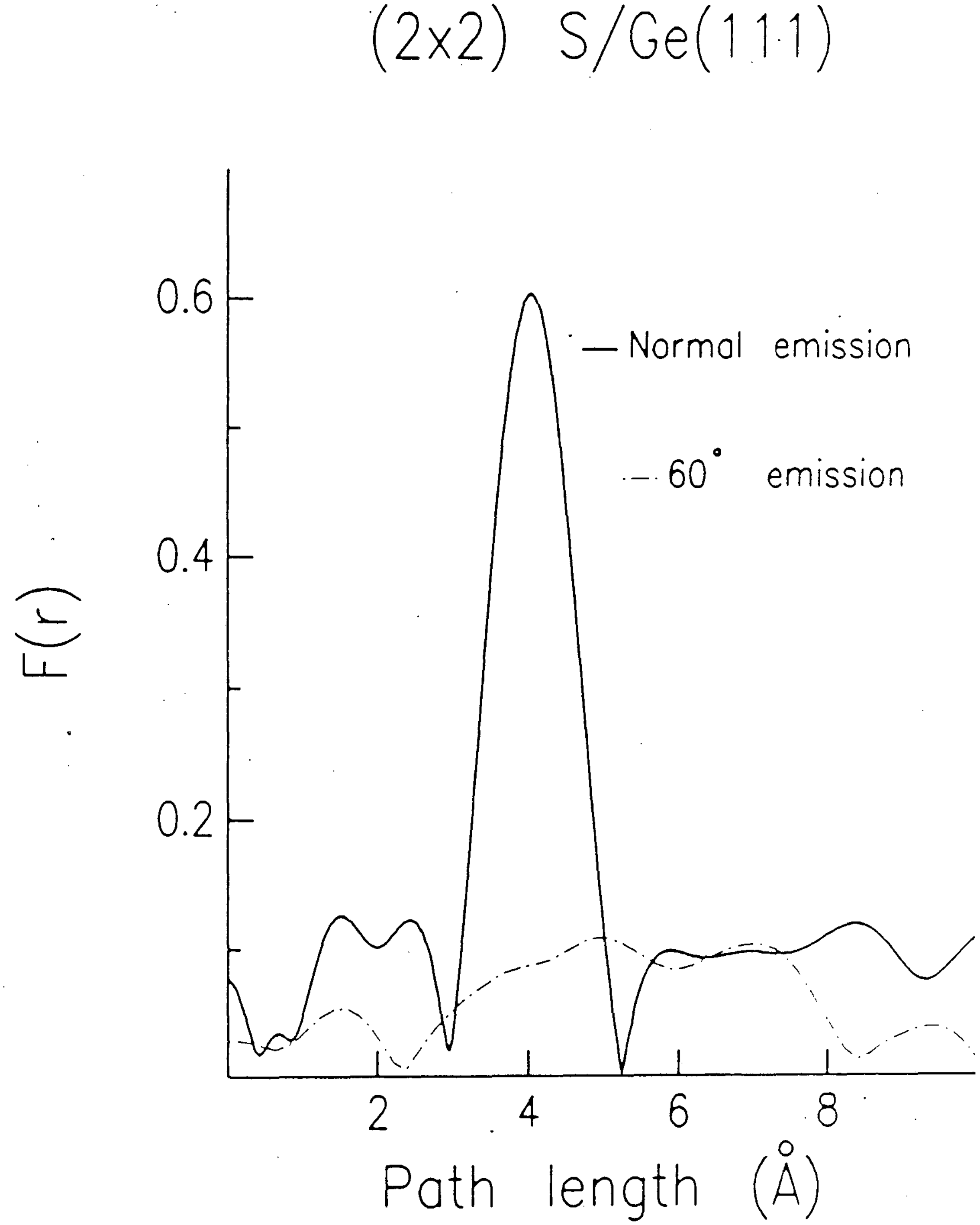

XBL 864-1279

Fig. 3

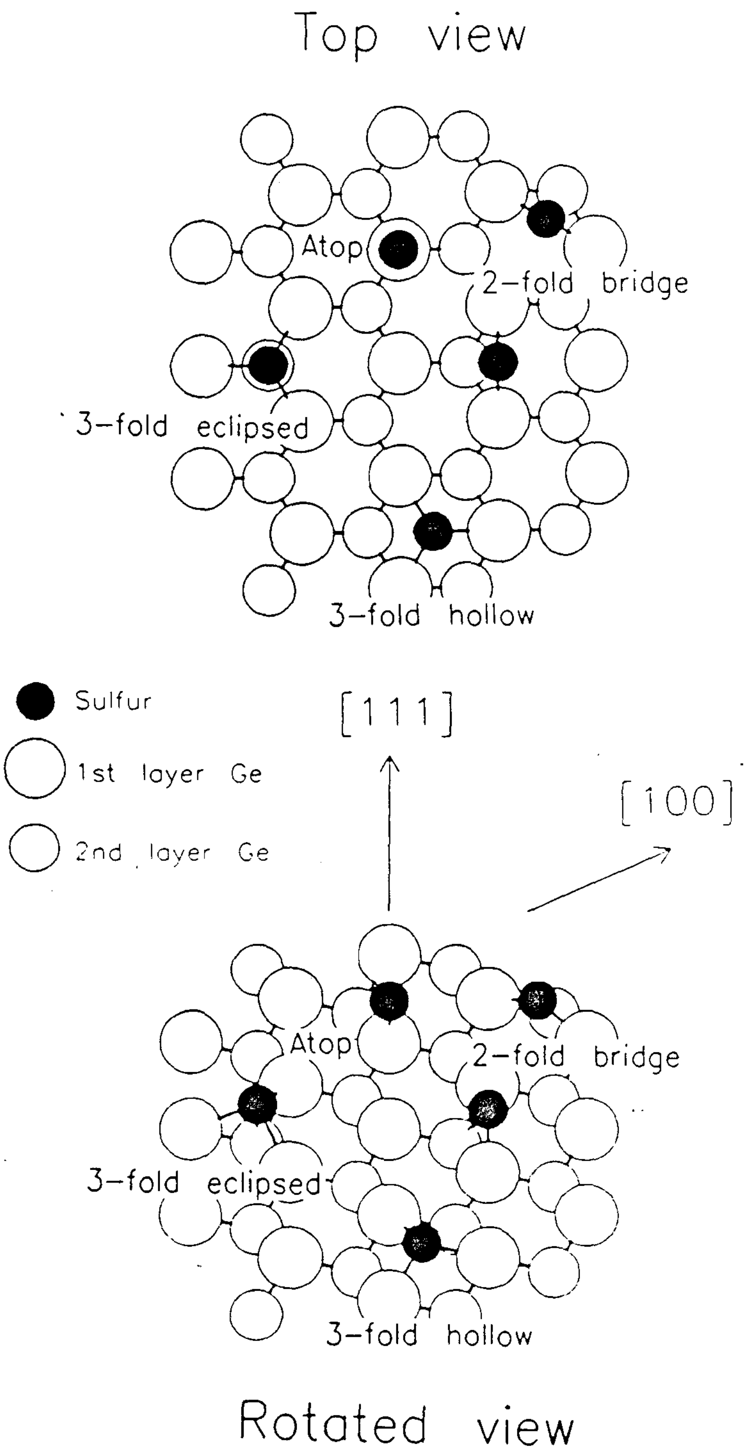

XBL 864-1283

Fig. 4

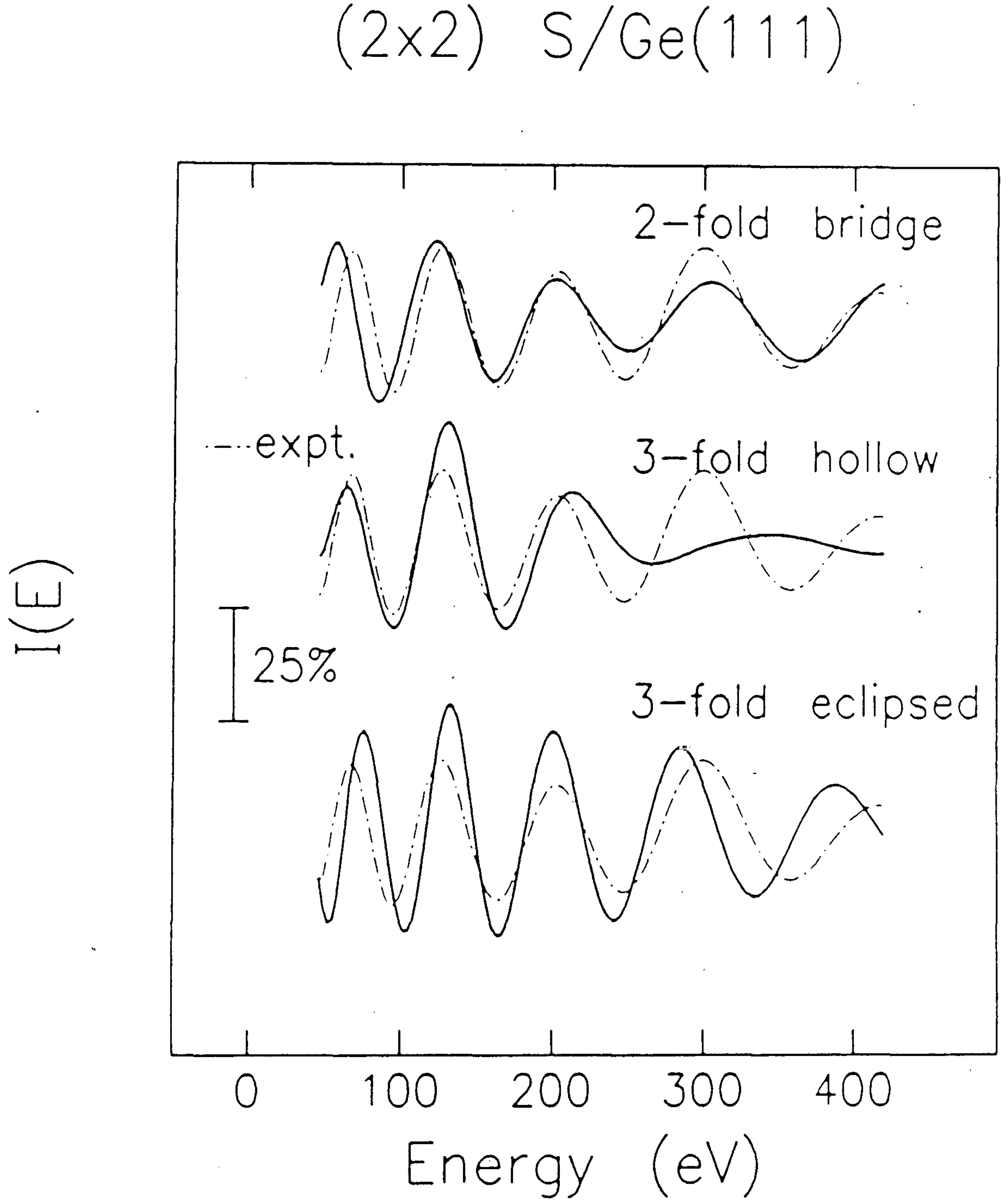

XBL 864-1280

Fig. 5

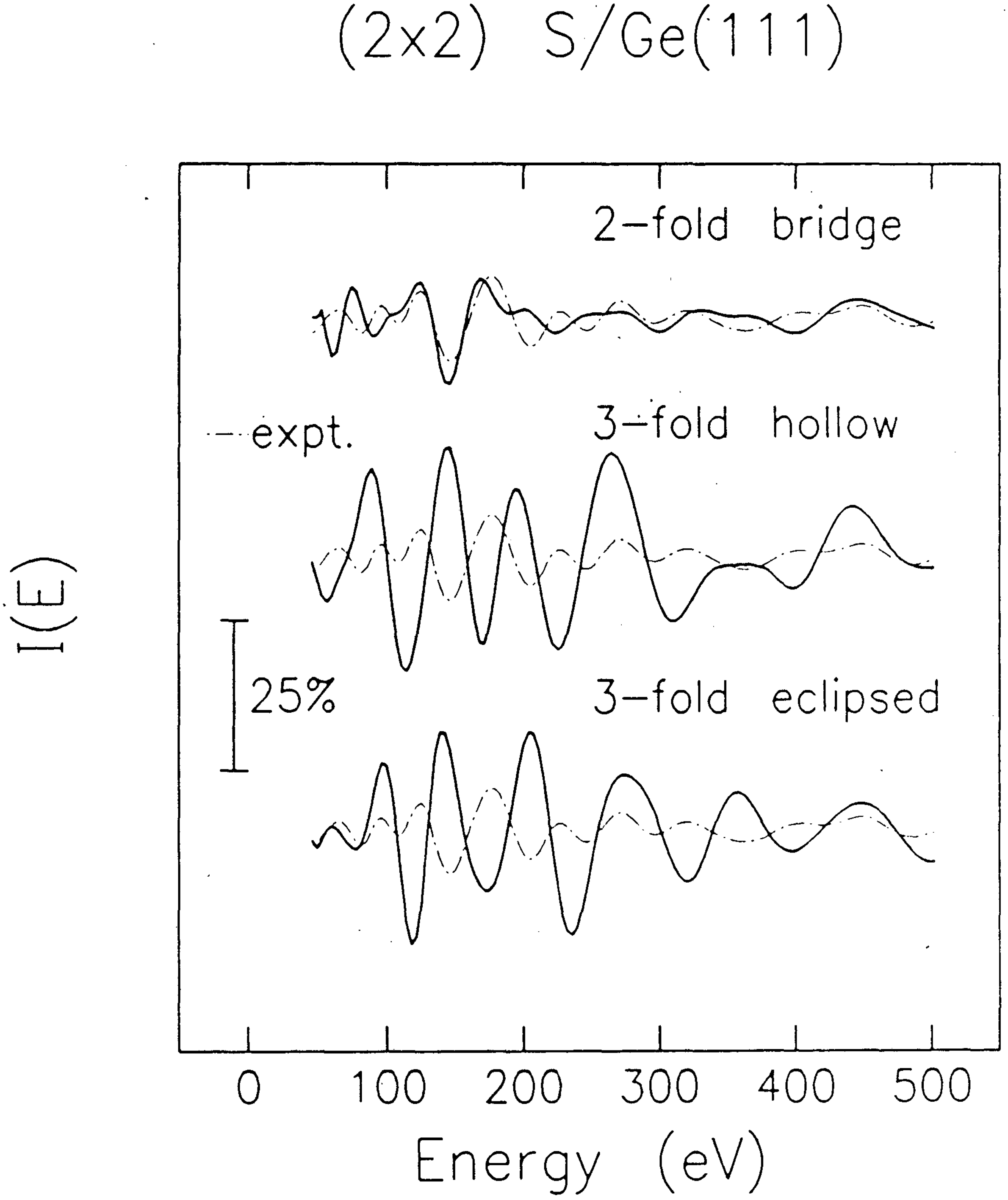

XBL 864-1281

Fig. 6

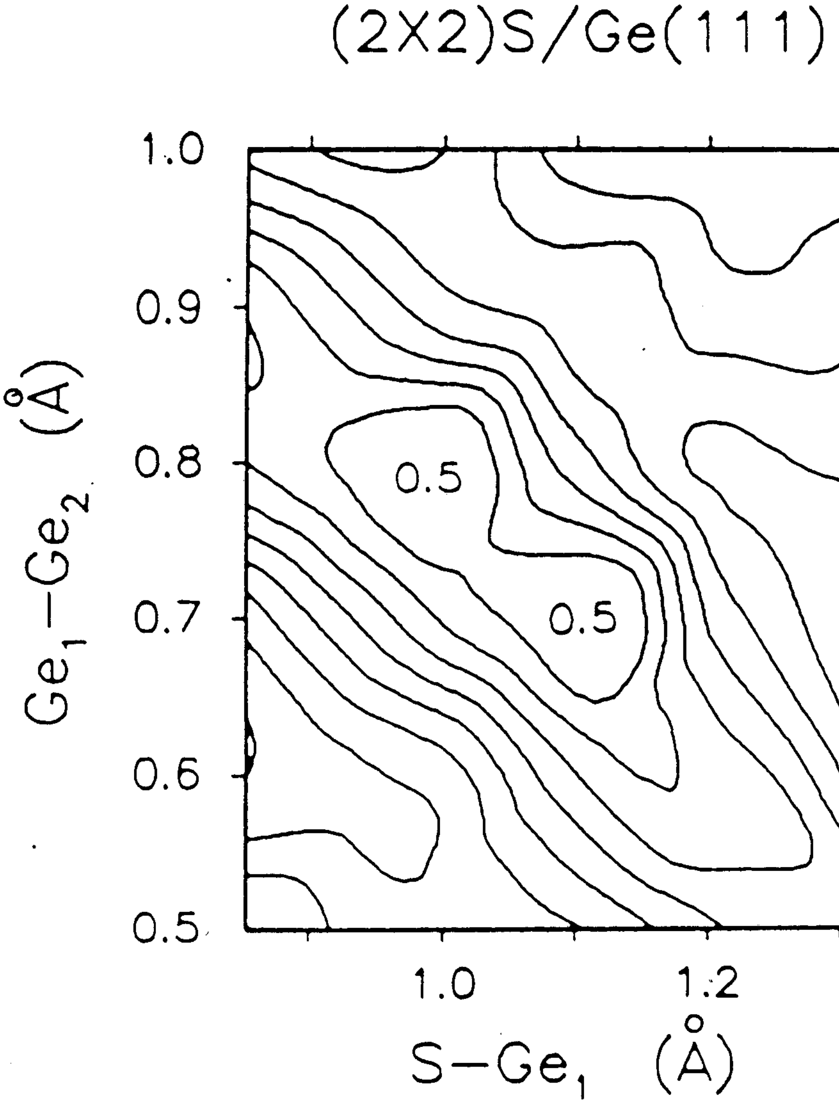

XBL 864-1274

Fig. 7

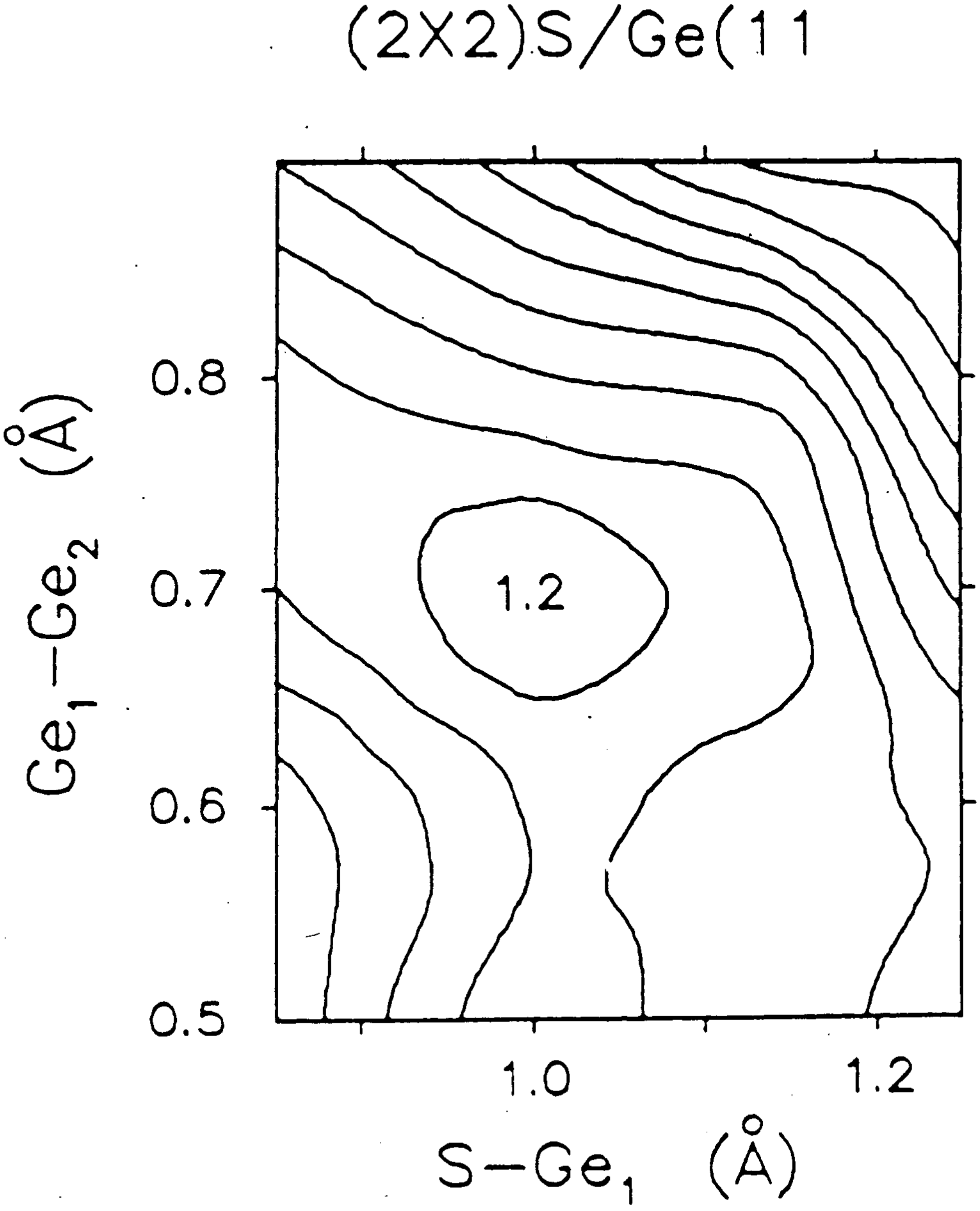

XBL 864-1282

Fig. 8

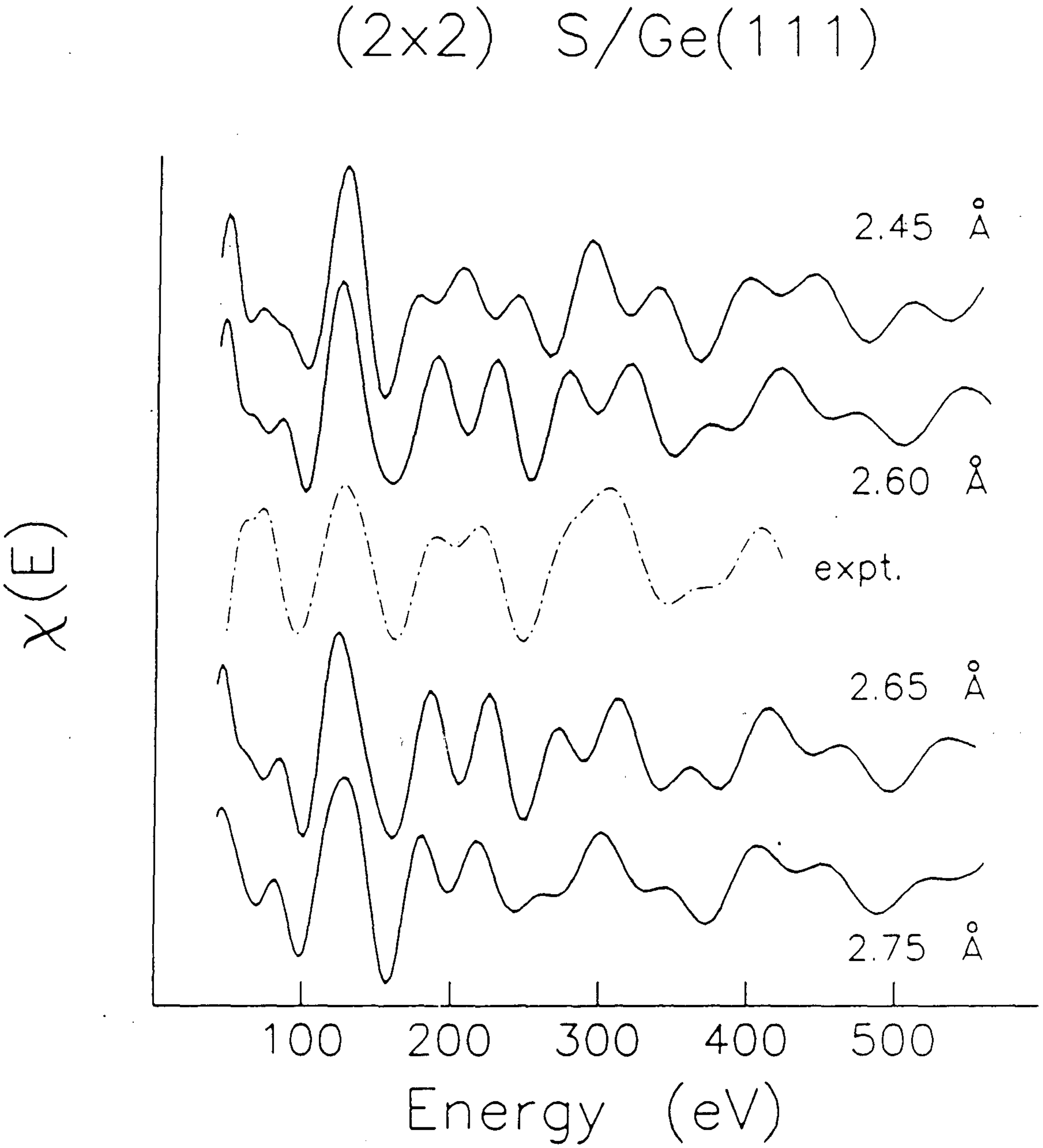

XBL 864-1275

Fig. 9

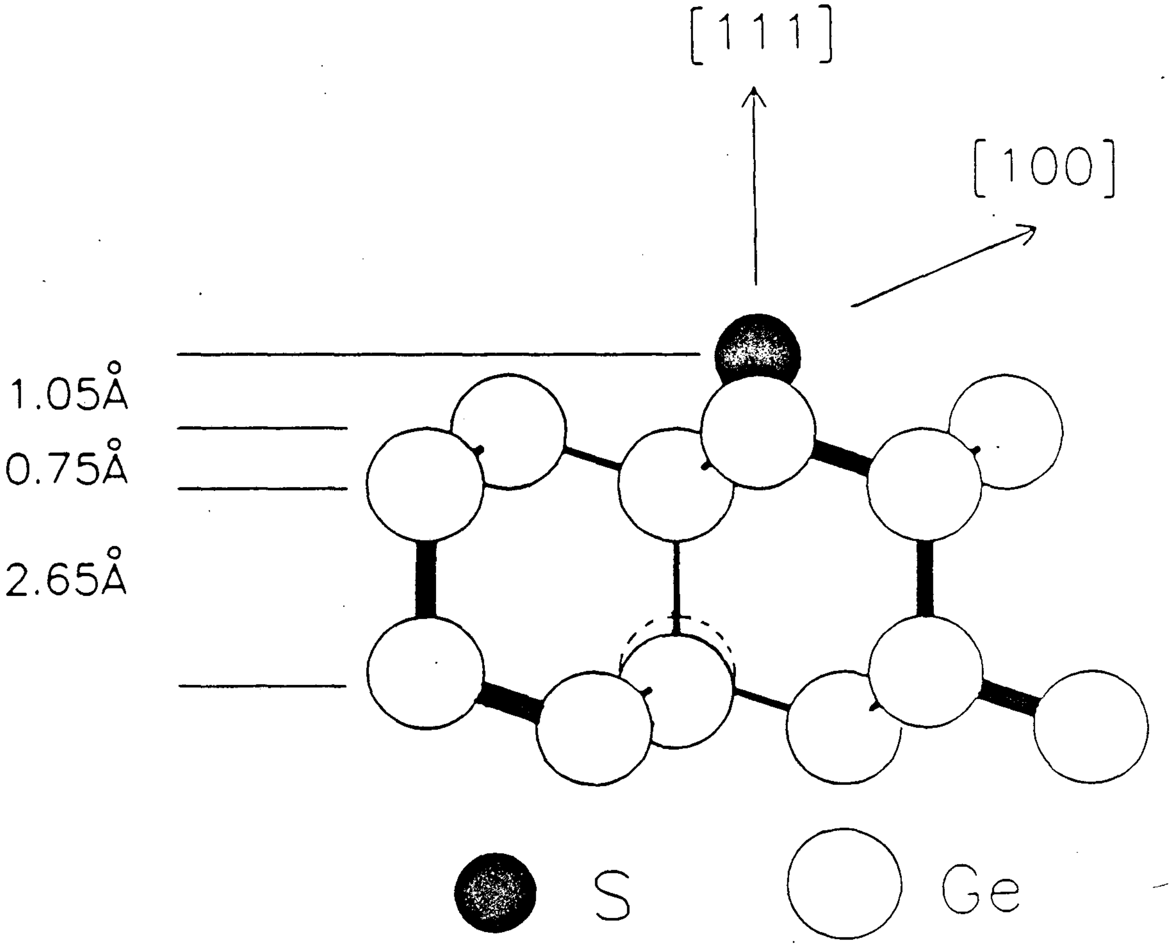

XBL 864-1549

Fig. 10

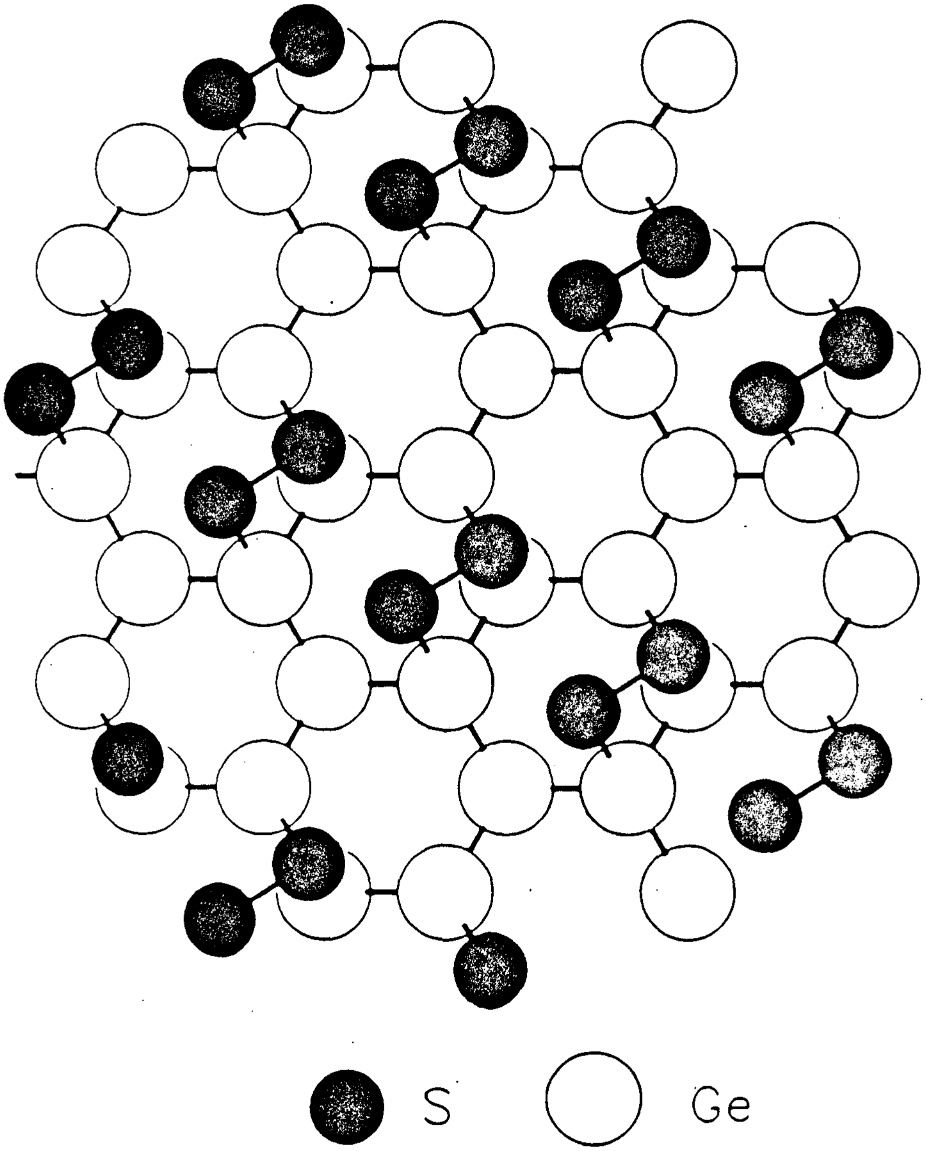

XBL 864-1285

Fig. 11

CHAPTER 6

Conclusions

The results presented in this thesis, as well as those from other studies, clearly indicate that ARPEFS has the capability of providing detailed local surface structural information. The ability to determine the relaxation of the Ni(011) surface due to the adsorption of sulfur, even employing simple Fourier transform methods, attests to this fact. Also, the computational simplicity of ARPEFS theory compared to, for instance LEED, allows for a more detailed investigation of the possible structures for the same cost in computation time.

While for best case situations, such as the S/Ni(011) experiment, much information can be gained by direct inversion of the data using Fourier transform techniques, this will in general not be possible. For more complicated systems, the structure in the Fourier transform will not be unambiguous enough to be used for this purpose without first employing comparisons to theoretical calculations. Once an analysis based on comparison to theory has been performed, of course, the use of backtransform techniques becomes moot. The effort expended on obtaining data of sufficient quality for a backtransform analysis (primarily of sufficient energy range) must be weighed against other factors such as the limited amount of time available. In some cases it may be preferable to limit the data range to ~ 200-250 eV so that adequate time for reproduction of the data is ensured and additional experimental geometries may be employed. This is particularlly true since the accumulation of the last ~ 100 eV of the typically employed energy range takes about 1/2 of the total time. Instead, the importance of the Fourier transform results presented here and in other studies is in the fact that they indicate that ARPEFS can be described within a relatively simple, local structure framework. Thus, while the use of backtransform techniques to directly obtain pathlengths will be limited, the qualitative information in terms of pathlength distributions will be useful by providing an alternative, more physically appealing view of the data.

Even without the ability to perform direct inversion of the data, ARPEFS still enjoys some advantages. The calculations are far simpler than LEED calculations for comparable systems and the measurement can be restricted to obtaining information about the local structure around a particular constituent of the surface system by choice of the appropriate core level. The anisotropy in the possible experimental information is much larger than can be obtained from SEXAFS.

Of course, there are also disadvantages. The level of sophistication in the equipment necessary to perform an ARPEFS experiment is greater than that typically necessary for a SEXAFS measurement. However, the need to have an angle-resolving electron analyzer can not really be viewed as a restriction when ARPEFS is viewed in the broader sense as being a sub-class of the general technique of angle-resolved photoemission. The versatility of ARP is unrivaled in surface studies. The necessity of employing synchrotron radiation does not compare well with the experimental accessability of LEED, but this situation is slowly changing. The qualitative simplicity of ion scattering makes that technique very attractive, but it too requires a sophisticated experimental arrangement and/or suffers from experimental problems such as unknown ion neutralization factors. It is clear, however, that each of these techniques has merits, and only by combining them and also using the additional information which can be obtained from techniques such as XPS and HREELS can complicated surface structures be determined unambiguously.

In addition to serving as a means of evaluating ARPEFS, it is hoped that the experiments presented in this thesis have provided some interesting results on the systems studied and will stir future work. The asymmetry between the atopped and unatopped second layer Ni atoms suggested for the S/Ni(011) system warrants further experimental studies, and also provides an interesting problem for theoretical investigations. Chemisorption studies for semiconductor surfaces employing ARPEFS provide an extremely interesting, and challenging, variety of possibilities. Several directions for future work were suggested in Chapter 5. The more complex nature of these systems will make the high directional anisotropy of ARPEFS a very attractive feature, even more attractive than in the case of the more symmetric adsorption sites normally encountered for metallic substrates.

ACKNOWLEDGMENTS

The biggest contribution to this work came from the love and support of my parents. This thesis is as much their accomplishment as mine.

I also wish to thank all the members of the Shirley group whom I have come in contact with over the last few years. They all, in some way or another, made my years at Berkeley easier, or at least more interesting. I am especially thankful to John Barton, Charlie Bahr, and Zahid Hussain-- their collaboration made this work possible. I also thank Jim Tobin for his early help in learning experimental technique. It has been a pleasure to work with the fine people at LBL such as Joe Katz and Wini Heppler.

I also thank Profs. David A. Shirley and Alan M. Portis for their efforts as advisors.

Finally, I especially wish to thank Janice for her constant help and support, and for her efforts in broadening my interests.

This work was supported by the Director, Office of Energy Research, Office of Basic Energy Sciences, Chemical Sciences Division of the U.S. Department of Energy under Contract No. DE-AC03-76SF00098. It was performed at the Stanford Synchrotron Radiation Laboratory, which is supported by the Department of Energy's Office of Basic Energy Sciences.

LAWRENCE BERKELEY LABORATORY
TECHNICAL INFORMATION DEPARTMENT
UNIVERSITY OF CALIFORNIA
BERKELEY, CALIFORNIA 94720